Electrical Properties of Functionalized Nanowire Field Effect Transistors

THÈSE N^{O} 4092 (2008)

PRÉSENTÉE LE 28 AOÛT 2008
À LA FACULTE SCIENCES DE BASE
LABORATOIRE DE SCIENCE À L'ÉCHELLE NANOMÉTRIQUE
PROGRAMME DOCTORAL EN PHYSIQUE

ÉCOLE POLYTECHNIQUE FÉDÉRALE DE LAUSANNE

POUR L'OBTENTION DU GRADE DE DOCTEUR ÈS SCIENCES

PAR

Ralf Thomas WEITZ

physicien, Ruprecht-Karls-Universität, Heidelberg, Allemagne
et de nationalité allemande

acceptée sur proposition du jury:

Prof. R. Schaller, président du jury
Prof. K. Kern, directeur de thèse
Prof. J. Brugger, rapporteur
Dr P. Gröning, rapporteur
Dr H. Klauk, rapporteur

ÉCOLE POLYTECHNIQUE
FÉDÉRALE DE LAUSANNE

Suisse
2008

Abstract

The utilization of functional organic materials holds great promise for applications in electronic devices. Semiconducting organic molecules are frequently used as channel material in field effect transistors, due to the ease by which they can be assembled as such components, and the ease with which their properties can be specifically tailored. An extension of the use of organic materials in field effect transistors with the potential to substantially improve the performance of such devices is investigated in this thesis. It is the miniaturization of the functional parts of these devices, including their conductive channel or the gate dielectric, down to nanoscopic dimensions, which is important for their integration into complex device architectures. The materials under consideration offer advantages over conventional field effect transistor channels, including improved processibility, high mobility and electrical stability.

The first part of the thesis is dedicated to the fabrication and electrochemical functionalization of nanoscopic field effect transistors comprising individual semiconducting single-walled carbon nantoubes. The combination of an ultra-thin gate dielectric based on an organic self-assembled monolayer is used for the fabrication of high-performance field effect transistors that show large on-state transconductance, as well as a large on/off ratio of 10^7, negligible hysteresis in the drain current, and a subthreshold swing that approaches the room temperature limit of 60 mV/decade.

Two different types of self-assembled monolayers are used. The first, a silane-based self-assembled monolayer, is utilized to build field effect transistors in a global back gate geometry. This layout is useful for demonstrating the benefits of the use of a self-assembled monolayer for nanotube field effect transistors. Secondly, a gate dielectric incorporating a self-assembled monolayer composed of an alkane phosphonic-acid is exploited for the fabrication of high-performance field effect transistors with patterned aluminum gate electrodes. This geometry allows for the fabrication of more than one gate electrode per substrate and thus for the realization of logic circuits with all field effect transistors located on the same substrate. The technological relevance of nanotube field-effect transistors is proven by showing that nanotube field effect transistors can be cycled for more than 10^4 times between their on and off state and stored in ambient air for more than 200 days without degradation of their electrical performance.

The electrochemical functionalization of individual single-walled carbon nanotubes with the organic coordination magnet Prussian Blue is investigated in the second part of this thesis. While this modification leaves metallic tubes unaffected, semiconducting SWCNTs become strongly p-doped during the electrochemical process. The temperature-dependent electrical behavior of Prussian Blue-functionalized semiconducting tubes can be understood by the freeze-out of the transfer of holes from the Prussian Blue below 150 K.

In the third part of this thesis, novel core-cyanated perylene carboxylic diimides end-functionalized with substituents of varying flourine content and geometry are utilized as active material in air-stable n-channel thin film field-effect transistors. The relation between the thin-film structure and the air stability of the charge carrier mobility is investigated. Contrary to previous reports, it is found that the air stability is not related to the redox potential of the molecules. In addition, one of the compounds is used for the fabrication of field-effect transistors with a nanoribbon channel. These nanoribbons self-assemble from the solution phase, and, owing to their high crystalline order, field effect transistors with mobilities of up to 0.2 $\mathrm{cm}^2/\mathrm{Vs}$ in air could be realized. The air stability of their mobility is found to be superior to that of thin-film transistors based on the same compound. Since the investigated perylene derivatives offer the possibility of fabricating thin-film as well as nanobelt field-effect transistors, they represent a valuable model system for the investigation of the relation between the crystalline order, mobility, stability and the performance of organic n-channel field-effect transistors.

The last part is dedicated to a novel method for the fabrication of nanoscale polymer wires of diameters as small as 25 nm that offer potential as channel material for nanofiber field-effect transistors. These fibers emerge from a polymer solution during a standard spin-coating process. The fiber formation relies upon the Raleigh-Taylor instability of the spin-coated liquid film that arises due to a competition of the centrifugal force and the Laplace force induced by the surface curvature.

Keywords: Carbon Nanotube, Field Effect Transistor, Self-Assembled Monolayer, Electrochemistry, Prussian Blue, Thin Film Field Effect Transistor, Perylene Diimide, Air Stability, Spin Coating, Raleigh-Taylor Instability, Polymer Nanofiber.

Zusammenfassung

Funktionellen organischen Materialien wird ein großes Potential für zukünftige Anwendungen in elektronischen Bauteilen zugeschrieben. Bereits heute werden organische Moleküle als aktive Materialien in Feldeffekttransistoren verwendet. Der Grund hierfür liegt in der relativen Einfachheit mit der sie zu elektronischen Bauteilen zusammengefügt werden können, sowie der Möglichkeit, ihre Eigenschaften gezielt einzustellen. Die vorliegende Arbeit befasst sich mit einer vielversprechenden Erweiterung dieses Ansatzes, nämlich der Miniaturisierung der Feldeffekttransistoren hin zu nanoskopischen Dimensionen. Dies stellt einen wichtigen Schritt zur möglichen Integration solcher Bauteile in komplexe elektronische Strukturen dar. Die hierbei verwendeten Materialien sind den herkömmlich für organische Feldeffekttransistoren verwendeten hinsichtlich der Prozessierbarkeit, Ladungsträgerbeweglichkeit und elektrischen Stabilität überlegen.

Der erste Teil der Arbeit befasst sich mit der Herstellung und elektrochemischen Modifizierung von Feldeffekttransistoren, die auf einzelnen halbleitenden einwandigen Kohlenstoffnanoröhren basieren. Hochleistungsfähige Nanoröhrentransistoren Feldeffektransistoren werden in Kombination mit einem ultradünnen zur Isolierung der Steuerelektrode verwendeten Dielektrikums hergestellt. Dieses Dielektrikum basiert auf einer selbstorganisierenden Monolage und erlaubt es, die Feldeffekttransistoren bei niedrigen Versorgungsspannungen zu betreiben. Die Qualität der Feldeffekttransistoren spiegelt sich in ihrem hohen Durchgangsleitwert, der vernachlässigbaren Hysterese im Strom und einem Unterschwellanstieg, welcher nahe dem minimal bei Raumtemperatur erreichbaren liegt (60 mV/dec), wider. Für die Herstellung der Feldeffekttransistoren werden zwei unterschiedliche selbstorganisierende Monolagen verwendet. Die erste basiert auf einer Silan-Ankergruppe. Sie wird eingesetzt, um Feldeffekttransistoren mit globalen Steuerelektroden herzustellen. Diese Konfiguration wird verwendet, um die Vorteile, welche die Benutzung einer selbstorganisierenden Monolage als Teil des Dielektrikums hat, zu demonstrieren. Des Weiteren werden Hochleistungsfeldeffekttransistoren untersucht, deren in diesem Falle strukturierte Steuerelektrode, aus Aluminium besteht. Da Silane keine dichten Monolagen auf Aluminium bilden, werden in diesem Fall Moleküle mit einer Phosphonsäure-Ankergruppe zur Herstellung der selbstorganisierenden Monolage verwendet. Die Verwendung von strukturierten Steuerelektroden erlaubt die Herstellung von mehreren Feldeffekttransistoren mit voneinander unabhängigen Steuerelektroden und somit die Realisierung einfacher Logikschaltungen, die aus mehreren Feldeffekttransistoren auf demselben Substrat bestehen. Ferner wird gezeigt, dass die auf einzelnen Nanoröhren basierenden Feldeffekttransistoren eine Lebensdauer besitzen, welche es erlaubt, sie öfter als 10^4 mal zwischen dem Ein- und Aus-Zustand hin und her zu schalten, sowie sie länger als 200 Tage unter Umgebungsbedingung aufzubewahren, ohne dass eine Degradation der Leistungsfähigkeit der Feldeffekttransistoren festzustellen ist.

Der zweite Teil dieser Arbeit beschäftigt sich mit der elektrochemischen Modifizierung einzelner einwandiger Kohlenstoffnanoröhren durch den organischen Magneten *Berliner Blau*. Während die elektrischen Eigenschaften der metallischen SWCNTs sich im Zuge der elektrochemischen Modifizierung sich nicht ändern, werden halbleitende Nanoröhren durch *Berliner Blau* stark p-dotiert. Durch die Messung der Temperaturabhängigkeit des Widerstandes der dotierten halbleitenden Nanoröhren wurde festgestellt, dass bei Temperaturen unter etwa 150 K die dotierende Wirkung verloren geht.

Im dritten Teil dieser Arbeit werden neuartige Cyano-substituerte Perylen-Carboxyl Diimid-Derivate zur Herstellung von luft-stabilen n-Kanal Feldeffekttransistoren verwendet. Verschiedene organische Halbleiter, welche sich durch den Fluor-Gehalt und die Geometrie der Endgruppen unterscheiden, werden hierzu herangezogen. Der Zusammenhang zwischen der Struktur der organischen Schichten und der Luftstabilität der Ladungsträgerbeweglichkeit wird untersucht. Es wird festgestellt, dass, im Gegensatz zu früheren Berichten in der Literatur, die Luftstabilität nicht vom Redoxpotential der Moleküle abhängt. Des Weiteren werden FETs, in welchen der Kanal aus kristallinen Drähten eines der Moleküle besteht, untersucht. Die nanoskopischen Drähte bilden sich durch Selbstorganisation aus einer Lösung. Aufgrund der hohen kristallinen Ordnung der Drähte haben die Feldeffekttransistoren eine hohe Beweglichkeit von bis zu 0.2 $\mathrm{cm}^2/\mathrm{Vs}$, sowie eine höhere Luftstabilität als Feldeffekttransistoren, die aus dünnen Schichten derselben Verbindung aufgebaut sind.

Der letzte Teil dieser Arbeit beschreibt eine neue Methode zur Herstellung von Polymernanodrähten, deren Durchmesser bis zu 25 nm herunterreicht. Die Drähte konnten in einem Rotationsbeschichtungsvorgang aus einer Polymerlösung hergestellt werden. Die Bildung der Drähte wird auf die Raleigh-Taylor Instabilität der Polymerschicht während des Rotationsbeschichtungsvorganges aufgrund des Wechselspiels von Zentrifugal- und Laplace-Kraft, welche auf die Oberflächenkrümmung des Polymerfilms zurückgeht, zurückgeführt.

Schlagworte: Kohlenstoff Nanoröhrchen, Feld Effekt Transistor, Selbstorganisierende Monolage, Elektrochemie, Berliner Blau, Dünnfilm Feld Effekt

Transistor, Perylen Diimid, Luftstabilität, Rotationsbeschichtung, Raleigh-Taylor Instabilität, Polymernanodraht.

Contents

Chapter 1

Introduction

Nanotechnology is an interesting and vibrant field of research. Its roots can be traced back to Feynman's famous lecture in 1959, in which he suggested that for entities with nanoscopic dimensions new physical phenomena should arise [1], if only one were able to manufacture and visualize such objects.

Nowadays, nanotechnology has advanced quite far. Efficient fabrication techniques for objects with nanoscopic dimensions are available and new phenomena occurring at the nanoscale can be investigated. These include advanced microscopy methods like electron microscopy [2] and scanning tunneling microscopy (STM) [3, 4], as well as high-resolution fabrication techniques, such as electron-beam lithography or molecular beam epitaxy [5]. These techniques enable the fabrication of nanoscale objects, such as thin metal strips with a width of 10 nm and their characterization with atomic resolution. This fabrication approach is usually called 'top-down'.

An alternative concept of fabricating nanoscale objects is called 'bottom-up'. In this approach, atomic and/or molecular building-blocks form ordered structures as a result of driving forces inherent to the system. To understand these processes, it is revealing to approach the topic from common crystal growth. Crystals, such as silicon monlithes grown for the semiconductor industry, form when the system approaches thermodynamic equilibrium. Here, usually only one type of bonding (for example covalent bonding in the case of silicon) dominates the crystal growth. In contrast, when nanoscopic building blocks such as the self-organization of organic molecules is considered, different kinds of bonding interactions are frequently present in parallel. For example, ionic, hydrogen or metal-ligand type interactions that can be unidirectional have to be considered. Furthermore, the interaction of the building blocks with their surrounding, such as interfaces, has to be considered. The ordering of the building blocks towards their thermodynamically most stable configuration leads to the formation of highly ordered nanoscopic structures that can be different from the structures of the undisturbed crystal. For example, benzoic acid molecules have been shown to form highly ordered chains upon deposition onto a gold single crystal.[6]

Even more complex structures can be achieved if the system's drive towards the thermodynamically most stable configuration is impeded by kinetics (i.e. the flux of nanoscopic building blocks to the growth area) for example. In the case that kinetics dominate the growth, metastable structures can be formed. An example is the growth of silver dendrites on a platinum crystal.[7]

In summary, self-organized growth of highly ordered nanoscopic structures on surfaces is determined by the relative magnitudes of (1) the interaction between the building-blocks and the substrate versus the interaction between the building-blocks among each other (i.e the thermodynamics) and (2) the thermodynamics versus the kinetics.[8]

Due to the nanoscopic dimensions of the objects under investigation, not only are novel fabrication techniques such as the described bottom-up approach of interest, but also new physical phenomena arise. Especially relevant for microelectronics is the fact that in nanoscale objects the movement of electrons is frequently confined to one or two dimensions, if the object's lateral dimensions are on the same order of magnitude as the Fermi wavelength of the electrons. This confinement might also lead to further novel phenomena, such as blockade of transport through such a structure by the Coulomb repulsion. A third example concerns the interactions of nanoscopic objects with their immediate environment. Due to their large surface-to-volume ratio, their properties can be strongly influenced by their surroundings or modifications of their surface. This property can be used for implementing new functionalities to the system, which will be utilized in Chapter 4 for the implementation of new functionalities in single-walled carbon nanotube field-effect transistors.

1.1 Organic functional materials for electronic applications

Although the initial discovery that organic materials can have semiconducting properties dates back to the 1940s [9], it took more than 40 years until it was perceived that they could be used in thin-film field-effect transistors (FETs). The first experimental realization of organic FETs dates back to the 80s, in which Tsumura et al. [10] and Horowitz et al. [11] first demon-

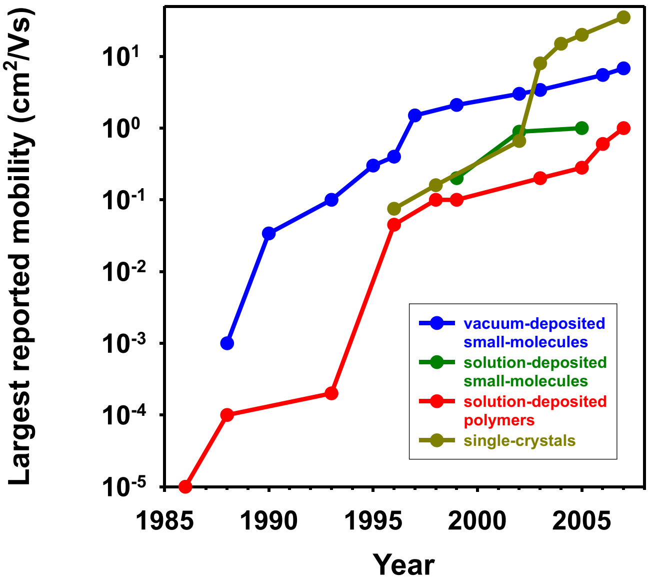

Figure 1.1: Development of the charge carrier mobility in organic semiconductors over the last decades.[12]

strated thin-film FETs based on polythiophenes and sexithienyl, respectively. While the performance of these FETs was rather limited, their performance has continuously improved over recent years, as exemplified by the development of the mobility with time in Figure 1.1. Nowadays, organic FETs are promising alternatives to thin-film FETs based on amorphous silicon. Since such silicon FETs are frequently used in commercially available active-matrix liquid-crystal displays, similar commercial applications are envisaged for organic FETs in the future [13].

The reason why organic materials have recently gained significant attention for applications in electronic devices is twofold. First, the use of organic functional materials offers the possibility of combining unconventional fabrication techniques such as solution-processing [14], self-assembly from the solution or gas phase [15], and printing techniques [16] that are not feasible for inorganic materials. These techniques allow for a separation of the synthesis of the organic materials (often performed at elevated temperatures [17]) from their deposition onto unconventional substrates such as plastic foils (these substrates would not sustain the elevated temperatures that are present during the synthesis of the molecules). Second, the selectivity and ease with which organic chemistry allows the properties of these materials to be tailored, promises the rational and deterministic design of functional organic entities for desired purposes.

Miniaturization of organic FETs to nanoscopic dimension is a very promising and important extension towards their use as functional entities in electronic devices. This is because the described novel phenomena present at nanoscale dimensions, such as a larger surface-to-volume ratio, can then be combined with the bottom-up fabrication approach and the possibility to adjust the functionalities of organic building blocks. Furthermore, such nanostructured organic entities may become promising candidates in the miniaturization of electronic circuits which is driven by the semiconductor industry.

In this thesis, nanoscale organic structures are investigated as components of functional organic devices. The materials under consideration offer certain advantages over conventionally-used organic materials. For example, single-walled carbon nanotubes (SWCNTs) are utilized as channels in FETs. Due to their one-dimensional nature and high structural quality, they allow for the fabrication of high-performance FETs. A second class of organic molecules under investigation are core-cyanated perylene tetracarboxylic diimide derivatives. These molecules allow for the fabrication of thin-film as well as nanobelt FETs and therefore enable a direct comparison between transistor performance and crystalline structure. In the following, a brief introduction to both materials is given.

1.1.1 Single-walled carbon nanotubes

Single-walled carbon nanotubes (SWCNTs) are macromolecules that can be imagined as a rolled-up graphene sheet (a monoatomic layer of graphite). A schematic depiction of a SWCNT is shown in Figure 1.2. It consists exclusively of carbon atoms with sp^2 hybridization that leaves one electron per carbon atom in delocalized π-orbitals. Depending on the way the nanotube is rolled up, it will either be metallic or semiconducting (i.e. have a finite density of states or no allowed states at the Fermi energy).

The roll-up direction is expressed by the so-called chiral vector $\vec{c} = n\vec{a_1} + m\vec{a_2}$ with $n \geq m$ as two integers and $\vec{a_1}$ and $\vec{a_2}$ being the lattice unit vectors of graphene [19]. The chiral vector uniquely identifies a (n, m) SWCNT. The diameter d of SWCNTs is given by $d = |\vec{c}|/\pi$. Typical diameters of nanotubes as observed in experiment are between 0.4 and 3 nm. SWCNTs can be up to a few centimeters in length. If $n = m$, the resulting tube is called armchair; if $m = 0$, the tube is called zig-zag, while all other combinations of n and m result in so-called chiral tubes. If the relation $m - n = 3i$ is satisfied, with i being an integer, a nanotube is metallic. Otherwise, a tube is semiconducting. Thus, all armchair nanotubes (n,n) are metallic, whereas

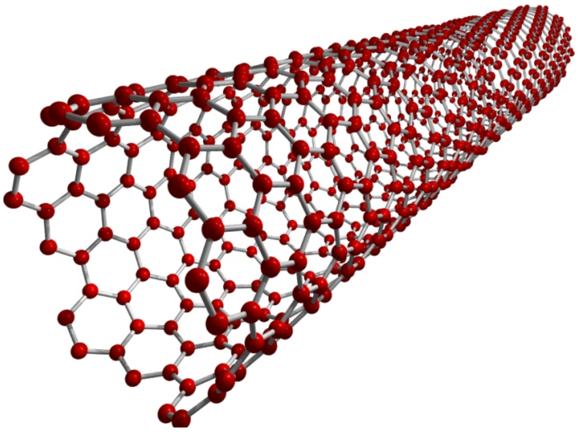

Figure 1.2: Scheme of a single-walled carbon nanotube (adopted from [18]).

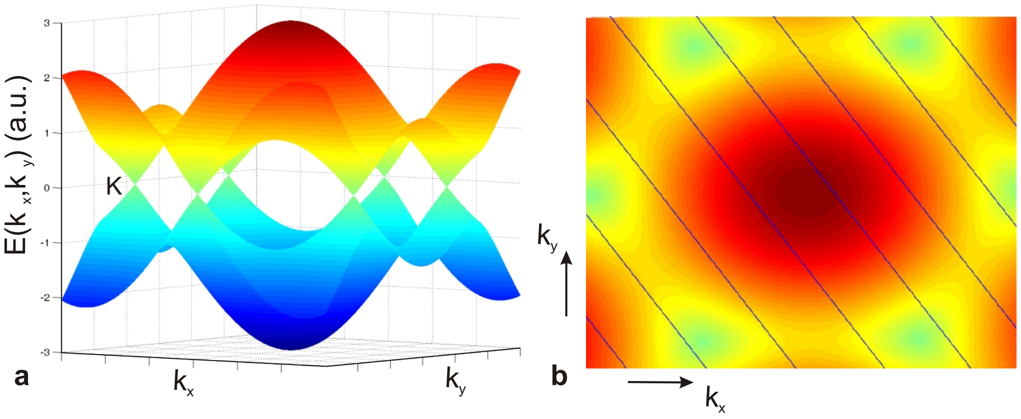

Figure 1.3: **(a)** Dispersion relation of graphene as calculated according to Equation 1.1. At the K points the conduction and valence band meet. **(b)** Dispersion relation of graphene viewed from top. The allowed wavewectors $\vec{k}$ lie on the black lines. The color represents the energy $\mathrm{E(k_x, k_y)}$.

zig-zag (n,0) and chiral (n,m) nanotubes can be metallic or semiconducting. SWCNTs are one-dimensional objects and as such have a very high aspect ratio. Their one-dimensional character originates from the fact that the Fermi wavelength of the charge carriers λ is comparable to the typical diameter of carbon nanotubes. This introduces periodic boundary conditions for the allowed wave vectors and leads to a quantization of the wave vector perpendicular to the axis of the tube $k_{\perp,q}$. The allowed wave vectors are restricted to values of $m \cdot 2\pi/k_{\perp,q} = q \cdot \lambda = |\vec{c}| = \pi d$, with q being an integer. The wave vector in the direction of the tube axis is not quantized. It follows that the allowed $\vec{k}$ vectors lie on parallel lines on the dispersion relation of graphene with a distance of $2/d$ (see Figure 1.3b). In the limit $d \to \infty$, the distance between these lines goes to zero, and the dispersion relation of graphene is recovered.

Depending on whether one of the allowed wave vectors for a SWCNT goes through the K point of the dispersion relation of graphene (at the K point the conduction and valence band of graphene are degenerate, see Figure 1.3a) or not, the SWCNT is either metallic or semiconducting. The dispersion relation of the SWCNT follows from the dispersion relation of graphene [20]

$$E_{graph}(k_x, k_y) = \pm t \sqrt{1 + 4\cos\left(\frac{\sqrt{3}}{2}k_x a\right)\cos\left(\frac{1}{2}k_y a\right) + 4\cos^2\left(\frac{1}{2}k_y a\right)} \quad (1.1)$$

by imposing appropriate boundary conditions that depend on the chiral vector of the tube of interest. In Equation 1.1, a ($= 2.46$ Å) is the lattice constant of graphene . For example, the dispersion relation of an armchair SWCNT (n, n) can be obtained by introducing the quantization condition $\sqrt{3}n \cdot a \cdot k_x = 2\pi q$ for the wave vector k_x which renders Equation 1.1 to [21]

$$E_{SWCNT}(k) = \pm t \sqrt{1 \pm \cos\left(\frac{q\pi}{n}\right)\cos\left(\frac{k_y a}{2}\right) + 4\cos^2\left(\frac{k_y a}{2}\right)}, \quad (1.2)$$

with $(-\pi/a < k < \pi/a)$ and q=1,...,n. Here, k_y is the wave vector in the direction of the tube axis.

The electronic density of states can be obtained by integrating the inverse of the slope of the energy dispersion of the SWCNT. It is given by

$$D(E) \propto \sum \frac{E}{\sqrt{E^2 - E_q^2}}, \quad (1.3)$$

with q as the index of the subband.

The electronic density of states of a semiconducting carbon nanotube as function of the energy is depicted in Figure 1.4. It displays a vanishing density of states at the Fermi energy and peaks at certain positions E_q. These so called van Hove singularities are characteristic of one-dimensional systems [22].

Due to the one-dimensional nature of carbon nanotubes, carrier motion is confined to the direction of the long axis of the tube. This leads to a reduced scattering of the charge carriers, since during a scattering process both energy and momentum of the charge carrier have to be conserved. As the density

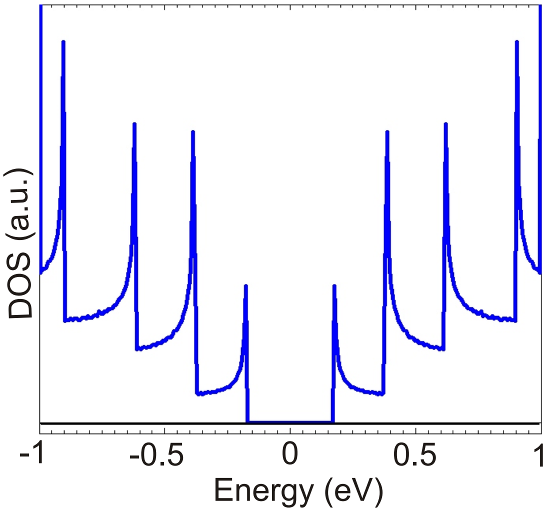

Figure 1.4: Electronic density of states (DOS) as function of energy for a semiconducting (10,0) nanotube, after [18].

of final states that electrons could scatter into is strongly reduced due to the one-dimensional nature of the SWCNT, scattering in one-dimensional objects is strongly suppressed. This is why SWCNTs can carry current densities up to 10^9 A/cm^2 [23]. The ballistic nature of conduction in SWCNT remains preserved even though SWCNTs are usually not completely free of defects which act as scatterers. The reason is that their tubular structure allows for the disorder to be smoothed out across the diameter of the tube [24].

1.1.2 Small organic molecules

Small organic molecules like pentacene ($C_{22}H_{14}$, consisting of five linearly fused benzene rings, shown in the inset of Figure 1.5) possess an energy gap separating their highest unoccupied molecular orbital (HOMO) and their lowest occupied orbital (LUMO)[9]. Therefore they can be used to build FETs.

The use of small organic molecules for the fabrication of FETs is especially interesting, since different types of molecules with tailored functionality can be synthesized by organic chemistry. For example, both n-type and p-type FETs can be fabricated from organic molecules, which will allow the implementation of complementary circuits with low power consumption, high operation frequency, and sufficient robustness against device parameter variations and external noise.

Organic FETs normally comprise thin films composed of small molecules like pentacene (the prototype of organic semiconducting small molecules) or the core-cyanated perylene tetracarboxylic diimides compounds investigated in this thesis, in strong contrast to the SWCNT FETs that are based on a single SWCNT. The molecules are interacting only by van-der-Waals forces, which are weak in comparison to covalent bonds. Hence, it is not straightforward to fabricate molecular crystals of high quality. Moreover, the properties of the FET are determined both by the properties of the individual molecules as well as the way these molecules self-organize into films.

Charge transport between the molecules cannot be described by a universal approach like the band model for metals. The charge transport through the organic material depends significantly on the relative alignment of adjacent molecules as well as on the interaction of the charge carriers with the individual molecules. For example, in very pure naphthalene crystals at low temperatures the transport can be described adequately in a band model [25]. This means that charge carriers can move through the crystal very fast (i.e have a high mobility, defined on page 21). At room temperature, however, the band model cannot be applied due to the strong localization of the charge carriers on the individual molecules. This localization arises due to the weak electronic overlap between neighboring molecules, which leads to a low charge carrier mobility [25]. As a consequence, the charge carriers interact strongly with the environment, such that transport in molecular crystals is usually described by introducing the quasiparticle polaron. This model takes the relaxation (i.e. the scattering) of the charge carriers via vibronic, electronic and phononic channels into account.

With regard to possible applications of organic FETs it is essential to achieve high charge carrier mobilities. However, its not straightforward to produce large molecular crystals. Accordingly, thin polycrystalline films of organic molecules are investigated as they can be prepared much more easily. In these, at the boundaries between the individual grains a large number of defects are introduced that hinder the charge transport through the crystal. Experimentally it can be found (and was also demonstrated in this thesis in chapter 5), that the mobility of the charge carriers critically depends on the relative alignment of the individual crystallites in a thin film. This has been shown, for example, for a polycrystalline film of pentacene (Figure 1.5) by X-ray diffraction [26].

Further complications that arise from the use of imperfect layers of organic molecules are that both the molecule as well as the films are prone to degradation by effects like photooxidation [27]. This process is accompanied by a rearrangement of the oxidized molecules in the film. Both processes lead to a degradation of the carrier mobility over time.

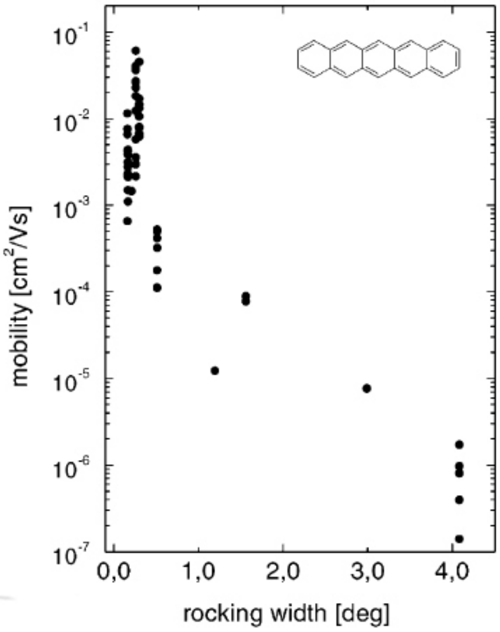

Figure 1.5: Charge carrier mobility as a function of the rocking width of a polycrystalline film of pentacene (its structure is shown in the inset), which is a measure of the angular spread of the orientation of the pentacene crystallites. The charge carrier mobility measured for FETs fabricated from the respective films is displayed on the y-axis and is found to significantly depend on the alignment of the crystallites (adapted from [26]).

Despite the relative ease with which organic molecules can be synthesized today, there is no clear understanding of how to predict the crystal structure that a molecule will take, and which impact the properties of the individual molecule, as well as the crystal structure, will have on the stability of the mobility under air exposure.

1.2 Organization of this thesis

This thesis is organized as follows. In Chapter 2, a brief introduction into FETs is given. The drain current will be discussed in the different operational regimes. To this end the drain current is explicitly calculated from the derived formulae. Chapter 3 is devoted to the fabrication of high-performance SWCNT FETs with an organic gate dielectric based on 2 nm thick self-assembled monolayers (SAMs). While a silane-based SAM allows for the fabrication of FETs in a global back-gate geometry, FETs with structured alumium gates are realized based on a phosphonic acid SAM. The shelf life and the operational stabilty of the FETs are investigated. The electrochemical modification of individual SWCNTs with the organic magnet Prussian Blue (PB) is described in Chapter 4. The temperature dependence of the modified tubes is discussed and compared with calculations performed in Chapter 2. In Chapter 5, five core-cyanated perylene carboxylic diimides end-functionalized with fluorine-containing linear and cyclic substituents are employed as air-stable n-channels in thin-film FETs. The relationships between molecular structure, morphology, transistor performance, and air-stability are investigated. The FET performance is compared to the characteristics of FETs based on self-assembled nanoribbons obtained from one of the compounds. Finally, in Chapter 6, a novel method of manufacturing nanoscale polymer fibers of diameters as small as 25 nm is demonstrated. The fiber formation proceeds without the need for a mechanical constriction as in electro- or meltspinning. The influence of the spin-speed, viscosity, concentration of the polymer solution on the fiber formation, as well as theoretical investigations of the relevant forces for the fiber formation are discussed. The thesis is concluded with a summary of the work and an outlook in Chapter 7.

Chapter 2

Fundamentals of field effect transistors

The field effect transistors (FETs) fabricated in this thesis were characterized by electrical measurements. The interpretation of the obtained electrical data is based upon a theoretical framework that will be discussed in this chapter. The concepts presented here rely mainly upon the standard MOSFET textbook approach [28], but are slightly altered since organic as well as SWCNT FETs do not operate in inversion but in accumulation mode. In MOSFETs, the charge carriers in the conducting channel are electrons, but the semiconducting channel is slightly p-doped (inversion mode). Doping stems from the incorporation of chemical impurities into a crystal that do not have the same valency as the host crystal. In contrast, SWCNTs and organic FETs are not deliberately doped, and the channel is formed by the accumulation of holes or electrons.

In this chapter it will be shown that the FET-behavior can be explained with a single assumption for the subthreshold and saturation regime, in contrast the separate approaches used in most textbooks [28]. Furthermore, the temperature dependence of the conductance of a doped semiconductor will be derived. This formula will be used to interpret the temperature dependent measurements of the conductance of doped SWCNTs (chapter 4). At the end of the chapter, the applicability of the derived formula will be discussed for FETs based on SWCNTs and organic small molecules.

2.1 Introduction

The development of the transistor begun with the discovery of the bipolar transistor in 1947 by Bardeen, Brattain and Shockley [29] [30]. This was the first realization of a three-terminal solid-state device and revolutionized the electronics industry. It consists, for example, of two p-n junctions back to back, i.e., a p-n-p structure. One terminal is connected to each of the sections. The current flowing between the two p-type parts of the device can be tuned by the application of a voltage to the n-type terminal.
A different approach to transistors was developed at the same time. It was the so-called field effect transistor (FET). The first metal-oxide-semiconductor FET (MOSFET) was realized in 1960 by Kahng and Atalla [31]. The schematic structure of a MOSFET is shown in Figure 2.1. The semiconducting channel is connected to two terminals (labeled source (S) and drain (D)) that are used to apply a voltage along the channel, whereas the third terminal (labeled gate (G)) is electrically insulated from the semiconducting channel. It serves to control the electrostatic potential at the semiconductor/insulator interface. There are different types of FETs that can be distinguished by the way the gate is coupled to the channel. The currently most commonly used type is the MOSFET in which the gate capacitor is formed by an insulator, (for example SiO_2) between the metallic gate electrode and the semiconducting channel. Other types of FETs are the junction FET (JFET) and the metal-semiconductor FET (MESFET) in which the gate capacitor is formed by a depletion layer.

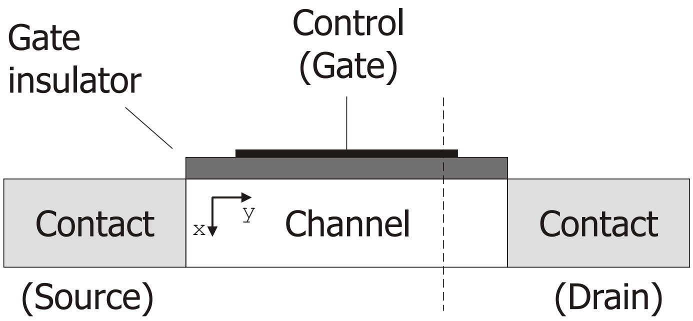

Figure 2.1: Schematic depiction of a FET. The band diagram of the metal-insulator-semiconductor capacitor along the direction of the dashed line is shown in 2.3.

Device layout

A more detailed scheme of an FET, corresponding to those studied in this thesis is depicted in Figure 2.2. The FETs usually rely on a heavily doped silicon wafer that is used as back-gate electrode and as the substrate. The substrate is coated with an insulating layer called gate dielectric. The FETs investigated in this thesis typically utilize either thermally grown SiO_2 of 100 nm thickness or an organic self-assembled monolayer (SAM). On top of this gate insulator, the semiconducting material (SWCNTs or organic molecules) are deposited. Source and drain metal electrodes are then defined by lithographical or shadow-mask techniques to complete the device.

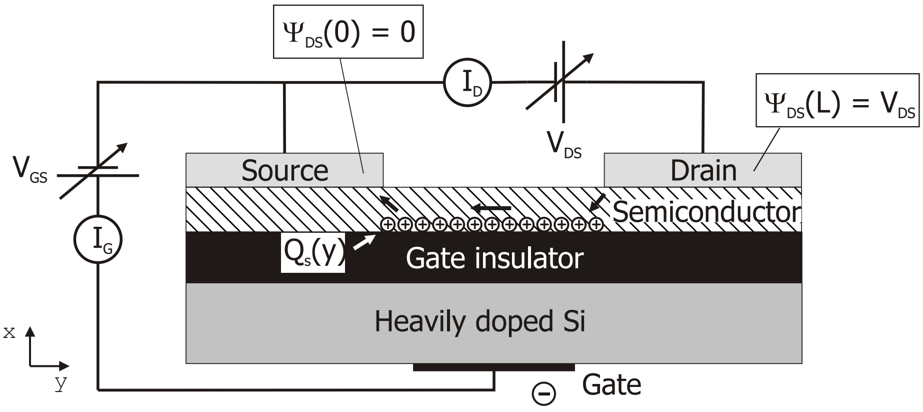

Figure 2.2: Scheme of a typical FET used in this work. $Q_s(y)$ is the space charge per unit area at position y between source and drain. The conducting channel Q_s is composed of holes in the depicted case, since a negative potential is applied to the gate. $\psi_{DS}(y)$ denotes the potential drop of V_{DS} across the channel.

2.2 Current-voltage characteristics of FETs

Operation principle of FETs

In FETs, the current through the channel (called the drain current I_D) is modulated by controlling the electrostatic potential of the channel through the application of a voltage between the gate and the source terminal (V_{GS}). In order for this potential change to affect the current through the channel, it has to alter the concentration of charge carriers in the channel. This can be seen from the Drude model

$$I_D \propto \sigma \cdot V_{DS} = p \cdot e \cdot \mu \cdot V_{DS}. \tag{2.1}$$

Here, σ is the conductivity of the channel, p the density of charge carriers in the channel, μ the mobility of the charge carriers and V_{DS} the voltage applied between the source and drain electrode. The current I_D flows because of the potential difference V_{DS} between the source and the drain electrode. μ is given by $\mu = e\tau/m^*$ with τ the time between two scattering events (relaxation time) and m^* the effective mass of the charge carriers. Since μ is usually not affected by the electrostatic potential, the modulation of the drain current results from the modulation of the charge carrier density in the semiconducting channel. In a semiconductor, the density of holes p in the conduction band depends exponentially on the separation of the Fermi level $\mathrm{E_F}$ to the valence band $\mathrm{E_V}$ [28]

$$p = N_V exp\left(\frac{E_V - E_F}{k_B T}\right). \tag{2.2}$$

In a FET, by changing $E_V - E_F$ through application of a gate voltage, the carrier density at the surface of the semiconductor can be influenced.

When the maximal density of charges is accumulated, the maximum drain current I_D flows, and the FET is in its on state. In Figure 2.2, the case in which holes accumulate and form a conductive channel between source and drain electrode upon application of a negative bias to the gate electrode is shown. Whether it is energetically more favorable for holes or electrons to accumulate in the channel depends on the sign and magnitude of the applied gate voltage as well as on the band gap and doping level of the semiconductor. In turn, if the charge density is minimal, the current through the channel is small and the FET is turned off. The ratio between the on and the off state (on/off ratio) is an important parameter determines the quality of a FET. Since FETs are used as electronic switches, the on/off ratio should be as large as possible. However, the operation of a FET is not only determined by the density of accumulated charges in the channel. In order for a large current I_D to flow through the device, charges have to be injected into the channel from the source contact. For example, the successful injection of charge carriers from the source electrode into the channel depends on the alignment of the conduction (in the case of an electron channel) or valence (in the case of a hole channel) band with the Fermi level of the metal used for the drain contact. The contact of a metal and a semiconductor leads to a potential barrier (Schotty barrier) that can hinder charge transport across this interface [28]. In case that the channel is composed of an inorganic material, the thickness of the Schottky barrier can be tuned by selective doping of the contacts. In contrast, when organic materials are used, doping is typically not straightforward and special care has to be directed to the choice of the combination of semiconductor and contact metal. This problem will be addressed in more detail in chapter 5 on FETs made from small organic molecules.

In order to illustrate the modulation of the charge carrier density at the surface of the semiconductor, the effect of a potential at the semiconductor/insulator interface will be discussed and finally the space charge per unit area Q_s at this interface will be derived. The knowledge of Q_s allows for the calculation of the drain current I_D, as will be discussed in detail for different values of the gate-source and drain-source voltages. This will serve as the basis for understanding the operation of the FET in regimes of different relative magnitudes of $\mathrm{V_{DS}}$ and $\mathrm{V_{GS}}$. Furthermore, important transistor parameters will be defined in these regimes.

2.2.1 Space charge density in the channel

The density of free holes in a p-doped semiconductor at low temperatures is given by

$$p = \frac{N_V n_A}{n_D} \exp\left(-\frac{E_a}{k_B T}\right), \tag{2.3}$$

where n_A is the concentration of acceptors, n_D the concentration of donors, N_V the effective density of states of the valence band, E_a the activation energy of the dopants, k_B Boltzmann's constant and T the temperature [32]. This relation is only valid if no external potential changes the electrostatic potential in the semiconductor. The modification of the electrostatic potential (e.i. the shift of the Fermi level) leads to a bending of the bands relative to the Fermi level. In Figure 2.3, the band structure of a metal-insulator-semiconductor (MIS) capacitor is shown. This capacitor is formed by the metal gate electrode, the gate insulator and the doped channel (Figure 2.1). The application of a bias to the gate electrode can be accounted for by introducing a potential $\phi(x)$. For this potential, $\phi(x \to \infty) = 0$ is fulfilled, which means that Equation 2.3 is valid far away from the semiconductor/insulator interface.

In the vicinity of this interface, the density of charge carriers is given by

$$n_\phi(x) \quad = \quad n \cdot \exp\left(\frac{e\phi(x)}{k_B T}\right)$$

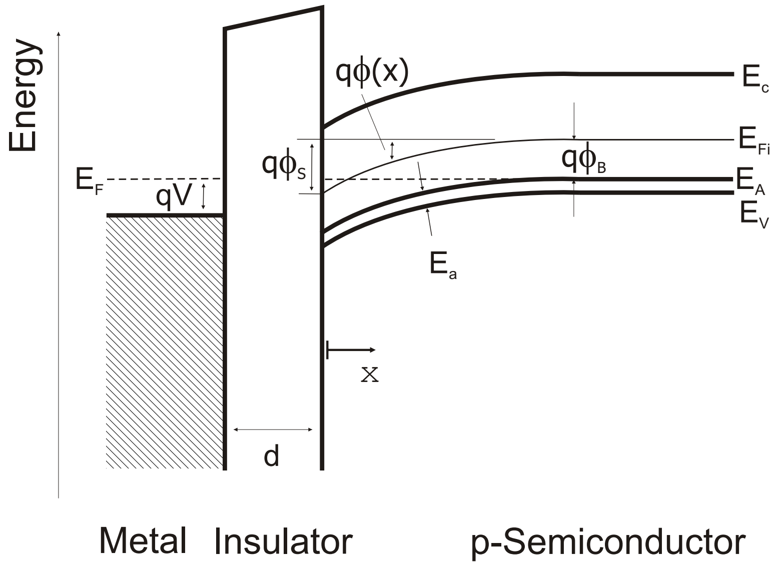

Figure 2.3: Energy band diagram of a metal-insulator-semiconductor structure along the direction of the vertical dashed line in Figure 2.1. At the depicted bias V, electrons are accumulated at the semiconductor/insulator interface. The surface potential is defined as $\phi_s \equiv \phi(x = 0)$.

$$p_\phi(x) = p \cdot \exp\left(-\frac{e\phi(x)}{k_B T}\right) \tag{2.4}$$

where n and p are the bulk electron and hole densities as given by Equation 2.3, $\phi(x) = (E_{Fi}(x) - E_{Fi}(\infty))/e$ with e as the elementary charge, and $E_{Fi}(x)$ is the intrinsic Fermi level (i.e. the middle of the bandgap) at position x. The relation between the potential $\phi(x)$ and the charge density created by $\phi(x)$ is given by the one-dimensional Poisson equation [28]

$$\frac{d^2\phi}{dx^2} = \frac{-\rho(x)}{\varepsilon_0 \varepsilon_r} \tag{2.5}$$

with ε_0 as the electric permittivity of the vacuum, ε_r the relative permittivity of the semiconductor and $\rho(x)$ as the excess charge density that arises due to the bending of the bands at the surface of the semiconductor. $\rho(x) = e(p_\phi(x) - p - (n_\phi(x) - n(x)))$ is given by

$$\rho(x) = e\left(p\left[exp\left(-e\frac{\phi(x)}{k_B T}\right) - 1\right] - n\left[exp\left(e\frac{\phi(x)}{k_B T}\right) - 1\right]\right). \tag{2.6}$$

In the bulk of the semiconductor ($x \to \infty$) the band bending disappears ($\phi(x \to \infty) = 0$) and therefore $\rho(x \to \infty) = 0$, which accounts for the requirement of charge neutrality in the bulk. If $\rho(x)$ in Equation 2.5 is expressed by Equation 2.6, the space charge per unit area Q_s that is accumulated by the band bending can be calculated by integration of Equation 2.5 over the potential from the bulk to the semiconductor/insulator interface (from $\phi = 0$ to $\phi = \phi_s$). The integration yields

$$Q_s = \mp\sqrt{2\varepsilon_0\varepsilon_r k_B T}\sqrt{\left[p(e^{-\frac{e\phi_s}{k_BT}} + \frac{e\phi_s}{k_BT} - 1) + n(e^{\frac{e\phi_s}{k_BT}} - \frac{e\phi_s}{k_BT} - 1)\right]}. \quad (2.7)$$

Here the relationship between the surface potential and the electric field at the surface was used to express Q_s [28]

$$\int_0^{\phi_s} \frac{d^2\phi}{dx^2}d\phi = \frac{1}{2}E_s^2 \qquad \text{since} \qquad \frac{d\phi}{dx} = -E \quad (2.8)$$

where E_s is the electric field created by Q_s at the surface of the semiconductor. By using the Poisson equation again, Equation 2.8 can be transformed into $Q_s = -\varepsilon_0\varepsilon_r E_s$ with the aid of the Gaußlaw.

This derivation is not limited to neither an excess electron nor hole concentration. If, for example, a p-doped semiconductor is considered for which the free electron density n in Equation 2.7 is significantly smaller than p, the evolution of Q_s with ϕ_s can be calculated, as illustrated in Figure 2.8.

2.2.2 Calculation of the drain current

From Equation 2.7 the complete current-voltage characteristics of the FET can be calculated. To this end, the influence of a drain-source voltage V_{DS} has to be included. This voltage creates the electric field in which the charges Q_s move from the source to the drain electrode. It is assumed that V_{DS} drops linearly along the whole channel.[1] This is accounted for by including a potential $\psi_{DS}(y)$ that lowers ϕ, such that the hole concentration as given by Equation 2.4 reads

$$p_\phi(x) = p \cdot e^{-\frac{e(\phi_P(x)-\psi_{DS}(y))}{k_BT}}. \quad (2.9)$$

---

[1] In addition it is assumed that the electric field E_x (created by the gate-source voltage) in the direction perpendicular to the insulator/semiconductor interface is much larger than the electric field E_y (created by the drain-source voltage) in parallel to the insulator/semiconductor interface. This approximation is called the gradual channel approximation [28].

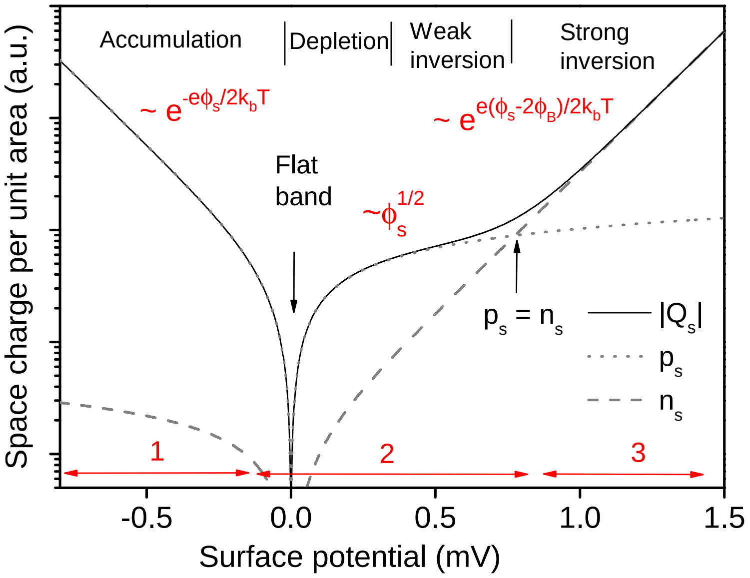

Figure 2.4: Variation of the space charge per unit area Q_s in a MIS-structure with the surface potential (calculated with MATLAB from Equation 2.7). The space charge per unit area is plotted separately for electrons (n_s, dashed) and holes (p_s, dotted). The electron concentration was assumed to be 10^6 times smaller than the hole concentration. In the three different regions (marked in red), the space charge per unit area is proportional to the terms shown in red.

The electron concentration is equally influenced by ψ_{DS}. This renders equation 2.7 to

$$Q_s(y) = \sqrt{\mp 2\varepsilon_0\varepsilon_r k_B T}\left[p(exp\left(-\frac{e(\phi_s-\psi_{ds})}{k_BT}\right)+\frac{e\phi_s}{k_BT}\right.$$

$$\left.-exp\left(\frac{e\psi_{DS}}{k_BT}\right))+n(exp\left(\frac{e(\phi_s-\psi_{DS})}{k_BT}\right)-\frac{e\phi_s}{k_BT}-exp\left(\frac{e\psi_{DS}}{k_BT}\right)\right]^{\frac{1}{2}}. \quad (2.10)$$

The drain current is given by

$$I_D = \frac{Z}{L}\int_0^L |Q_s(y)|v(y)dy, \quad (2.11)$$

with L being the length of the channel and Z its width. If the mobility is assumed to be independent of the applied drain bias, i.e., $v(y) = E(y)\mu =$

$\frac{\psi_{DS}(y)}{dy}\mu$, Equation 2.11 reads

$$I_D = \mu \frac{Z}{L} \int_0^{V_{DS}} |Q_s(y)| \frac{d\psi_{DS}(y)}{dy} dy. \tag{2.12}$$

For general values of V_{DS} and ϕ_s the integration of 2.12 cannot be carried out analytically. This is why most textbooks incorporate simplifications at this point for the space charge density to analytically derive the current [28]. However, for certain values of ϕ_s Equation 2.10 can be approximated and then solved analytically. These distinct regions are characterized by the domination of the hole or electron concentration. These regions are marked in red in Figure 2.4:

***Region 1*, in which $Q_s \propto exp(\phi_s/2k_BT)$:**
When ϕ_s is significantly smaller than 0, $p \gg n$ which is why this region is called hole accumulation region. This is the region in which the FETs investigated in this thesis are operated.

***Region 2*, in which $Q_s \propto \sqrt{\phi_s}$:**
This linear proportionality between Q_s and $\sqrt{\phi_s}$ is valid for different values of ϕ_s, specifically:
- For small negative and small positive ϕ_s. Here, the holes in the channel are depleted which is why this area is called depletion.
- For slightly larger ϕ_s, the concentration of electrons at the surface is starting to approach the concentration of holes, which is why this region is called weak inversion. In this region the current that flows through the device is small, i.e., the FET is in the off state.

***Region 3*, in which $Q_s \propto exp[(\phi_s - 2\phi_B)/2k_BT]$:**
If the surface potential is larger than $2\phi_B$, the electron concentration exceeds that of the holes which is why this region is called strong inversion. This is the region in which single-crystal silicon MOSFETs are typically operated in.

From Figure 2.4 it is apparent that in principle a FET can be operated in either the accumulation or the strong inversion regime, since in both regimes the carrier concentration can be changed by the surface potential over several orders of magnitude. In the following, the influence of the surface potential on the drain current in *region 1* will be discussed in detail, since this is the relevant region for the FETs investigated in this thesis. The calculation of the drain current in *regions 2* and *3* is described only briefly.

2.2.3 Drain current in the accumulation region (region 1)

In the accumulation regime, Q_s is dominated by the exponential increase of the hole concentration as a function of ϕ_s. By neglecting the contribution of electrons and the linear increase of the hole concentration as a function of $\sqrt{\phi_s}$ in 2.10 it follows for Q_s

$$Q_s = \mp\sqrt{2\varepsilon_0\varepsilon_r k_B T}\sqrt{p(e^{-\frac{e(\phi_s-\psi_{DS})}{k_B T}} - e^{\frac{e\psi_{DS}}{k_B T}})}. \tag{2.13}$$

With Equation 2.12 it follows for I_D

$$\begin{aligned} I_D(V_{DS}, V_{GS}, T) &= \mu\frac{Z}{L}\sqrt{2p\varepsilon_0\varepsilon_r k_B T}\frac{2k_B T}{e}\left(1 - \exp\left(\frac{V_{DS}}{2k_B T}\right)\right) \\ &\sqrt{\exp\left(-\frac{e\alpha(V_{GS} - V_{FB})}{k_B T}\right) - 1}. \end{aligned} \tag{2.14}$$

The discussion has so far neglected the influence of any parameters that are specific to the device under consideration. For example, the capacitance of the gate insulator has not been included. It is however evident, that the efficiency by which the surface potential ϕ_s can be changed by the application of a voltage between the gate and the source V_{GS} will strongly depend on the geometry of the transistor as well as the materials used for the fabrication of the FET. This is why in Equation 2.14 $\phi_s = \alpha(V_{GS} - V_{FB})$ has been used, in which V_{GS} is the bias applied to the gate electrode, V_{FB}, the flatband voltage and α the gate coupling factor. V_{FB} and α are material and geometry-dependent parameters. V_{FB} accounts for a possible offset in the case that $\phi_s = 0$ does not coincide with $V_{GS} \neq 0$. Possible reasons for $V_{FB} \neq 0$ are fixed charges at the semiconductor/insulator interface (their density is denoted by N_{it}) that were not taken into account in the above considerations.
The gate coupling factor α describes the efficiency by which the gate-source voltage $\mathrm{V_{GS}}$ changes the surface potential ϕ_s. The gate coupling factor is given by [33]

$$\alpha = \frac{C_{ox}}{N_{it}e^2 + C_D + C_{ox}}, \tag{2.15}$$

with C_D as the capacitance of the charges in the channel per unit area and C_{ox} as the capacitance of the gate dielectric per unit area.

The drain current as given by Equation 2.14 depends not only on the material parameters, but also on three variables that can be controlled after the fabrication of the FET, namely the drain-source voltage V_{DS}, the gate-source

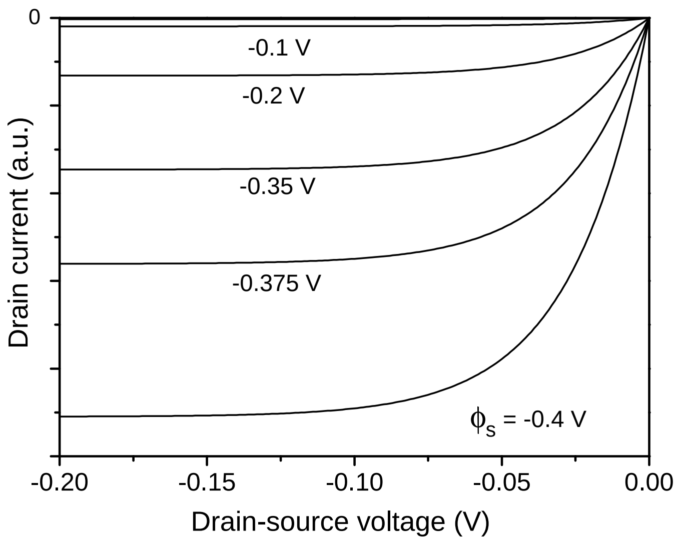

Figure 2.5: Evolution of the drain current I_D with drain-source voltage V_{DS} (output curve), as calculated with MATLAB after Equation 2.14, for different values of $\phi_s = \alpha(V_{GS} - V_{FB})$.

voltage V_{GS} and the temperature T. The impact of the independent variation of all three variables will now be discussed separately.

Variation of I_D with V_{DS}, (output curve)

The evolution of I_D with V_{DS} calculated from Equation 2.14 is displayed in Figure 2.5 for different constant values of the surface potential ϕ_s. The graph can be divided into two different regimes: At low drain-source voltages, the current increases linearly with the drain-source voltage (linear region of a transistor). At larger drain-source voltages the influence of the gate voltage is counteracted by the large drain bias close to the drain. This lowers the charge carrier density close to the drain contact, an effect called pinch-off which leads to a saturation of the drain current at large V_{DS} (called saturation region).

Variation of I_D with V_{GS}, (transfer curve)

From Equation 2.14 it is apparent that (for small values of V_{DS} this region is called subthreshold region) I_D increases exponentially with V_{GS}.
The inverse of the derivative of the logarithm of I_D with respect to V_{GS} is an important parameter for the characterization of FETs. It relates the properties of the materials used for the fabrication of the transistor to the applied gate voltage. This parameter is called subthreshold swing S and follows from the inverse of the differentiation of Equation 2.14 with respect to V_{GS} and describes the efficiency with which V_{GS} can change I_D. It is given by

$$S = \frac{dV_{GS}}{d(log(I_D))} = \frac{k_B T}{e} ln(10) \frac{1}{\alpha}. \tag{2.16}$$

The theoretical minimum of S is about 60 mV/decade at room temperature and corresponds to a maximum gate coupling efficiency of $\alpha = 1$. For transistor applications it is desirable that the subthreshold swing be as steep as possible, since then the gate voltage range needed for the operation of the transistor is minimal.
Strategies for minimizing S are *(1)* to increase C_{ox} (since $C_{ox} = \varepsilon_0 \varepsilon_r / d$ with d as the thickness of the gate insulator, this can be achieved by reducing the insulator thickness and/or increasing the dielectric constant ε_r of the insulator) and/or *(2)* reduce N_{it}. Both approaches will be discussed in chapter 3 for SWCNT FETs.
Evaluation of the subthreshold swing yields information about the density of these interface traps (here C_D was assumed to be negligible small) via

$$N_{it} = \left(\frac{log(2.72) e \cdot S}{k_B T} - 1 \right) \frac{C_{ox}}{e^2} \tag{2.17}$$

and thus about the quality of the semiconductor/insulator interface.

I_D for large V_{GS}

From Equation 2.14 it follows, that for large V_{GS} the drain current I_D rises without any limit if all other parameters are held constant. However, as for example shown in the transfer curve of a SWCNT FET in Figure 2.6, the exponential increase of I_D for low V_{GS} levels off into a square root dependence of I_D on V_{GS} at larger V_{GS}. One of the reasons is, that the efficiency α by which the gate-source voltage changes the surface potential, is a function of C_D. For the above considerations α was assumed to be independent of Q_s. However, at very large surface potentials this is not the case anymore.

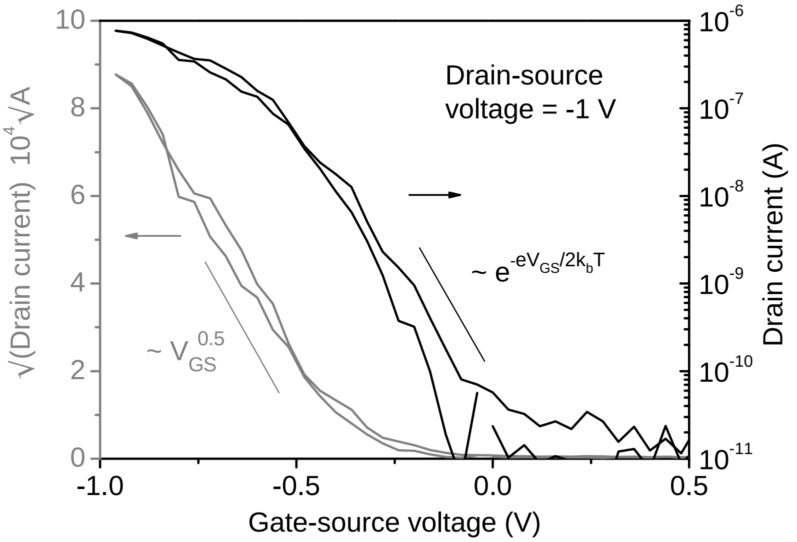

Figure 2.6: Experimental transfer curve of a SWCNT FET. At small gate voltages (V_{GS} between approximately 0 and -0.4 V) the drain current increases exponentially with V_{GS}, whereas at larger V_{GS} (between -0.5 and -1 V) a square root dependence of the drain current on V_{GS} is found.

The capacitance of the accumulation charge layer C_D then increases with increasing Q_s since the thickness of the accumulation layer, as determined by the screening or Debye length L_D, varies with Q_s like $L_D \propto \frac{1}{\sqrt{Q_s}}$. This in turn means that the gate coupling becomes smaller for increasing Q_s, as shown in Figure 2.7.

If for the calculation of I_D this decrease of the gate coupling α at larger Q_s is taken into account, the exponential increase of the space charge density with V_{GS} levels off for large Q_s (Figure 2.7).

For a simplified description of the basic behavior of the FET at large carrier concentrations, the space charge layer is usually assumed to be a charge sheet with zero thickness (L_D is assumed to be 0) which is the so called charge-sheet model[28, 34]. Assuming a charge sheet of thickness 0 implies that the potential drop across this layer is zero and the charge density at the surface is proportional to the applied voltage as well as the capacitance of the plate capacitor formed by the gate as the one electrode (C_{ox}) and the charge accumulated in the channel as the other electrode. The insulating layer is considered as the dielectric of this capacitor. It thus follows for the

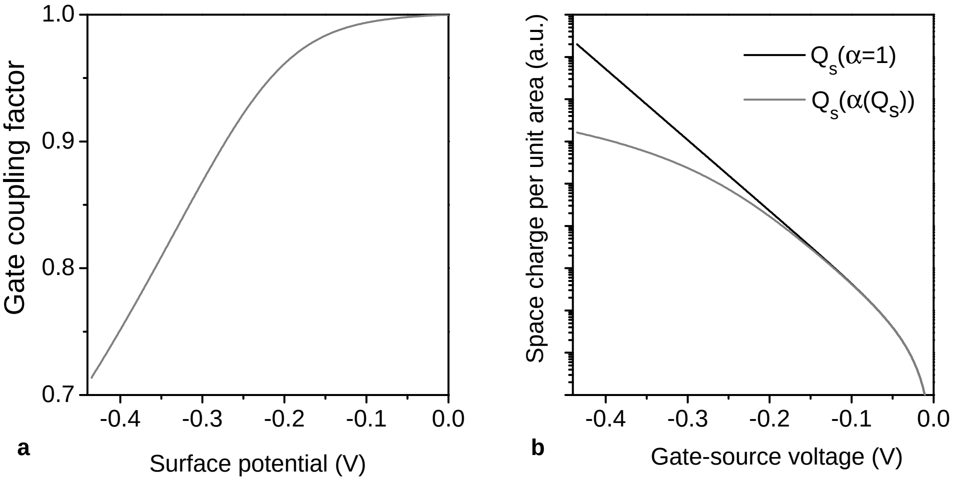

Figure 2.7: **(a)** The gate coupling factor α calculated with MATLAB as it varies with C_D. For this simple calculation it was assumed that $\alpha = 1/(1 + const \cdot C_D) = 1/(1 + const \cdot \sqrt{Q_s})$ **(b)** Calculated space charge per unit area for $\alpha(Q_s)$ and the comparison with $\alpha = 1$. For this calculation the gate-source voltage was increased in steps of ΔV_{GS}. The space charge density was then iteratively calculated according to $Q_s(V_{GS}, \alpha_i(Q_s(V_{GS} - \Delta V_{GS}, \alpha_{i-1})))$.

charge accumulated in the channel Q:

$$Q(y) = (V_{GS} - V_{FB} - \psi_{DS}(y))C_{ox} \tag{2.18}$$

Assuming a field-independent mobility μ it follows for the drain current from 2.11 after integration across the length of the channel

$$I_D = \mu C_{ox}\frac{Z}{L}(V_{GS} - V_{FB} - \frac{1}{2}V_{DS})V_{DS}. \tag{2.19}$$

This equation is only valid for gate voltages at which a significant charge density has already been induced in the channel (otherwise the assumption of a charge sheet is not justified). It describes $I_D(V_{DS})$ well until approximately the point $V_{DS}^{sat} = V_{GS} - V_{FB}$ at which the charge in the accumulation layer at the drain becomes zero, since at these values of V_{DS}, the influence of V_{GS} is compensated by V_{DS} (pinch-off). From this point on the drain current does not depend on V_{DS} anymore (Figure 2.5) and can be approximated by setting $V_{DS} = V_{GS} - V_{FB}$ in Equation 2.19

$$I_D = \mu C_{ox}\frac{Z}{L}(V_{GS} - V_{FB})^2. \tag{2.20}$$

In the saturation regime the mobility μ of the charge carriers can be extracted from the slope of the $\sqrt{I_D}$ vs. V_{GS} curve, which is given by

$$\mu = \frac{2L}{C_{ox}Z}\left(\frac{\sqrt{I_D}}{V_{GS}}\right)^2. \tag{2.21}$$

Another important parameter of a FET is the transconductance in the on state. It can be calculated from the transfer curve by

$$g_m = \frac{dI_D}{dV_{GS}}. \tag{2.22}$$

2.2.4 Drain current in the off state (region 2)

In this regime (region 2 marked in Figure 2.4) the charge in the channel is dominated by holes. Due to the low density of charge carriers the current that flows through the device is negligible (off state). The space charge density is proportional to $\sqrt{\phi_s}$ (Figure 2.4). This renders Q_s to (here, p is expressed by Equation 2.3)

$$Q_s = \mp\sqrt{2\varepsilon_0\varepsilon_r k_B T}\sqrt{\frac{N_V n_a}{n_D}e^{-\frac{E_a}{k_B T}}\frac{e\phi_s}{k_B T}}. \tag{2.23}$$

With Equation 2.11 it follows for I_D

$$I_D = \mu\frac{Z}{L}\sqrt{\frac{2\varepsilon_0\varepsilon_r e}{k_B T}}\sqrt{\frac{N_V n_A}{N_D}}e^{-\frac{E_a}{2k_B T}}\sqrt{\alpha(V_{GS}-V_{FB})}V_{DS}. \tag{2.24}$$

The drain current I_D depends linearly on both $\sqrt{V_{GS}}$ and V_{DS}. This means that I_D, in contrast to the exponential influence of V_{GS} in region 1, is only weakly influenced by V_{GS}, but strongly depends on the intrinsic carrier densities that are given by the doping density. In chapter 4, I_D of a SWCNT FET will be strongly altered by doping with Prussian Blue. The impact of the doping concentration on the space charge per unit area will be discussed in section 2.2.6 in more detail.

2.2.5 Drain current in the strong inversion regime (region 3)

In the inversion regime the drain current can be calculated in a manner analogous to the accumulation regime. From Equation 2.7 it can be seen that in this region the space charge density and accordingly the drain current increases exponentially with the surface potential. This is the region single-crystalline silicon MOSFETs typically operate in. Since the FETs investigated in this work all operate in the accumulation regime, the strong inversion regime will not be further discussed.

2.2.6 Impact of the channel doping concentration on the space charge

The introduction of electron or hole-donating species into a semiconductor is called doping. The carrier concentration in the channel can be adjusted by systematic doping. From Equation 2.7 the effect of different doping concentrations on the space charge density can be calculated. The result is shown in Figure 2.8, where it can be discerned that the impact of the doping on Q_s is twofold. Firstly, a lower surface potential is needed in order to induce the same space charge density (marked by 1 in Figure 2.8). Second, an increased p-doping leads to an increase of the space charge density in the off region. This in turn will lead to an increased minimum conductivity of the channel (marked by 2).

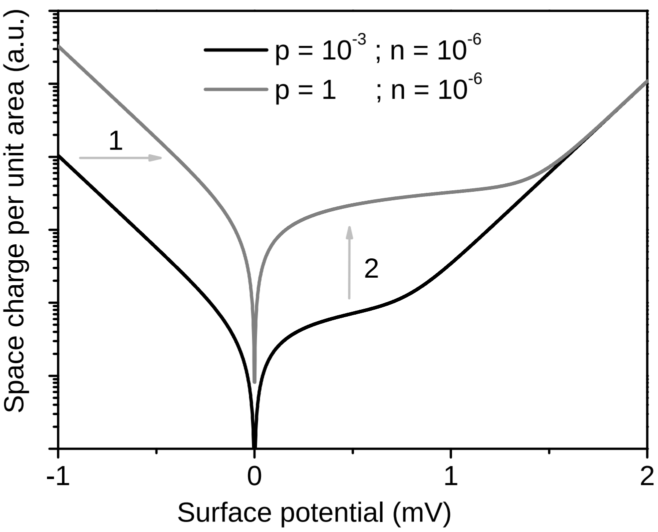

Figure 2.8: Variation of space charge density in a MIS-structure for different ratios of p/n calculated with MATLAB from Equation 2.7.

At very large doping levels, the on-off ratio is drastically decreased and I_D

in the on state and the off state are approximately the same. This case is encountered for the Prussian Blue-doped SWCNTs described in chapter 4.

2.2.7 Determination of the dopant activation energy from the temperature dependence of I_D

The activation energy of the dopants E_a has has a direct influence on the charge carrier density in the channel. From the evolution of the subthreshold current with temperature the activation energy of the dopants can be measured. In order to get a first hint how different activation energies E_a influence the temperature dependence of the drain current, Equation 2.14 can be evaluated for different E_a. Equation 2.2 adequately describes the temperature dependence only for low temperatures or values of V_{GS} for which the Fermi level is far away from the valence band.[32] It follows that the current

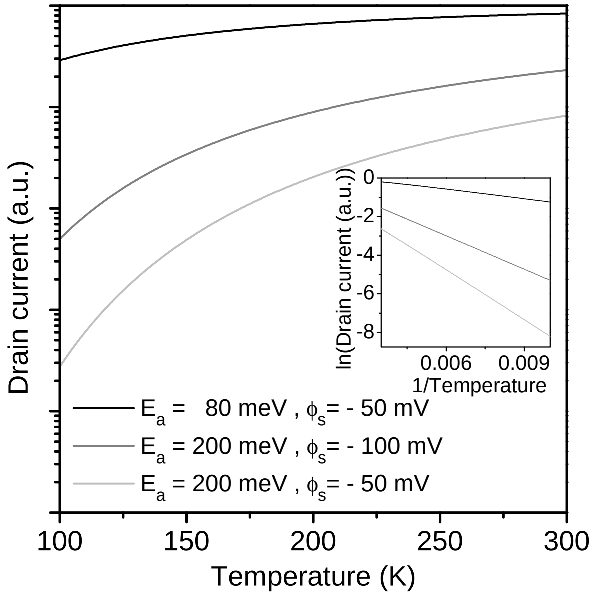

Figure 2.9: Calculated $I_D(T)$ for different E_a and V_{GS} from 2.14

.

varies exponentially with $\frac{1}{T}$, which results in the linear behavior in the $ln(I_D)$ versus $1/T$ plot shown in the inset of Figure 2.9. This behavior is the typical

Arrhenius-law for thermally activated processes.
For an activation energy of $\mathrm{E_a} = 80$ meV, hardly any variation of the drain current between 100 K and 300 K can be discerned. In contrast, if an activation energy of $\mathrm{E_a} = 200$ mV is assumed, a strong temperature dependence of the drain current occurs. While in the investigated temperature range an activation energy of 80 meV only leads to a variation of the drain current by a factor of 5, an activation energy of 200 meV results in a decrease of the drain current by more than one order of magnitude.
It is furthermore important to note that the gate-source voltage $\mathrm{V_{GS}}$ has to be included in the determination of the activation energy. For different values of V_{GS}, I_D evolves differently with temperature (Figure 2.9). This is due to the fact that an increased gate voltage shifts the Fermi level closer to the dopants which allows for their ionization already at lower temperatures. If the impact of $\mathrm{V_{DS}}$ is neglected (which can be done for the small $\mathrm{V_{DS}}$ usually used in the experiments), Equation 2.14 can be simplified. The one-dimensional effective density of states $N_V^{1D} = \sqrt{\frac{m^* k_B T}{2\pi\hbar^2}}$ was used in this case, since in this thesis the doping of a one-dimensional system (SWCNTs) is investigated. It follows for the drain current

$$I_D = \mu \frac{Z}{L} \sqrt{2\varepsilon_0 \varepsilon_r k_B T \sqrt{\frac{m^* k_B T}{\pi\hbar^2}} \frac{n_A}{n_D} e^{-\frac{E_a}{k_B T}} \frac{2 k_B T}{e}} \sqrt{e^{-\frac{e\alpha(V_{GS}-V_{FB})}{k_B T}}}. \tag{2.25}$$

Thus the relationship between I_D and T is given by

$$I_D \propto e^{-\frac{E_a + e\alpha(V_{GS}-V_{FB})}{2k_B T}}, \tag{2.26}$$

where the weak non-exponential influence of the temperature has been neglected in favor of the much stronger exponential factor. In chapter 4, this relation will be used to estimate the activation energy E_a of the Prussian Blue dopants in SWCNTs.

2.3 Applicability of the derived formula to SWCNT-FETs

Due to the one-dimensional nature of SWCNTs, certain modifications of the above equations are required, as explained in the following.

Concept of mobility in a ballistic conductor

The SWCNT FETs fabricated in this thesis all have a channel length below 200 nm. In SWCNTs, transport is ballistic at room temperature across these distances [35]. The concept of mobility, however, is based on scattering of charge carriers ($\mu = e\tau/m^*$ with τ relaxation time between two scattering events and m^* the effective mass of the charge carriers). Since scattering does not occur in ballistic conductors, the concept of mobility is not valid and carrier mobilities for SWCNT FETs are therefore not given.

Role of Schottky barriers at the SWCNT/metal contact in FET operation

At the contact between a metal and a semiconductor, charges are transferred from the material with the lower work function to that with the larger work function. This leads to a bending of the bands in the semiconductor at the contact (called Schottky barrier formation[28]). The applied gate voltage leads to a modulation of the width of the Schottky barriers. This gate dependent modulation of the Schottky barriers leads to an additional modification of the drain current on top of the modulation of the drain current by the change of the charge carrier density with gate-source voltage.[36]. However, as the overall transistor behavior still is dominated by the modulation of the charge carrier density within the channel, the role of Schottky barriers in the FET operation will be neglected in the following.

One-dimensional channel

Electrical transport trough a one-dimensional channel is described by the Landauer formula. It accounts for the mismatch of current-carrying channels in the contacts (3D objects) and the one-dimensional channel. This mismatch leads to a finite contact resistance for each current-carrying channel within the one-dimensional object (the quantum of conductance $G_0 = e^2/h = (25.8\,\mathrm{k}\Omega)^{-1}$). Such a description for SWCNT FETs has been done, for example, in [37]. It leads to output and transfer characteristics that are qualitatively similar to those obtained from the classical formula derived in this chapter. This is why for a qualitative description of SWCNT FETs the above-derived formula are used that neglect the influence of an one-dimensional channel. However, the above-derived formula do not yield the correct maximum conductance, given by $4G_0$ in a FET based on an individual SWCNT.

Another implication of the presence of a one-dimensional channel is, that the typical bending of the bands at the semiconductor/semiconductor interface

(Figure 2.3) on which the deviation of the drain current I_D was based, is not necessarily valid. This in turn means, that the derived formula for the activation energy E_a is only a rough approximation when applied to systems such as the doped SWCNTs.

2.4 Applicability of the derived formula to organic FETs

The above description of the FETs was based on the assumption that the semiconductor possesses continuous bands with no localized states. However, in FETs based on small molecules, especially for FETs based on vacuum deposited layers as they are used in part of this work, this assumption is not vaild. These films are usually polycrystalline and therefore contain a large density of defects, in particular grain boundaries that disrupt the periodicity of the crystal lattice and give rise to localized states in the band gap.

Dependence of the mobility on the electric field

In Equation 2.12 it was assumed that the mobility μ of the charge carriers is independent of the gate and source/drain field. This is not the case if the semiconductor has localized states in the band gap (Figure 2.10), as is the case for most FETs comprising small molecules. Here, the mobility depends on the position of the Fermi level (as determined by the gate voltage) relative to the energy of the traps. Nontheless, in most publications the mobility is assumed to be independent of the applied biases. This simplification will also be used here.

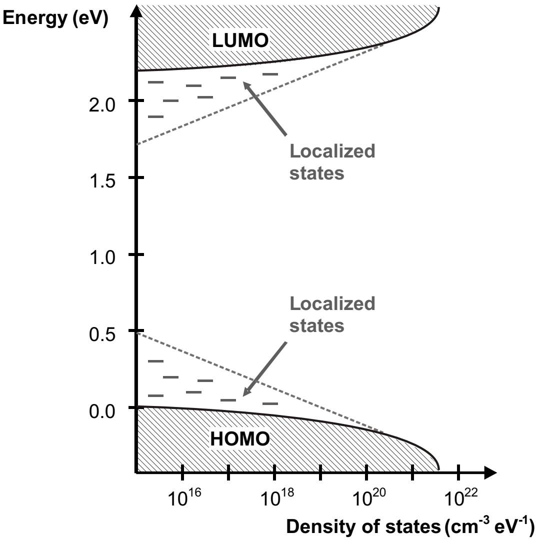

Figure 2.10: Schematic depiction of the electronic density of states of an organic semiconductor. The band-like states are shown in black. The localized states are shown in grey [**?**].

.

Chapter 3

SWCNT transistors on SAM-based gate dielectric

Single-walled carbon nanotubes (SWCNTs) are promising components of field effect transistors (FETs). However, as demonstrated in chapter 2, not only the material used for the channel but also other parameters determine the performance of an FET. For example, the subthreshold swing S is determined by the thickness and dielectric constant of the materials used for the gate dielectric and the defect density at the SWCNT/gate dielectric interface. In the most widely used configuration, a highly doped silicon substrate covered with thermally grown SiO_2 (typical thickness $100 - 200$ nm; growth temperature $> 700°C$) serves as a macroscopic back-gate.[38] In order to achieve increased capacitive coupling that reduces the operating voltage of the FET, alternative gate dielectrics of ultra-thin thickness (e.g., Al_2O_3)[39] or high dielectric permittivity (e.g., ZrO_2)[40, 41] have been investigated, in some cases employing a top-gate geometry. While the corresponding FETs exhibit a very high transconductance, they often suffer from pronounced hysteresis in the transfer characteristic [42], which is a sign of a large interface state density. Back gated FETs based on random SWCNT networks have recently been reported using a thin (16 nm) organic self assembled multilayer gate dielectric.[43, 44] Devices reported in that work show a greatly reduced hysteresis, but - since they are based on SWCNT networks - show inferior on/off drain current ratio and mobility. In addition, they display relatively large gate leakage currents.

In this chapter the possibility of using self-assembled monolayers (SAMs) as major insulating component of the gate dielectric will be investigated. The use of a SAM promises to reduce the thickness of the gate dielectric and therefore reduce the operation voltage of the FETs. Furthermore, it

was shown that the SAM dielectric has a low defect density [45] and thus promises a reduced subthreshold swing.
Two different molecules will be utilized for the fabrication of high-quality SAMs. The first one is a silane that self-assembles on SiO_2. SWCNT FETs in a global back-gate-geometry [46, 47] (i.e. only one gate electrode is available for all FETs that are located on the same substrate) will be fabricated in this manner. Based on these devices, the impact that the use of a SAM has on the FET performance will be assessed. For the fabrication of logic circuits however, the use of a global back gate structure is not suitable. Accordingly, a phosphonic-acid based molecule will be used in the second part of this chapter to fabricate FETs with a local back gate. Phosphonic acid-based molecules readily form high-quality SAMs on metal oxides [15], which allows for the fabrication of patterned aluminum gate electrodes. This approach will also be used to investigate the operational and shelf-life stability of SWCNT FETs.

3.1 SWCNT FETs based on global SAM dielectric

3.1.1 Fabrication and characterization of SAM-based dielectric

For the implementation of FETs in a global back gate geometry, heavily doped Si-wafers were used as substrate and gate electrode. The structure of the SWCNT-FET devices is apparent from Figure 3.1b. The SAM is based on (18-phenoxyoctadecyl)-trichlorosilane and self-assembles subsequent to a brief oxygen plasma treatment (0.1 mbar, 100 W, 10 sec, substrate at room temperature) of a p+-doped silicon wafer from the vapor phase (low-pressure nitrogen atmosphere) at a temperature of 200 °C. Ellipsometry revealed that the plasma activation resulted in a ~ 4 nm thick SiO_2 coating of the silicon substrate. The plasma activation is required for high-quality molecular self-assembly in order to generate a sufficient density of functional groups at the surface. During the plasma treatment, the substrate remains at room temperature, which in principle opens up the possibility of implementing the devices on flexible substrates (in which case a metal would be used instead of silicon). Compared to silicon dioxide formed by thermal oxidation above 700 °C [48], the room temperature plasma-grown SiO_2 is of lower quality,

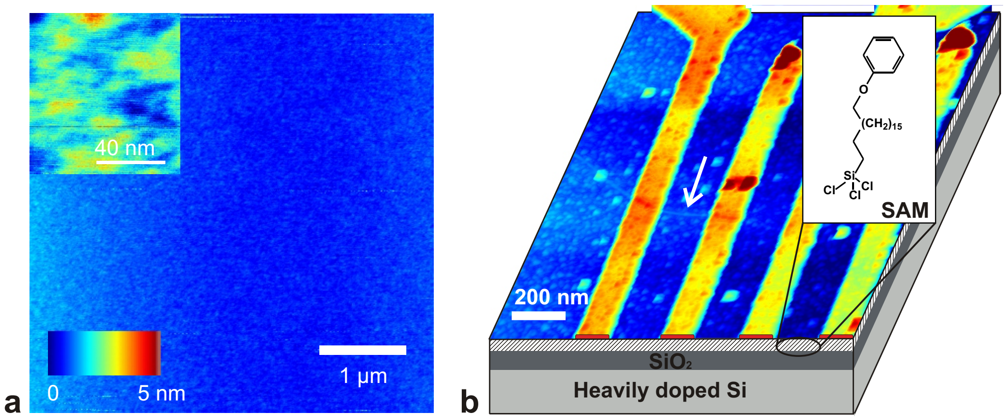

Figure 3.1: **(a)** Tapping-mode atomic force microscopy (AFM) image of the silicon substrate covered by the SAM. The layer is very smooth and pinhole free across large areas. **Inset** Zoom into the main image. The color scale ranges from 0 to 0.5 nm.**(b)**AFM image of a typical SWCNT-FET device structure. The 4 nm thick SiO_2 layer on top of the highly doped silicon wafer (light gray) is shown in dark gray. Four AuPd electrode lines are deposited onto the SAM (hatched layer) that has formed on the SiO_2 surface. A 0.3 nm thick layer of titanium is evaporated on top of the monolayer to enable spin coating of 2.5% PMMA solution. The individual SWCNT in the AFM image has been colored to enhance its visibility. The scale bar is 200 nm. **Inset:** Chemical structure of the silane molecule used for SAM formation.

but as far as gate leakage and interface state density are concerned, this deficiency is compensated by the SAM which is also created at low temperature (200 °C).

The SAM-covered substrate is smooth over large areas as shown by atomic force microscopy (Figure 3.1a). Scanning tunneling microscopy studies have shown that the SAM is essentially free of pinholes [45]. The capacitance of the dielectric stack, in which the SAM accounts for the majority of the insulating properties, has been determined by impedance spectroscopy to be 0.5 $\mu F/cm^2$. The relative permittivity of the dielectric is estimated to be about 3.3 and is predominantly determined by the permittivities of the SAM and the SiO_2. Due to the strongly hydrophobic character of the SAM-modified surface, a 0.3 nm thick layer of titanium had to be evaporated onto the samples to allow spin coating of the e-beam resist (PMMA, see Appendix A for details on the e-beam lithography procedure). The titanium does not form a closed layer, as confirmed by AFM measurements. Due to the small thickness and fast oxidation of the titanium layer upon air exposure, it does

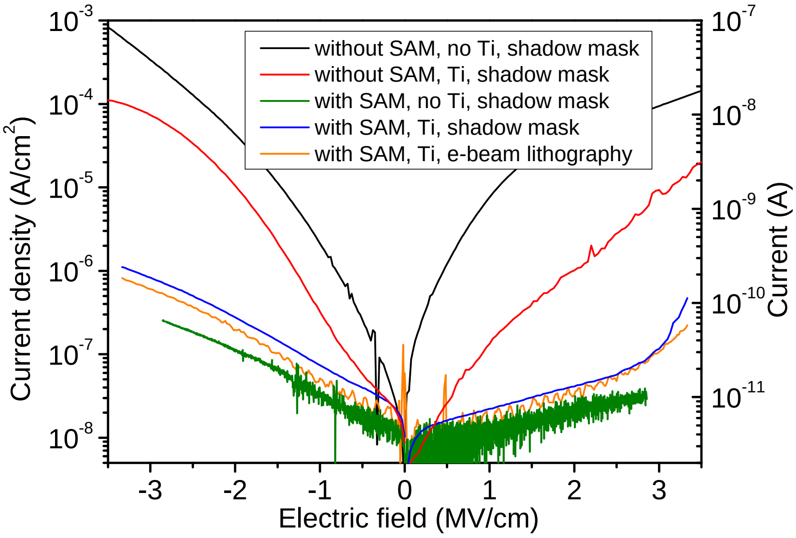

Figure 3.2: Current density through the gate dielectric vs. bias field measured at room temperature on sandwich structures with and without the organic SAM. In the devices incorporating the SAM, the top gold contacts were patterned either by e-beam lithography or by evaporation through a shadow mask. The absolute current is displayed on the right axis.

not contribute to the electrical conduction between source and drain, as has been confirmed by electrical measurement. The contribution of the capacitance of the oxidized titanium to the total capacitance of the dielectric stack can be neglected, since titanium oxide has a very large permittivity (> 50) in comparison to the SiO_2/SAM stack (addition of the titanium oxide reduces the total capacitance by about 1%).

Process and electrical stability of the SAM

In order to determine the extent to which the e-beam exposure during lithography causes structural damage of the SAM as well as to evaluate the contribution of the SAM to the insulating properties of the SiO_2/SAM-dielectric, five different types of test structures were investigated. These samples consist of a heavily doped silicon substrate covered by a thin dielectric (bare or SAM-modified 4 nm plasma-grown SiO_2, with or without 0.3 nm oxidized Ti) and a top metal contact (patterned either through an evaporation mask or by e-beam lithography). Thin metal wires were carefully glue-bonded to the contact pads to establish reliable electrical connections between the device terminals and the chip carrier. In Figure 3.2, the results of current-voltage (I-V) measurements performed on the respective samples under ambient conditions are shown. The SiO_2 dielectric without SAM has very poor insulating properties, as apparent from the substantial current density of about 10^{-4} A/cm^2 at an electric field of 2 MV/cm applied between the silicon gate and the metal contact. The leakage current does not decrease significantly upon evaporating 0.3 nm of Ti onto the 4 nm thick plasma grown SiO_2 and allowing the Ti to oxidize prior to depositing the contact pads. The large leakage currents in the devices without SAM originate from the poor quality of plasma-grown SiO_2 as compared to high-quality SiO_2 grown by thermal oxidation.[48]

In comparison, the test structures including a SAM exhibit a significantly reduced leakage current density of less than 10^{-7} A/cm^2 at the same electric field. This confirms the crucial role of the SAM in determining the insulating properties of the dielectric stack, despite its thickness of only 2 nm. A similar conclusion has previously been drawn for organic SAM-containing sandwich devices.[45, 49, 50] Comparing the SAM devices with and without a 0.3 nm thick Ti layer evaporated on top of the SAM shows an increase in leakage current by a factor of about 2 as a result of the titanium deposition. If the SAM was significantly damaged or destroyed by the Ti, as has been reported in the literature [51], one would expect a more significant increase in leakage current. In the present case, however, it is believed that the 0.3 nm Ti oxidizes sufficiently fast (due to its very small thickness and the residual gas in our evaporator) to not inflict substantial damage on the SAM.

More intriguingly, the leakage current through the SAM dielectric is found to be virtually the same (10^{-7} A/cm^2 at 2 MV/cm) regardless of whether the top metal contact is patterned by a shadow-mask technique or by e-beam lithography, which demonstrates that the electron dose of 300 μC/cm^2 does not significantly damage the SAM. Due to its small thickness, the electron absorption in the oxidized Ti can be ignored, especially since AFM measurements suggested that the oxidized Ti does not form a closed layer. At first glance, the good stability of the SAM under e-beam exposure appears to be in contrast to literature reports of considerable damage involving bond rapture and partial desorption of molecular fragments after e-beam irradiation of thiol-based SAMs on Au substrates.[52] However, it has to be taken into account that the electron energy of 25 keV in the present study is much higher than the $10 - 100$ eV used in case of the thiol-based monolayers. It is well-documented that higher energy electron irradiation causes less dam-

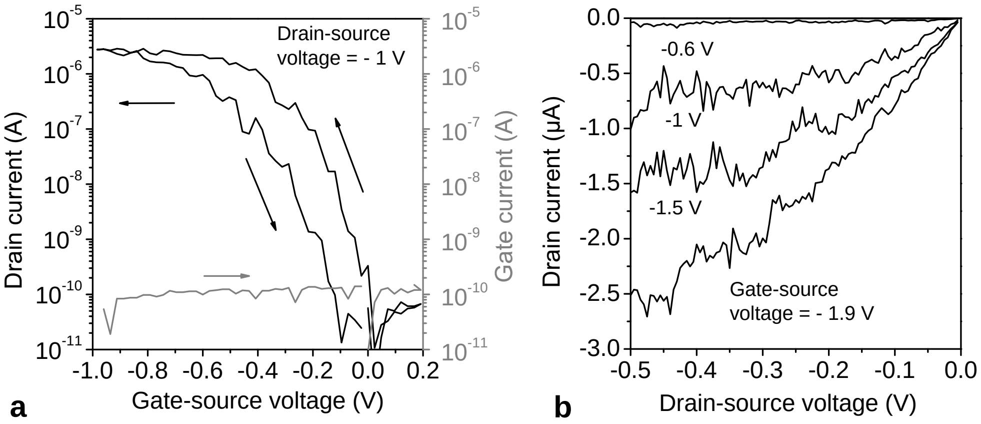

Figure 3.3: **(a)** Transfer characteristics of the same device as in Figure 3.1. The gate voltage sweep rate was 150 mV/s. All measurements were performed under ambient conditions. The measured gate leakage current resolution is limited by the measurement setup in this experiment. Data for the leakage current density are available from Figure 3.2 which shows measurements of the gate leakage current with a higher accuracy. **(b)** Output characteristics of a FET device with a SAM-based gate dielectric comprising an individual semiconducting SWCNT as channel.

age in thin organic films than lower energy irradiation.[53] This difference can be attributed to the lower stopping power of higher energy electrons, whereby only little energy is deposited in thin films. First signs of electron-beam induced damage of the PMMA resist-covered SAMs, manifested by increased leakage currents ($\geq 10^{-6}$ A/cm^2), were detected for doses larger than 1800 µC/cm^2.

3.1.2 Electrical characteristics of the FETs

Building upon the excellent process stability and insulating properties of the SAM-based dielectric, FETs from individual semiconducting SWCNTs were fabricated. SWCNTs were solution-deposited and source and drain contacts defined by e-beam lithography and thermal metal deposition, as described in Appendix A. The output characteristics of an exemplary device (tube diameter 1.2 nm) shown in Figure 3.3a display p-type behavior, a common feature of SWCNT-FETs that were not subjected to further treatment.[39, 54] The drain current vs. drain-source voltage characteristic resembles that of conventional p-type metal-oxide-semiconductor FETs (MOSFETs). One of these features is the saturation of the drain current at higher V_{DS} (Figure 2.5).[28] For the present device, saturation occurs at a drain-source voltage of approximately −0.3 V and a gate-source voltage of 1.5 V (also see Figure 3.5 for a different device showing good saturation). From the transfer characteristics, shown in Figure 3.3b, one finds a transconductance [28] $g_m = dI_D/dV_{GS}$ of about 20 μS at $V_{\mathrm{DS}} = 1$ V. This value is close to the highest so far reported for SWCNT-FETs [55] and testifies to the superior gate coupling. The device exhibits a threshold voltage between 0.05 and 0.5 V, depending on whether the threshold voltage is estimated from the plot of the square-root of the drain current versus gate source voltage, or from the plot of the drain current versus drain source voltage. Moreover, the large on/off drain current ratio of about 10^5 (at $V_{\mathrm{DS}} = 1$ V) is remarkable in view of the small thickness of the gate dielectric and theoretical predictions on drain voltage scaling in SWCNT-FETs.[41, 56, 57, 58]

Investigation of subthreshold behavior and the interface state density

Evaluation of the subthreshold swing S (see Equation 2.16) yields the value of 60 mV/decade, close to the theoretical limit of the subthreshold swing at room temperature [28]. Such a low value has not been previously reported for undoped Schottky-barrier SWCNT FETs with low operating voltages[40, 59, 60, 61, 62], and its realization within the present devices is notable considering that no attempts were made to reduce the contact resistance [63], and that a global back gate structure is used. Previous publications have reported subthreshold swings of 60 to 70 mV/decade for SWCNT FETs in which the channel conductance was controlled with a local gate while the contact regions were either chemically doped [63] or electrostatically "doped" by applying a large static field from a global back gate [40, 62]. It is known, that in such devices the subthreshold slope is not limited by the gate dielectric [62, 64]. In the present devices, the low voltage back gate controls the entire nanotube and the low subthreshold swing is an indication for the high quality of the gate dielectric used in this work.

From the subthreshold swing the interface state density N (defined in Equation 2.17) of the SAM/SWCNT interface can be estimated. The obtained value of $N = 6 \times 10^{-10}$ $\mathrm{cm}^{-2}/\mathrm{V}^{-1}$ is more than one order of magnitude lower compared to other SWCNT transistors [41, 54, 55, 57] (see Figure 3.4), which underlines the high structural quality of the SAM.

It should be stressed, that in order to achieve a minimal subthreshold swing both the capacitance of the gate dielectric as well as the interface state density have to be optimized. While in most works using high-permittivity

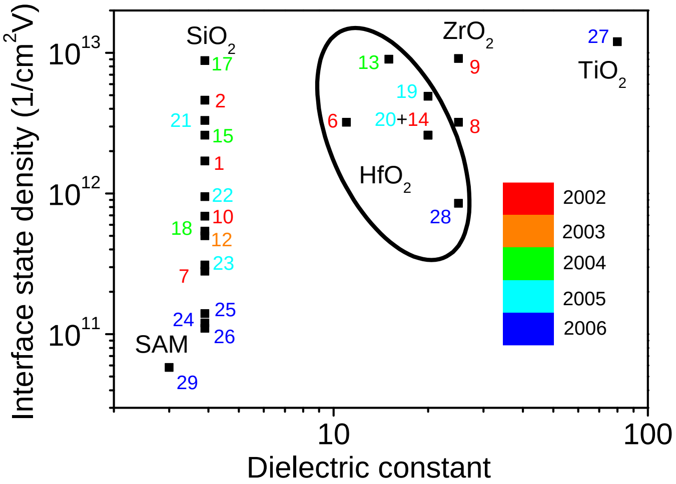

Figure 3.4: Comparison of the interface state density of gate insulator materials with different dielectric constants. The color scale indicates the respective year of the publication. It can be clearly observed that for materials of lower dielectric constant the interface state density is lower. Furthermore, a trend towards a lower interface state density over the years due to higher quality dielectrics is visible. **1.-3.** [65] **4.-5.** [66] **6.-7.** [54] **8.-10.** [41] **11.** [42]**12.** [56] **13.** [55] **14.-15.** [67] **16.** [35] **17.** [68]**18.** [69] **19.-20.** [59] **21.** [70] **22.-23.** [63] **24.-25.** [71] **26.-27.** [57]**28.** [40] **29.** [46]

dielectrics a large capacitive coupling is realized, the interface trap density is often high in comparison to dielectrics with lower permittivity like the one used in this work (see Figure 3.4).

It is furthermore relevant that the device exhibits a very low gate leakage current ($\sim$ 100 pA at $V_{GS} = 1$ V) that is smaller than the drain current by more than four orders of magnitude. This leakage current is an upper limit of the actual leakage, since the minimum resolution of the instrument used in this measurement is about 100 pA. Figure 3.2 provides the real leakage current through the gate dielectric. While the electrical characteristics presented above belong to one of the best devices, it is noted that only a relatively small variation in performance was observed from sample-to-sample. In particular, all of the devices displayed saturation of the drain current in the output characteristic. The lowest transconductance and on/off ratio found among the investigated devices was 0.5 µS and 10^4, respectively, while subthreshold swings as large as 300 mV per decade were measured.

Hysteresis in the drain current

The transfer characteristics of the investigated devices (Figure 3.3) disclose a hysteresis, a phenomenon is common to SWCNT-FETs. It has been ascribed to traps located within the bulk SiO_2 gate insulator or near the nanotube/SiO_2 interface, which get filled with electrons from the nanotube channel upon sweeping to more positive gate voltages.[58, 72] Similar to other SWCNT-FETs, the present devices show forward-type hysteresis.[42] Its magnitude (defined as the separation between the forward and backward curves at 50% of the maximum source-drain current) depends on temperature as well as the V_{GS} sweep rate and range, whereas it is only weakly affected by V_{DS}. We find a room temperature hysteresis of 900 mV when sweeping the gate voltage between 1.5 and -1.5 V at a rate of 7.5 mV/s. Its value decreases down to 100 mV/s upon increasing the sweep rate to 350 mV/s. Such a decrease in hysteresis with rising sweep rate of the gate voltage indicates the presence of trap charging on a time scale on the order of several hundreds of milliseconds. Moreover, the hysteresis experiences a significant reduction when the devices are cooled, similar to the behavior of SWCNT-FETs with a pure SiO_2 gate insulator [72, 73].

Hysteresis in SWCNT-FETs has previously been considered mostly from the viewpoint of potential memory applications.[72, 73, 74] This task still requires a better control over the hysteretic effect, although first promising steps have already been taken in this direction, for instance via removal of the water layer from the SiO_2 gate insulator surface.[42] A prerequisite for efficient operation as a FET, however, is the absence of hysteresis. In this regard, it is pertinent to note that some of the investigated devices exhibited essentially no hysteresis even when measured under ambient conditions, i.e., with the SWCNT channel exposed to air (Figure 3.5). This result is outstanding since a vanishing hysteresis has so far only been achieved with the nanotube protected from air by either inorganic atomic-layer deposited (ALD) dielectrics [57] or when working with a liquid gate [61]. The small or absent hysteresis in the SWCNT-FETs investigated here can be attributed to two major factors. A first contribution may arise from the low operation voltage enabled by the strong gate coupling, as has been put forward previously.[43] Secondly, the SAM-modified dielectric surface should adsorb only little amounts of water, despite the thin oxidized titanium layer covering the SAM.[45] This is further supported by the finding that the hysteresis of the devices is not significantly reduced upon transfer of the device into vacuum. Since water is known to enhance hysteretic behavior[42], the predominantly hydrophobic character of

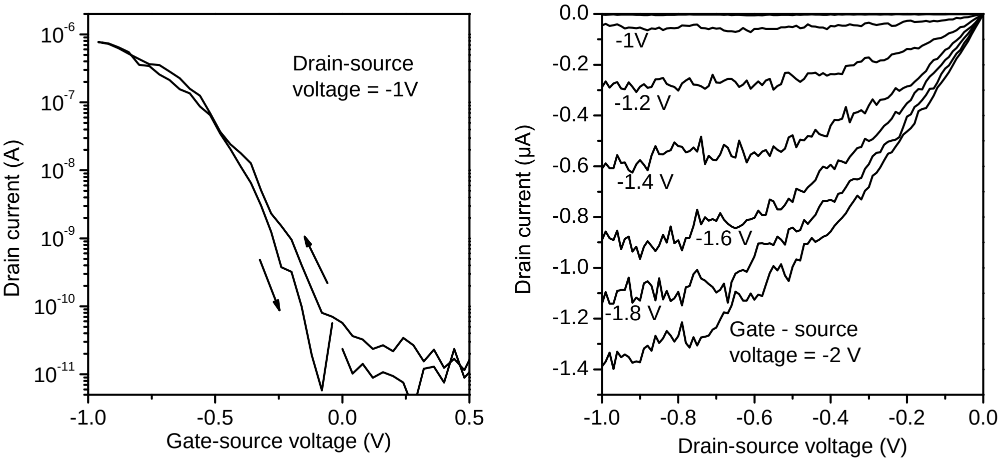

Figure 3.5: Transfer **(left)** and output **(right)** curves of a SWCNT FET at a drain-source voltage of -1 V. Negligible hysteresis is measured under ambient conditions. The gate voltage sweep rate was 210 mV/s.

the surface should help to reduce the hysteresis.

To prove that indeed the monolayer is responsible for the reduced hysteresis, we fabricated devices with a 100 nm thick thermal SiO_2 gate dielectric covered by the SAM and 0.3 nm of Ti. We found the hysteresis to be between 0 and about 20% of the maximum gate voltage window. In Figure 3.6, such a transfer curve is compared with a device that does not have a SAM covering the thermal SiO_2. In the device with the SAM the hysteresis is significantly reduced. To evaluate the extent to which the SAM reduces the hysteresis data from the transistors investigated here are compared to data taken from the work by Kim et al.[42] Since the hysteresis is known to depend on the gate voltage sweep rate and the maximum applied gate field, not the absolute value of the hysteresis can be compared but it has to be set in relation to the maximum gate field and the sweep rate. When in the FET comprising the SAM-covered SiO_2 the gate field is swept at a speed of 3.8×10^4 V/cms across a gate field of 1×10^6 V/cm a hysteresis of 12% of the maximum gate field window (i.e. the difference between the maximum and minimum gate field) can be observed. In Kim et al.'s work a thermally grown SiO_2 is used without any surface functionalization [42]. The gate field is for example swept at a speed of 1.1×10^5 V/cm $\cdot$ s up to a maximum field of 2×10^5 V/cms. A hysteresis of 38% of the maximum gate field window can be observed. In comparison with the present results it can be seen that

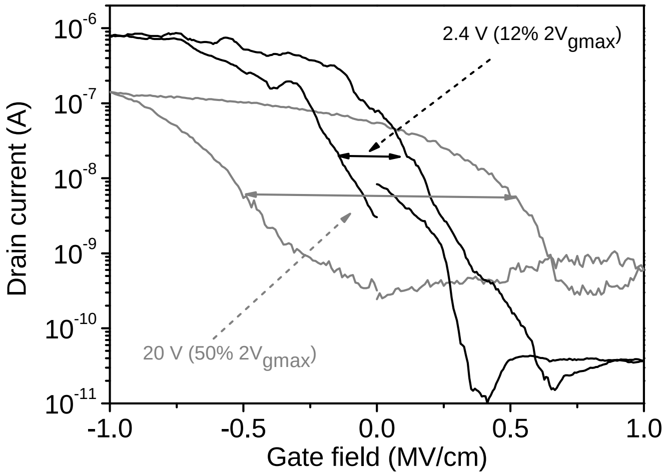

Figure 3.6: Transfer curve of two devices: In light grey a SWCNT FET with a 200 nm SiO_2 dielectric, in black a SWCNT FET with a 100 nm SiO_2 and a SAM on top. The hysteresis in this case is only 12% of the gate voltage window (determined by the difference between the minimum and maximum gate voltage) at a gate voltage sweep rate of 0.38 V/s (3.8×10^4 V/cms).

even when a device with SAM is swept across a larger gate electric field at a low sweep speed the hysteresis in the drain current is still lower than in devices that do not include the SAM.

3.2 SWCNTs FETs with local gates and SAM-based gate dielectric

The silane-based SAM used in chapter 3.1 allowed for the fabrication of high-performance FETs based on a global back-gate. However, the use of a global back-gate has certain limitations. For example, since the overlap between the source/drain and the gate electrode is large (source/drain pads overlap with the gate), the operational frequency of the transistor is limited. Furthermore, the use of one gate electrode per substrate does not allow for the fabrication of simple logic circuits.

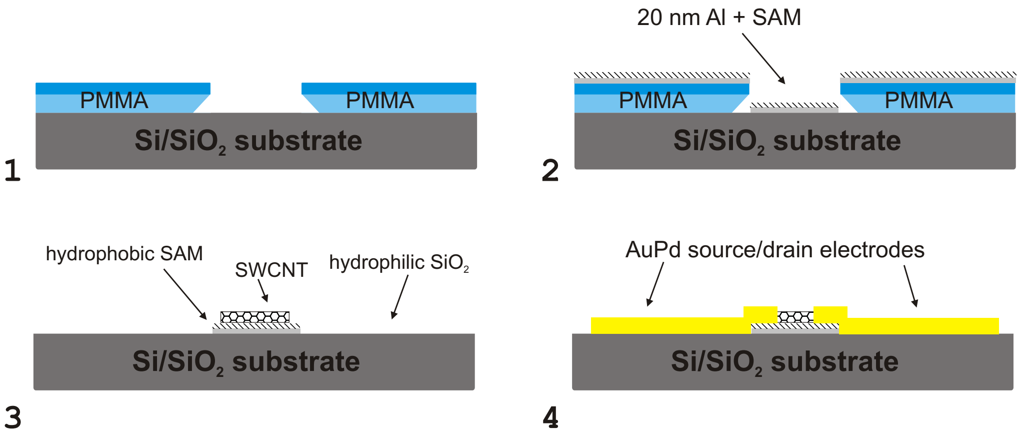

Figure 3.7: Fabrication process for carbon nanotube FETs with individual metal gate electrodes: **(1)** A thermally oxidized silicon wafer is coated with a double layer of PMMA resist, and areas for the gate electrodes are opened by e- beam lithography. **(2)** A 20 nm thick layer of aluminum is deposited by vacuum evaporation and briefly exposed to an oxygen plasma. An organic monolayer is allowed to self assemble on the plasma-oxidized aluminum from a solution of n-octadecylphosphonic acid. **(3)** The PMMA resist is stripped off and the substrate is immersed in a suspension of HiPCO SWCNTs. **(4)** Gold/palladium source/drain contacts are created by e beam lithography, evaporation and lift off.

In this section, the fabrication of FETs based on individual semiconducting SWCNTs with patterned aluminum gate electrodes and a thin room-temperature gate dielectric consisting of oxygen plasma-grown aluminum oxide and an organic self-assembled monolayer are investigated. The devices were manufactured on a thermally oxidized silicon wafer. The wafer serves only as a substrate and is not part of the final device. It is coated with poly(methyl-metacrylate) (PMMA) resist, and areas for the local gate electrodes are opened in the resist by e-beam lithography (see Figure 3.7 and Appendix A). A 20 nm thick layer of aluminum is deposited by thermal evaporation and then briefly exposed to an oxygen plasma. This creates a 3.8 nm thick layer of aluminum oxide terminated with hydroxyl groups [15]. The substrate is then immersed in a 2-propanol solution containing 5 mM of n-octadecylphosphonic acid, so that a 2.1 nm thick SAM is formed on the plasma oxidized aluminum gate electrodes [15]. The result is a gate dielectric with a thickness of about 6 nm composed of plasma-grown aluminum oxide and a high-quality SAM, both created at room temperature (see Figure 3.7). Since the areas outside the aluminum gates are covered by PMMA during the gate dielectric process, the hydrophobic SAM is formed only on the gate electrodes, while the rest of the substrate is left hydrophilic. This is important for two reasons: Due to their hydrophobic nature [75], carbon nanotubes deposited from a liquid suspension will preferably deposit on hydrophobic regions, in the present case on the SAM-covered gate electrodes. In terms of aiding the integration into large-scale circuits, this can be viewed as a first step towards the important goal of directed nanotube deposition. A second advantage of leaving the areas outside of the gate electrodes hydrophilic is that this avoids problems related to coating hydrophobic substrates with PMMA resist during the subsequent lithography for definition of the source/drain contacts [46].

After the gate stack definition, the PMMA mask is stripped to remove the aluminum outside the gate areas. The substrate is then immersed in a suspension of HiPCO SWCNTs (see Appendix A for details on the SWCNT deposition). After inspection by atomic force microscopy (AFM), the substrate is again coated with PMMA resist, areas for the source and drain contacts are opened by e-beam lithography, and a 20 nm thick layer of gold/palladium is deposited by evaporation. Finally, the PMMA is stripped to remove the metal outside of the contact areas (see Figure 3.7). An AFM image of a completed transistor is shown in Figure 3.8. The patterned aluminum gate electrode, the carbon nanotube, and the overlapping source and drain contacts are clearly visible.

Figure 3.9 shows the current voltage characteristics of a SWCNT FET with a patterned aluminum gate electrode and a phosphonic acid SAM-based gate dielectric. Owing to the large capacitance of the gate dielectric ($0.7\ \mu F/cm^2$; (ref [15])), the FET can be operated with a maximum gate-source voltage of 1 V. Immediately after fabrication the transistor exhibits a maximum drain current of 3.5 μA (at $V_{GS} = -1$ V and $V_{DS} = 0.5$ V), a transconductance of 3.6 μS, a subthreshold swing of 77 mV/decade, an on/off current ratio of 10^7, and a gate leakage current of about 10^{-13} A.

The fabrication approach presented here offers certain advantages compared with previously reported carbon nanotube-FETs. For example, the first SWCNT integrated circuits, reported in 2001 by Bachtold et al., utilized FETs with patterned aluminum gates and a native aluminum oxide dielectric [39]. These FETs exhibited a maximum drain current of 50 nA and a subthreshold swing of 150 mV/decade. In comparison, SWCNT FETs with an alkanesilane SAM dielectric have shown notably larger drain currents (2 μA) and a subthreshold swing close to the theoretical limit of 60 mV/decade (Equation 2.16). The good subthreshold characteristics were attributed to the low defect density of the SAM based gate dielectric. However, alkanesilanes are suited specifically for adsorption on silicon substrates, which makes

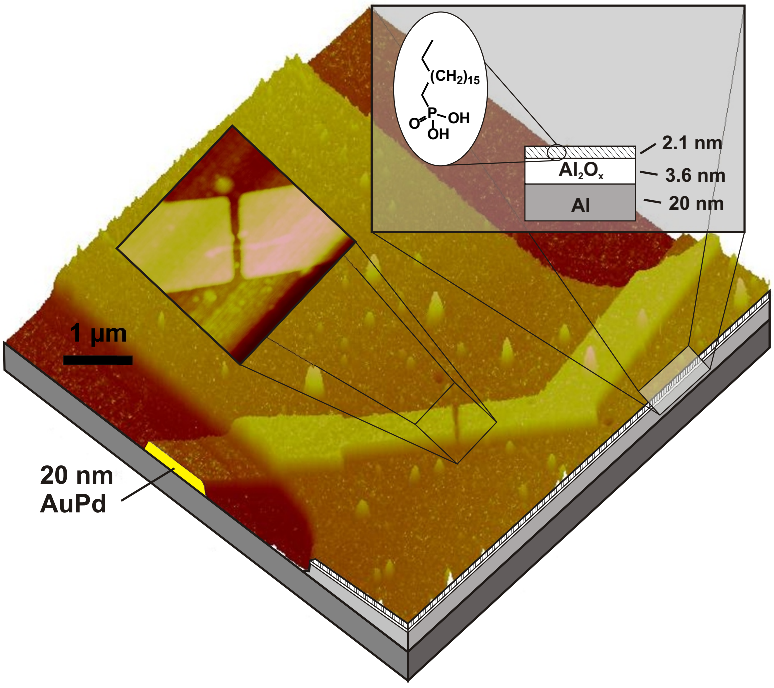

Figure 3.8: Atomic force microscopy (AFM) images of a completed carbon nanotube FET. The patterned aluminum gate electrode, the carbon nanotube, and the overlapping source and drain contacts are clearly visible.

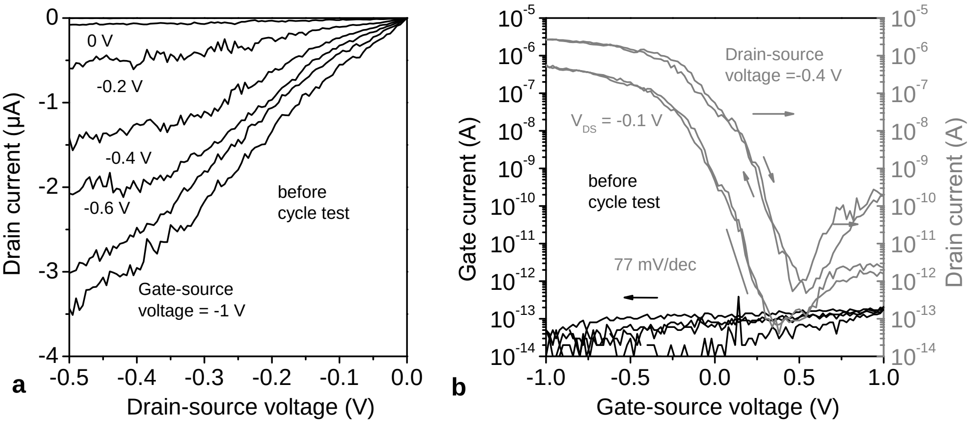

Figure 3.9: Electrical characteristics of the FET based on the local SAM-modified gate dielectric prior to the cycle test. The Output curve is shown in **(a)**, the transfer curve in **(b)**.

it difficult to utilize them for FETs with patterned gate electrodes. In order to combine the concepts of local metal gates [39] with the good device characteristics afforded by SAM dielectrics [46], alkanephosphonic acids which form high-quality SAMs on aluminum were employed [15]. They enabled SWCNT FETs with individual gates, large drain current, small gate leakage, steep subthreshold swing, and small overlap capacitance. In addition to the implementation of large-scale integrated circuits, this also opens the possibility of nanotube electronics on glass or flexible substrates. Another advantage of the SAM-based gate dielectric is that the hysteresis in the current-voltage characteristics of the FETs is notably smaller compared with hydrophilic gate dielectrics [46].

A number of groups have fabricated SWCNT FETs by depositing local gate electrodes on top of the carbon nanotubes, with a low-temperature deposited inorganic dielectric isolating the gate from the nanotube. In some of these reports the gate overlapped the source and drain contacts, so that the electric gate field controlled the entire channel from source to drain [55, 76, 65]. However, these FETs had either a large subthreshold swing ($>$ 100 mV/decade; [55, 65]) or a poor on/off current ratio [76].

In many other reports, the FETs were designed without gate-to-contact overlap, such that the gate field controlled only a portion of the channel. If the top gate does not control the entire channel from source to drain, the conductance of those sections of the nanotube not controlled by the top gate must be increased by other means. In some cases, the intrinsic conductivity of the nanotube was large and depletion-mode FETs were obtained [41, 40, 77, 66, 71], although from a circuit-design perspective enhancement-mode FETs are more desirable. Some authors employed electrostatic doping via a global silicon back gate [67, 59], which may be difficult to implement in large-scale integrated circuits. Finally, a few groups have employed chemical doping to render the ungated nanotube sections conducting and obtained FETs with excellent characteristics [63, 59]. The local bottom gate structure employed in the FETs reported here allows the gate to control the entire channel from source to drain, thus eliminating the need for chemical doping, while providing a steep subthreshold swing and a large on/off ratio.

3.2.1 Simple logic circuit based on SWCNTs

As noted earlier, an important advantage of the local bottom gate structure is that it allows FETs to be connected into circuits, without the use of a global back gate. As a proof of principle, two SWCNT FETs that were prepared on the same substrate were connected into a logic circuit. One of the FETs

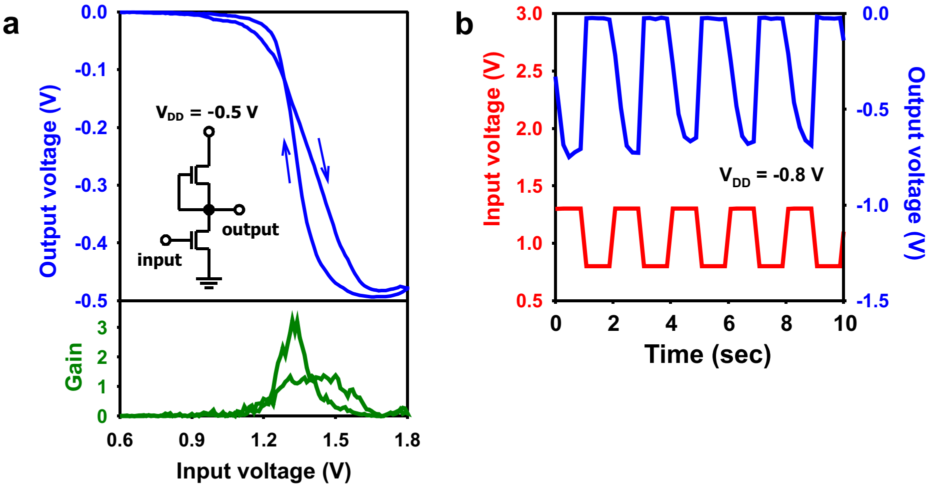

Figure 3.10: **(a)** Static and **(b)** dynamic characteristics of a unipolar inverter-like circuit composed of two SWCNT FETs with patterned metal gates and SAM-based gate dielectric on the same substrate.

serves as the drive transistor, the other one as a load (the gate of which is connected to the output node of the circuit). The electrical connection between the FETs was realized by wire bonding. The schematic and the static transfer characteristics of the circuit are shown in Figure 3.10a. The switching of the output voltage between the two logic states, 0 V and 0.5 V, is clearly observed; the hysteresis is less than 200 mV and the small-signal gain is as large as 3. Due to the positive threshold voltage of the FETs, the circuit requires positive input voltages, which means that the input and output voltages do not match and the circuit cannot be used as an inverter. Figure 3.10b shows the result of a dynamic test of the circuit, in which the input voltage was swept over a range of 0.5 V, causing the output voltage to change over a range of 0.7 V (gain $>$ 1). When the drive FET switches from the conducting to the non-conducting state, the output node (which is connected to the probe capacitance of about 10^{-11} F) is charged through the load FET (which has a resistance of about 10^{10} Ω), which leads to a signal delay on the order of 0.1 sec. For large-scale integrated circuits to operate at high frequencies, the output capacitance will have to be reduced significantly [71].

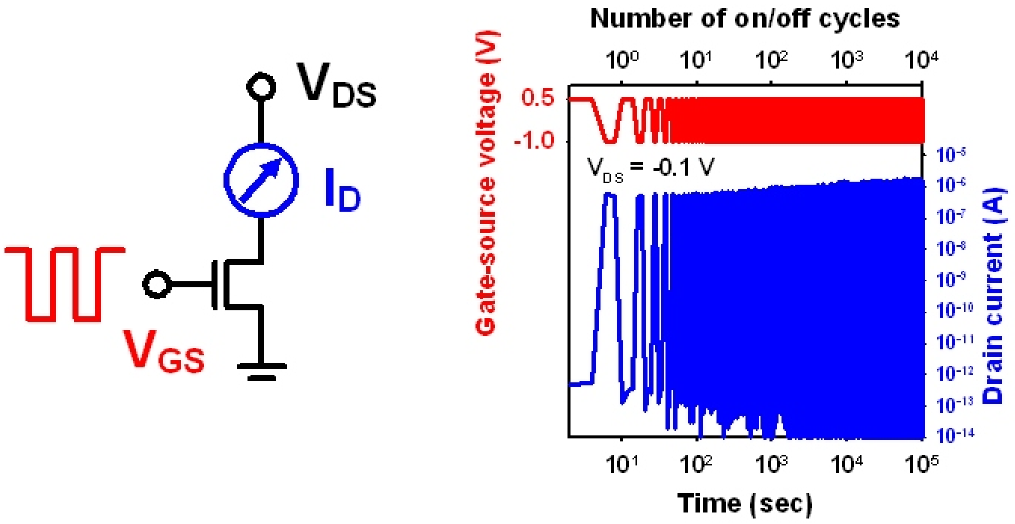

Figure 3.11: **(a)** Schematic depiction of the device setup used for the cycle test. **(b)** Recorded drain current while the FET is cycled 10^4 times between the on ($V_{GS} = 1$ V) and off state ($V_{GS} = 0.5$ V).

3.3 Reliability of SWCNT FETs

An issue that has received only little attention in literature is the operational and shelf-life stability of carbon nanotube transistors. To our knowledge there are no previous reports on the stability of SWCNT FETs during operation under air. For the possible integration of SWCNT FETs into logic devices it is, however, important to evaluate their long-term stability. In this section SWCNT FETs with local metal gates and SAM dielectric are studied with regard to their operational and shelf-life stability.

3.3.1 Operational stability

To evaluate the operational stability of the SWCNT FETs the transistor that was already investigated in Figure 3.9 was cycled 10^4 times between the on ($V_{GS} = -1$ V) and off state ($V_{GS} = 0.5$ V). During the cycle test the drain-source voltage was fixed at $V_{DS} = 0.1$ V, and the drain current was recorded continuously (see Figure 3.11a). In the course of the cycle test the on-state drain current increased by a factor of 2.5 (from 0.5 µA to 1.27 µA, measured at $V_{GS} = 1$ V and $V_{DS} = 0.1$ V), while the threshold voltage remained unchanged. In addition, the slope of the I_D vs. V_{DS} (output) curves at small drain source voltage ($V_{DS} \rightarrow 0$) increased notably

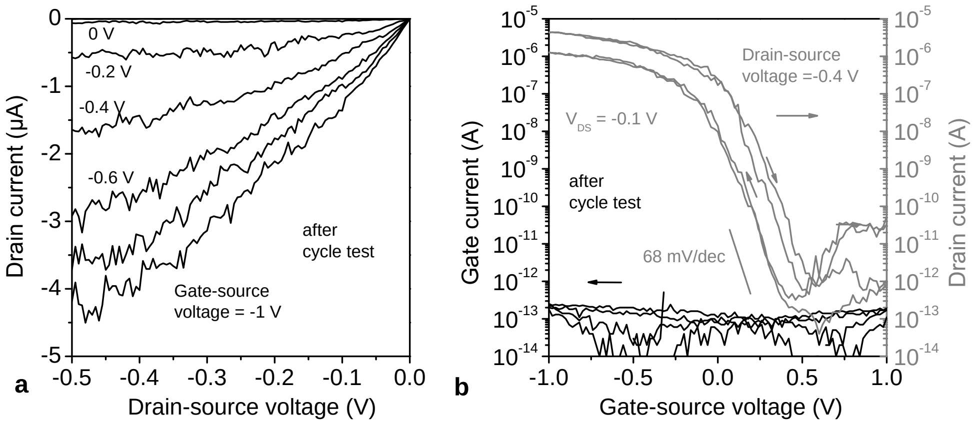

Figure 3.12: Electrical characteristics of the FET based on the local SAM-modified gate dielectric after the cycle test. The Output curve is shown in **(a)**, the transfer curve in **(b)**.

during the cycle test. These observations suggest that the performance of the source/drain contacts, i.e., the efficiency of injecting and extracting carriers at the metal/nanotube interfaces improved during the cycle test [78]. This may be related to thermal annealing as a result of an increase in the temperature near the contacts due to the large current densities during FET operation.

During the cycle test, the subthreshold swing of the transistor improved from 77 mV/decade to 68 mV/decade. Although the improvement is small and may not be a systematic effect, it is possibly related to a reduction in the density of trap states at the nanotube/dielectric interface during the cycle test. In any event, it is noteworthy that the contact injection efficiency and the subthreshold swing do not degrade during the cycle test.

In contrast to the on-state drain current and the subthreshold swing, which improved during the cycle test, the off state drain current and the gate leakage current remained essentially unchanged, both at about 10^{-13} A (i.e., close to the noise level of the setup). The fact that the gate leakage current remains small is indicative of the high quality and reliability of the gate dielectric, despite its small thickness and its fabrication at room temperature. The observation that the off state drain current remains small (10^{-13} A, measured at $V_{DS} \sim 0.5$ V) suggests that the nanotube retains its intrinsic electronic properties, i.e., it is apparently not doped during the cycle test, despite the local heating at the metal/nanotube contacts and air exposure.

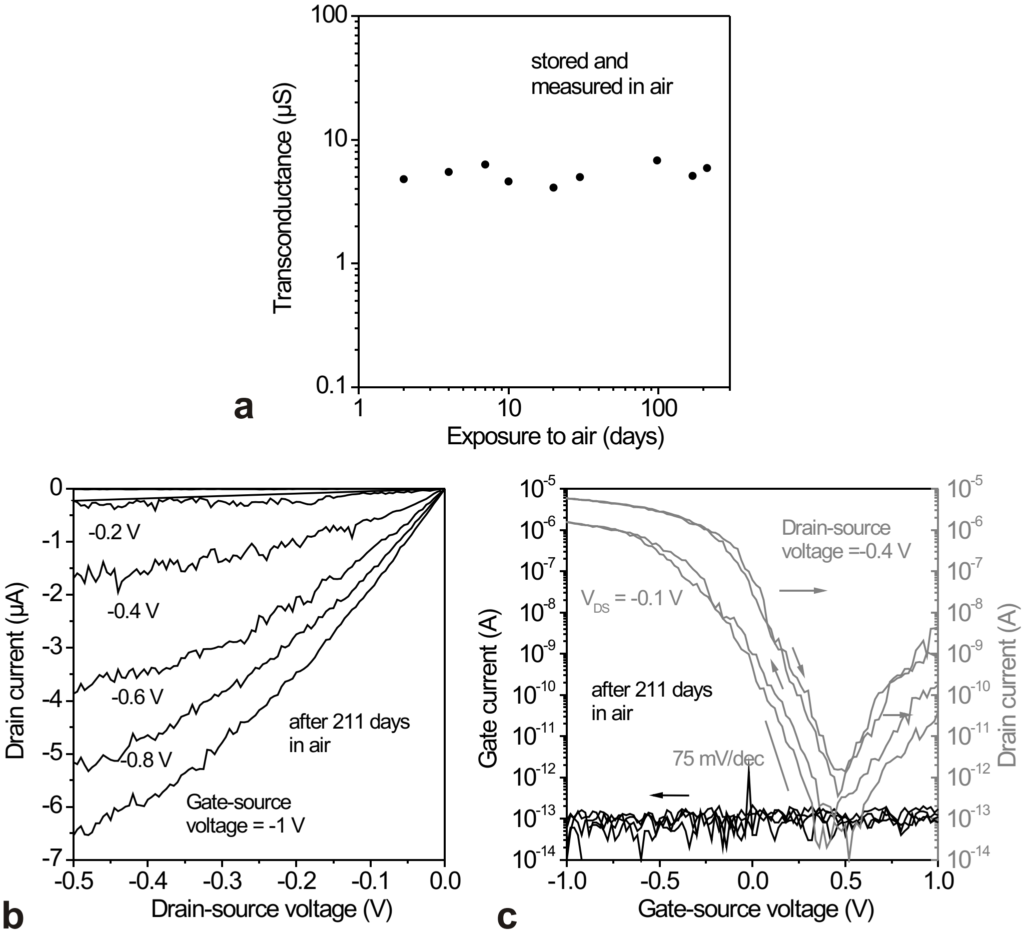

Figure 3.13: Shelf life stability of the same SWCNT FET shown in Figure 3.12. The shelf life test was started after completion of the cycle test; the characteristics of the FET at the beginning of the shelf life test are shown in Figure 3.12. **(a)** Transconductance of the FET during the shelf life test, while the substrate was kept in ambient air at room temperature. **(b)** Electrical characteristics of the FET after 211 days in air.

3.3.2 Shelf-life stability of SWCNT FETs

After completion of the cycle test, the transistor was kept under ambient air at room temperature for 211 days, during which the current voltage characteristics were measured occasionally. Figure 3.13a shows the transconductance of the transistor over time. As can be seen, there were essentially no changes in the transconductance during the shelf-life test. The electrical characteristics of the transistor after 211 days are shown in Figures 3.13b and 3.13c. The FET has a transconductance of 6 μS, a subthreshold swing of 75 mV/decade, and an on/off current ratio of 10^7.

The excellent stability of the carbon nanotube FET during the cycle and shelf-life tests testifies the chemical inertness of defect-free carbon nanotubes. This is in contrast to many of the conjugated hydrocarbons that are finding use as semiconductor in organic thin-film transistors. An example is pentacene. Pentacene thin-film transistors show good initial performance, with a subthreshold swing of 100 mV/decade and an on/off current ratio of 10^7 (ref [15]). However, pentacene is readily oxidized under ambient conditions by substitution reactions at the 6,13-positions of the molecule, yielding 6,13-pentacenequinone which acts as a scatterer or charge trap in the pentacene film [79, 80, 81, 82]. As a consequence, the transconductance of pentacene thin-film transistors exposed to ambient air decays significantly over time [83, 84, 85]. Carbon nanotubes, in contrast, are much more stable against chemical reactions, due to the lack of -CH= moieties [86], explaining the excellent stability of the SWNCT FET during the cycle and shelf-life tests reported here.

Yao et al. and Javey et al. have pointed out that transport in carbon nanotubes is ballistic over distances of at least 300 nm when the drain-source voltage is less than about $V_{DS} = 0.15$ V (ref [87, 35]). The cycle test presented here was performed on an FET with channel length of 100 nm and using a drain-source voltage of 0.1 V. Hence, interactions between the charge carriers and the nanotube are expected to be minimal and effects that might induce structural changes of the nanotube, such as Joule heating caused by the coupling between carriers and optical phonons, will be greatly suppressed.

Chapter 4

Electrochemical functionalization of SWCNTs

In Chapter 3 the excellent electrical properties of SWCNTs were utilized for the fabrication of high-performance FETs based on ultra-thin gate dielectrics. For example the SWCNT FETs showed a subthreshold swing that approached the room-temperature limit of 60 mV/decade and an operational stability of 10^5 cycles. The SWCNTs were used "as received", i.e. their properties were not altered by, for example, chemical modification. However, it would be auspicious for possible applications to implement new functionalities on the SWCNTs by for example altering their properties by chemical functionalization. Since SWCNTs consist only of surface, one can expect a strong influence of the functionalization on the properties of the tube.

One way to accomplish such a modification is electrochemistry. It offers the advantage of control over the modification extent, and furthermore ensures that modification occurs only at electrified surfaces. Such an electrochemical modification can be covalent or non-covalent. In general, covalent functionalization methods substantially alter the chemical bonding of the nanotubes by changing sp^2 into sp^3 hybridized carbons. This modification disrupts the delocalization of the π-system based on the sp^2 hybridized carbon lattice and hence strongly alters the electronic properties of the carbon nanotubes. Covalent modification schemes have been used for the fabrication of diodes via partial modification of nanotubes [88] and on-tube devices like single-electron transistors [89]. In addition, they have been successfully employed for the selective elimination of metallic nanotubes, thus providing access to purely semiconducting nanotube ensembles useful as FET channels [90].

Non-covalent modification schemes, which leave the carbon framework of the nanotubes intact, have found application in the chemical doping of nanotubes [91]. On this basis, semiconducting SWCNTs have been converted from p-to n-type [92, 93, 94] and p-n junctions have been defined within individual SWCNTs [95, 96, 97].

However,the functionalization of individual tubes with spin-carrying moieties, such as molecular magnets, has received only very little attention so far. Nanotubes decorated by a molecular magnet represent a useful model system for nanowires coupled to ferromagnetic spin chains, which are expected to show interesting electrical transport features under applied magnetic fields [98]. One important type of molecular magnet are metal coordination compounds, among which Prussian Blue (PB) ($Fe_4^{III}[Fe^{II}(CN)_6]_3 \cdot nH_2O$ (n=14-16)) is a well-investigated representative. PB displays ferromagnetic properties below its Curie temperature of $T_c = 5.6$ K. [99] It has been used as an electrocatalytic material to chemically modify bulk nanotube electrodes in the fabrication of amperometric biosensors. [100, 101, 102, 103, 104, 105, 106, 107].

In this chapter, the detailed electrical characterization of individual SWCNTs with an electrodeposited ultrathin layer of PB is presented. This can be regarded as a first step toward the realization of spintronic devices based upon nanotube-molecular magnet hybrids. To this end, first the PB deposition by electrochemical methods is introduced, and the product is characterized by spectroscopic techniques. This chapter is concluded with electrical measurements of individual semiconducting and metallic SWCNTs modified with PB. As an intriguing finding, PB-modified semiconducting SWCNTs exhibit a temperature-dependent doping characteristic, ranging from heavy p-type doping at room temperature to negligible doping at cryogenic temperatures.

4.1 Prussian Blue deposition on individual SWCNTs

Prussian Blue (PB) is usually deposited from aqueous solution containing ferric (Fe^{3+}) and ferricyanide ($[Fe^{III}(CN)^6]^{3-}$) ions, either in an electroless manner [108] or by electrodeposition.[109, 110, 111] The latter method offers the advantage of control over the deposited amount, and furthermore ensures that coating occurs only on electrified surfaces.[112] This is why the electrochemical modification is adopted for the selective deposition of PB on individual SWCNTs. Details on the parameters used for electrochemistry as well as on the sample preparation are given in Appendix B.

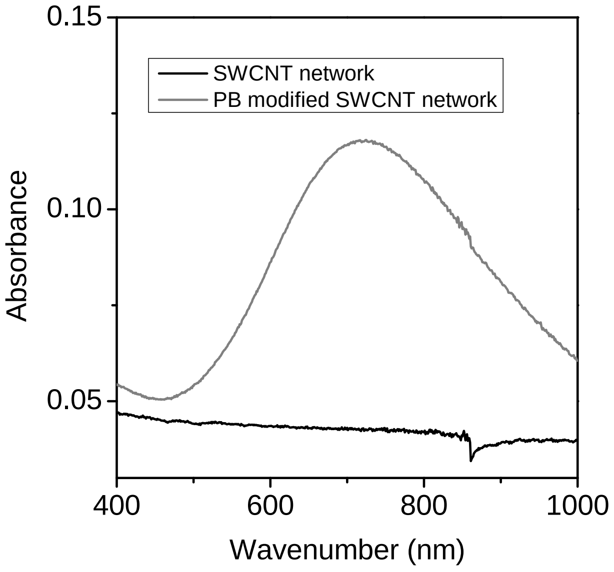

Figure 4.1: UV/visible absorption spectra of a network of SWCNTs (black) and SWCNTs with electrodeposited PB (grey) on glass coated with octadecyltrichlorosilane.

4.1.1 Spectroscopic investigation of PB

In order to prove the presence of PB on the SWCNTs modified by electrodeposition, PB-modified low-density nanotube networks were investigated using different spectroscopic techniques.

UV/visible spectroscopy

The UV/visible absorption spectrum of the PB-coated tubes exhibits a broad absorption band with a maximum at about 700 nm (Figure 4.1). This feature can be assigned to photo-induced charge transfer between Fe(II) and Fe(III) centres in the PB. [113]

X-ray photoelectron spectroscopy

X-ray photoelectron spectroscopy (XPS) data collected from a PB-covered SWCNT network are presented in Figure 4.2. Most relevant are the iron and nitrogen peaks, whose energies determined from curve fits are presented in Table 4.1 along with literature values for comparison. The N(1s) peak

	Binding energy [eV] (electrodep. PB)	**Binding energy [eV] (commercial PB)**	**Literature value [eV]**	**Assignment of peak in literature**
Fe ($2p_{3/2}$)	708.4 ± 1.2	708.1 ± 1.3	708.7 – 709.0	Fe (II) low spin unambiguously identified in lit.
	709.7 ± 2.8	709.7 ± 2.1	710-712 [1-3] (in some works not visible)	Fe (III)
	712.9 ± 3.9	713.1 ± 4.8	712.7 [4] (in some works not visible)	Fe(III) [4]
			713.6-713.8 [1,2] (in some works not visible)	Fe(II) high spin satellite[1]
Fe ($2p_{1/2}$)	721.2 ± 1.4	721.1 ± 1.8	721-721.9 [2-4]	Fe (II)
	722.8 ± 2.6	723.0 ± 2.1	723.9 [3]	Fe (III)
	725.3 ± 4.1	725.7 ± 5.2	726.1 [4]	Fe(III)
N (1s)	397.7 ± 1.2	397.4±1.1	397.8 - 398.2	N in CN unambiguously identified in lit.
	399.3 ± 2.1	398.8 ± 1.9,	398.3	KCN [5] [a]
		400.1 ± 1.4	399.6 - 400.2 [3,4]	adsorbed N_2 [b] CN-surface[3] Charge transfer [4]
	402.3 ± 2	401.8 ± 2		

Table 4.1: Survey of XPS Fe 2p and N 1s binding energies in PB (electrodeposited or commercial samples) reported in the literature and measured in the present work. The literature data include values of partially reduced PB, which may be formed via light-induced reaction at the surface. [a] Potassium peaks corresponding to KCN have also been detected in commercial PB powder, but not in our electrodeposited PB. [b] This peak is also observed on Si/SiO2 substrates with electrodes but without CNTs and without PB. (1: Ref [114]; 2: Ref [115]; 3: Ref [116]; 4: Ref [117]; 5: Ref [118])

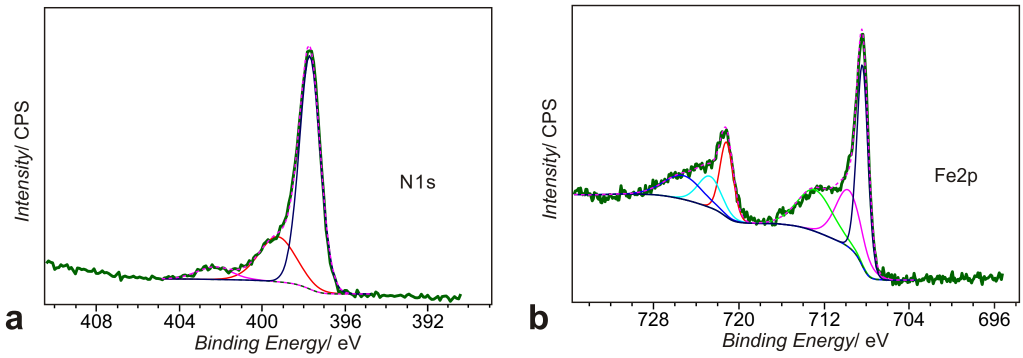

Figure 4.2: X-ray photoelectron spectra of PB electrodeposited galvanostatically, in the N 1s **(a)** and Fe 2p **(b)** regions. The substrate was a SiO_2 coated Si wafer covered with a network of SWCNTs contacted by AuPd electrodes.

occurring at 397.7 eV indicates the presence of nitrogen in the cyano ligand, while the shoulder at 399.3 eV is due to N_2 absorbed on the surface. The weak peak at 402.3 eV most likely originates from surface contaminations.

A detailed analysis of the iron peaks is complicated by the fact that the binding energy of the Fe ions is affected by multiplet splitting, satellite features and different oxidation states.[119] This has led to considerable discrepancies in the peak assignments as reported in the literature. The Fe 2p area is composed of two groups of peaks, each of which could be fitted by three components. Comparison with the literature values indicates that the group at higher binding energy with components at 708.4 eV, 709.7 eV, and 712.9 eV comprises the Fe 2p3/2 signal, while the lower energy group with components at 721.2 eV, 722.8 eV, and 725.3 eV corresponds to Fe 2p1/2. Moreover, the peaks at 708.4 eV and 721.2 eV can be reasonably assigned to Fe(II), and the peaks at 709.7 eV and 722.8 eV to Fe(III). On this basis, the two remaining peaks at 712.9 eV and 725.3 eV could be explained as satellites belonging to Fe(II), which occur due to surface reduction of high-spin Fe(III) to high-spin Fe(II), in agreement with previous observations. [119, 114]

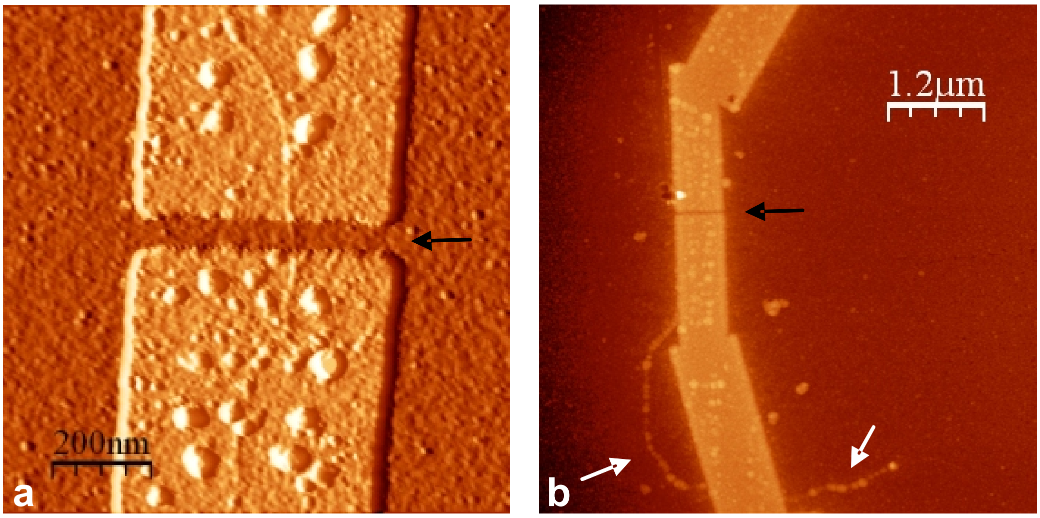

Figure 4.3: **(a)** Atomic force microscopy (AFM) image of an individual SWCNT contacted by two AuPd electrodes. The distance between the electrodes is 100 nm (black arrow). **(b)** AFM image of the same structure after modification with PB. Between the electrodes the SWCNT cannot be seen anymore due to the scansize. However, a SWCNT located outside the gap can be seen to be covered with PB (white arrows).

4.2 Electrical transport through PB-coated SWCNTs

In Figure 4.3, AFM images of individual contacted SWCNTs are shown before and after PB electrodeposition. Successful decoration has been achieved with both, metallic and semiconducting nanotubes under the same electrochemical conditions. In addition to the coating on the tubes, PB deposits can be seen on the electrodes and the adjacent Si/SiO$_2$ substrate area. Although the amount of PB deposited on the substrate decreases with distance from the electrodes, the space between the electrodes (typically 100 nm wide) appears to be filled with a homogeneous PB layer. The possibility that this layer contributes to the electrical conduction between the electrodes was excluded by test experiments wherein PB was deposited into electrode gaps without a nanotube, which yielded very high resistances exceeding 10 GΩ.

Modification of metallic SWCNTs with PB

In the case of metallic SWCNTs, the PB coating did not alter the electrical resistance (Figure 4.4). This observation is in good agreement with

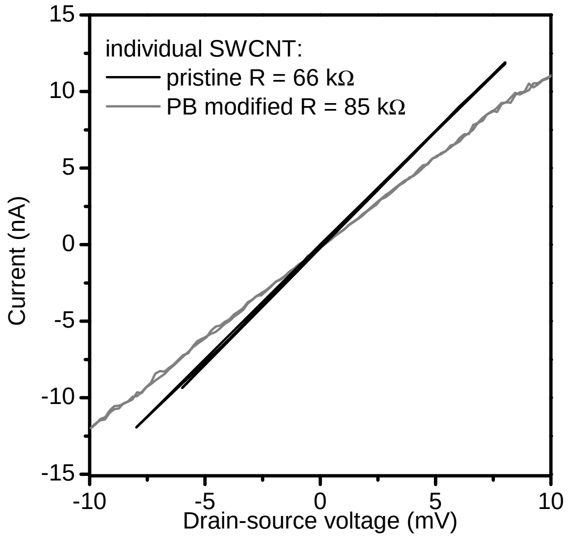

Figure 4.4: Individual SWCNT before and after electrochemical modification with Prussian Blue (PB). The resistance of the SWCNT is hardly affected by the PB deposition.

previous studies on the non-covalent modification of metallic tubes,[91] providing that neither covalent bonding between the CNT and the PB takes place, nor are defects introduced by the electrochemical modification. In fact, covalent attachment is well-documented to disturb the sp^2 carbon network by introducing sp^3 conjugated carbons, thereby significantly reducing the tube's conductivity.[120] Moreover, the presence of sp^3 centers or other types of defects would be manifested in a noticeable gate dependence of conductance,[120] which is, however, not observed.

Modification of semiconducting SWCNTs with PB

Contrary to the metallic SWCNTs, the electrical transport properties of semiconducting SWCNTs were found to be strongly influenced by electrochemical functionalization with PB. As apparent from Figure 4.5a, before coating the semiconducting tubes display the characteristic p-type behaviour (red curve), i.e., decreasing current with increasing gate voltage,[121, 46] whereas after PB coating, the gate dependence under ambient conditions as well as at tem-

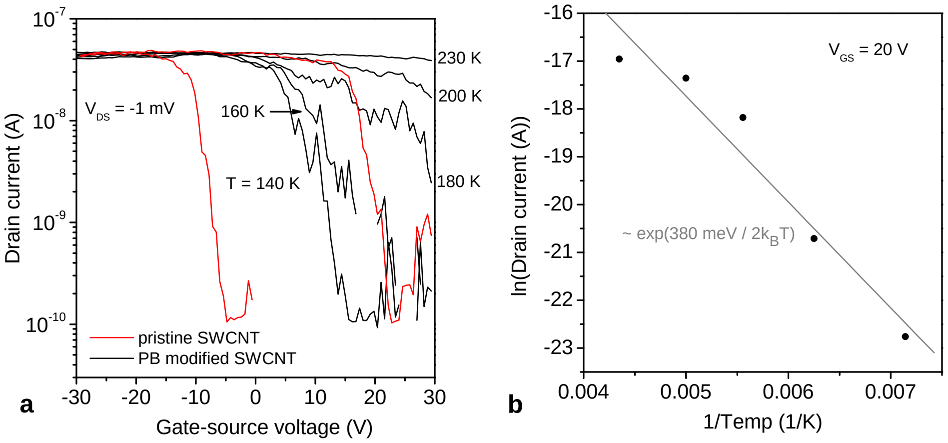

Figure 4.5: **(a)** Drain current as a function of applied gate-source voltage for an individual semiconducting SWCNT. The curve in red shows the gate dependence of the pristine tube at room temperature. After electrochemical modification with PB, the gate dependence at room temperature has vanished (shown in black). Upon cooling down to 140 K the gate dependence is slowly recovered. **(b)** Arrhenius plot of the drain current at V_{GS} = 20 V.

peratures as low as 230 K is effectively eliminated.[63] This change can be explained by strong p-doping of the SWCNT whereupon the threshold voltage is shifted toward much higher gate-source voltages. Such type of doping is consistent with the electron transfer from the nanotube to Fe(III) ions in the PB deposition solution that occurs during the electrodeposition process. As the electrodeposition bath is acidic (pH = 2), control experiments were performed in which PB was deposited in an electroless manner [108] onto semiconducting SWCNTs. The obtained results clearly demonstrate that the PB coating is responsible for the observed effect, although an additional doping contribution by H_3O^+ ions under the condition of an applied potential [120, 122, 123] cannot be completely ruled out.

Temperature-dependent electrical measurements of PB-modified SWCNTs

Further electrical characterization of the PB-decorated semiconducting nanotubes revealed an intriguing change in the electrical behavior upon cooling of the samples. In particular, when the temperature is lowered from 230 to

140 K, a full recovery of the original gate dependence, with a current modulation of over three orders of magnitude, is observed (Figure 4.5a). The decrease of the current with decreasing temperature may in principle originate from a temperature dependence of the charge carrier mean free path and/or the charge carrier density in the tubes.

Possible contributions of contact resistance to the temperature dependence of the current can be neglected due to the usually low on-conductance of the nanotubes which is as low as 0.5 G_0, with $G_0 = 4e^2/h$ being the conductance quantum. [24]

Moreover, the existence of a significant temperature dependence of the mean free path is unlikely in view of the almost identical on currents detected at the various temperatures.

From low-temperature measurements of pristine and PB-coated semiconducting SWCNTs it can be inferred that only a minor amount of defects is introduced by the PB coating and the mean free path of the charge carriers is thus not influenced by the coating. In a semiconducting SWCNT with a short channel (100 nm in the present case) transport is expected to be ballistic[35, 56]. In a SWCNT with ballistic conduction, if the coupling of the SWCNT to the contacts is strong (as in the present case), Fabry-Perot interferences are expected to be visible at low temperatures [124]. These oscillations emerge because the nanotube acts as a coherent electron waveguide, with a resonant cavity formed between the two nanotube-electrode interfaces.

Fabry-Perot interferences have been observed in semiconducting [56] and metallic SWCNTs [124] with a conductance of at least 0.1 G_0. In Figure 4.6, the gate dependence of the drain current at T = 2.2 K of an individual semiconducting SWCNT with a maximum conductance of 0.5 G_0 is shown before and after electrochemical modification with PB. Fabry-Perot type modulations of the drain current are visible in both the pristine as well as the PB-doped nanotube.

The observed Fabry-Perot-like oscillations before and after the coating with PB do not have a regular periodicity like they have been observed in other works [124], but are rather composed of oscillations with different periodicities. The theoretically expected periodicity for the electrode spacing used in this experiment (100 nm) is $\Delta V_{GS} = hv_F/2\alpha L = 1$ V [125] (with h Planck's constant, $v_F \sim 8 \times 10^5$ m/s the Fermi velocity [125], $\alpha = 0.0165$ the gate coupling factor determined from Figure 4.7, and $L = 100$ nm the electrode separation). The apparent divergence of the observed periodicity ($\Delta V_{GS} \sim 3 - 5$ V) from the theoretically expected fluctuations as well as the observed overlay of multiple oscillations can be attributed to localized states in the SWCNT that might be caused by chemical defects already present be-

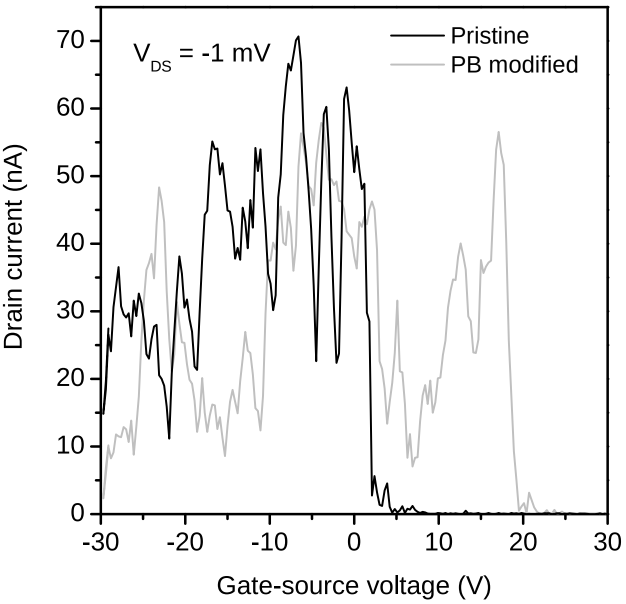

Figure 4.6: Fabry-Perot-like oscillations recorded at a temperature of 2.2 K in a helium cryostat of an individual semiconducting SWCNT before and after electrochemical modification with PB. The maximum conductance of the unmodified devices is 0.5 G_0. In this device the threshold voltage at 2.2 K has shifted to more positive gate voltages in the modified device. However, this was not observed in all devices.

fore the PB coating [125]. After the PB coating, Fabry-Perot-like oscillations are still visible at low temperatures, however with different periodicites than before. This can be attributed to the interaction between the PB and the conduction electrons in the SWCNT. In any case, the observation that the Fabry-Perot-like oscillations are not disturbed upon PB-coating reveals that the strong hole doping by the PB does not introduce strong scattering sites that significantly reduce the ballistic mean free path of the charge carriers in the SWCNT. This in turn means that the carrier mobility does not change upon modification of the SWCNTs with PB.

Accordingly, the most plausible scenario is that upon lowering the temperature, the transfer of holes from the nanotube to the PB is frozen out, in analogy to the well-established behavior of doped conventional semiconductors. In the following, the simple model of semiconductors (shown in section

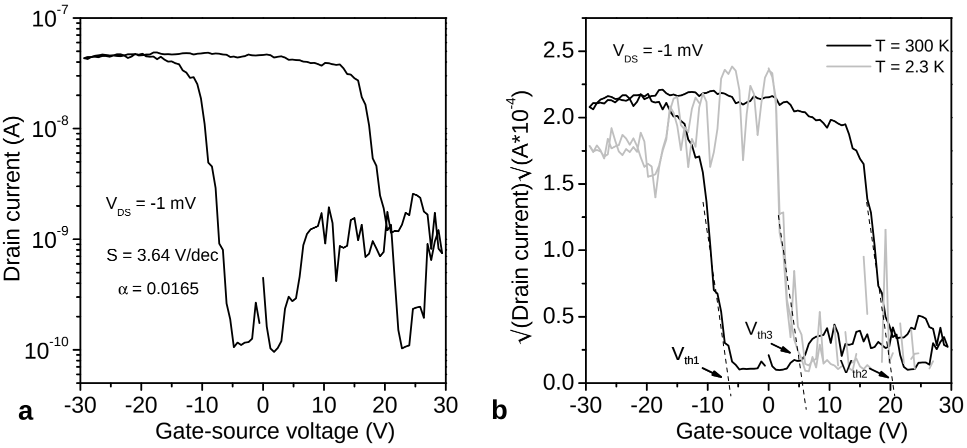

Figure 4.7: Transfer curve of the pristine SWCNT. **(a)** At room temperature the logarithmic depiction of the drain current allows for calculation of the subthreshold swing. The subthreshold swing allows for calculation of the gate coupling parameter α (defined in Equation 2.16. **(b)** The square-root plot of the transfer curve yields the threshold voltage V_{th}. Since V_{th} depends on temperature, the transfer curves at room temperature and at cryogenic temperature have to be evaluated. In order to also include the influence of the gate voltage window used for the measurement, as a rough estimate a temperature and sweep-voltage-independent threshold voltage is calculated according to $((|\mathrm{V_{th1}}| + |\mathrm{V_{th2}}|)/2 + |\mathrm{V_{th3}}|)/2(V_{th1} = 6.6$ V; $V_{th1} = 20.3$ V ;$V_{th3} = 5.4V)$. This gives an average, temperature-independent V_{th} of 9.4 V.

2.2.7) will be applied for analyzing the temperature dependence of the gate current. However, as described in section 2.3, this is only an approximation. As derived in section 2.2.7, in a doped semiconductor, the drain current $\mathrm{I_D}$(T) varies with temperature as

$$I_D \propto \exp\left(-\frac{E_a + e\alpha(V_{GS} - V_{TH})}{2k_BT}\right), \tag{4.1}$$

with E_a as the energy level of the dopants measured from the valence band edge (for hole doping in a p-type conductor), k_b Boltzmann's constant, T the temperature and V_{TH} the threshold voltage. The threshold voltage can be extracted from the square-root plot of the gate dependence as shown in Figure 4.7. From the transfer curves recorded at different temperatures (Figure 4.5a) the drain current I_D at $\mathrm{V_{GS}} = 20$ V has been extracted and plotted in Figure 4.5b. From the slope of the curve (380 meV) the activation energy of the PB-dopants can be calculated to $E_a = 380\ \text{meV} - 0.0165(20 - 9.4) = 224\ \text{meV}$. Future low-temperature experiments under the influence of external magnetic fields are expected to provide valuable insight regarding the implementation of carbon nanotube-based spintronic devices.

Chapter 5

N-channel organic field effect transistors

In the previous chapter, field effect transistors (FETs) comprising single-walled carbon nanotubes (SWCNTs) were investigated. However, there exists another approach to integrating organic semiconductors into functional electronic devices. This approach utilizes small organic molecules for the semiconducting channel in a FET structure.

This chapter will be focussed on novel core-cyanated perylene carboxylic diimides that can be employed in the fabrication of air-stable n-channel organic field effect transistors. The first part of the chapter will be focussed on the fabrication, electrical and structural characterization of FETs based on thin films of five core-cyanated perylene carboxylic diimides and the stability of their electrical characteristics in different environments. The second part will be focussed on the fabrication on individual nanowire transistors based on one of the perylene carboxylic diimides. The nanowires are fabricated using a self-assembly approach in solution. The air stability of the mobility of the nanowire FETs will be investigated and compared to that of FETs based on thin films of the same compound.

5.1 Introduction

Organic semiconductors are in principle expected to show ambipolar transport characteristics[126] with both p-type and n-type conduction when employed as the active layer in a FET. In practice, the majority of the organic thin-film FETs reported to date show either p-type or n-type behavior, but not both simultaneously. This phenomenon is actually advantageous for organic transistor applications, since ambipolar transport through the FET channel would lead to unacceptably large leakage currents, so that the transistor could not be completely turned off. (CMOS transistors are ambipolar, but the leakage currents are very small (< 1 pA) since the contacts are selectively doped p-type or n-type such that space charge regions block undesired injection and leakage. For organic FETs, however, reliable contact doping has remained elusive.)

Several mechanisms are responsible for the often unipolar characteristics of organic FETs. One is the fact that in most organic semiconductors the HOMO-LUMO gap is sufficiently large that only one of the two orbitals (usually the HOMO) is accessible for the efficient injection of charge carriers from the contacts. A second mechanism that promotes unbalanced transport is the selectivity of the deep trapping of injected carriers in the channel [126]. It appears that in many organic semiconductors negative charge carriers are trapped more efficiently than positive carriers, either at interfaces (such as the semiconductor/gate dielectric interface or at grain boundaries within the semiconductor) or by environmental traps (generated presumably by oxygen, water, or ozone). As a result, most organic FETs show p-channel behavior.

Approaches for the realization of n-channel organic FETs

A number of strategies have been developed to obtain organic FETs that operate as n-channel devices [127]. One is the use of a combination of organic semiconductor and electrode material for which electrons can be efficiently injected into the LUMO, as schematically depicted in Figure 5.1. This can be realized either by choosing a semiconductor with a large electron affinity or a contact metal with a low workfunction, or both. Another strategy is the elimination of electron traps from the transistor by passivating the dielectric interface and/or operating the FET in an oxygen-free environment. Examples for the successful implementation of these two strategies include n-channel FETs based on C_{60} (ref [128, 129]) or (hydrocarbon-functionalized) naphthalene or perylene carboxylic dianhydrides or diimides [130, 131, 132, 133, 134, 135]. Other examples are n-channel FETs based on pentacene [136] or poly(9,9 dioctylfluorene) [126] that employ low workfunction metal contacts and a dielectric interface with a reduced density of active electron traps. Generally, all these transistors operate properly only in vacuum or an inert atmosphere, apparently because certain species present in ambient air, such as oxygen, easily diffuse into the semiconductor and destabilize or

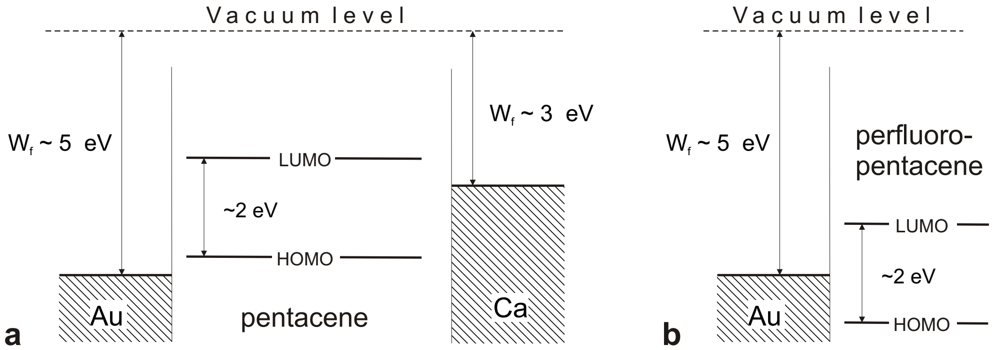

Figure 5.1: **(a)** Schematic energy diagram of the relative alignment of the Fermi level of pentacene and gold and calcium electrodes. Gold, with its work function (W_f) of around 5 eV, can efficiently inject holes into the HOMO, but no electrons into the LUMO. In comparison, from a calcium electrode electrons can be efficiently injected into the LUMO of the pentacene, since Ca has a relatively low work function of about 3 eV **(b)** A way of enabling the injection of electrons from a gold electrode into the LUMO of a semiconductor is to lower the LUMO as well as the HOMO by utilizing molecules that have been functionalized with electron-withdrawing substituents such as fluorine.

trap the negative charge carriers in the channel. (This does not mean that the organic semiconductor is destroyed by oxygen exposure; devices typically recover upon returning to an inert ambient.)

Fluorine functionalization for the realization of air-stable n-channel FETs

A third strategy that has been developed and which has led to the demonstration of organic n-channel FETs that can be operated in air is the functionalization of conjugated compounds with fluorine-rich substituents. This was first reported by Bao and coworkers for copper phthalocyanine (CuPc).[137] FETs based on CuPc only show p-channel operation, while FETs based on the perfluorinated counterpart, F_{16}CuPc, operate as n-channel FETs in air with a mobility of 0.03 cm^2/Vs and excellent long-term stability [138, 15]. This raises the question about the mechanism by which the fluorine-containing substituents promote air stability. Fluorine functionalization to create organic semiconductors for n-channel FETs works for other material systems as well, e.g., for naphthalene carboxylic diimides [139, 140, 141], perylene carboxylic diimides [142, 143], oligothiophenes [144, 145, 146, 147, 148, 149, 150],

and pentacene [151, 152]. However, although these materials have demonstrated n-channel FET operation, not all of them operate in air. It appears that fluorine functionalization generally helps in obtaining n-channel FETs, but that it promotes air stability only for certain types of materials (such as $CH_2C_6H_4CF_3$-functionalized naphthalene carboxylic diimide FETs that show a n-channel mobility of 0.12 cm^2/Vs both in vacuum and in air [139]), but not for others (such as FETs based on perfluorinated pentacene [152] or fluoroalkyl oligothiophenes [149]). The origin of this difference remains unclear, especially since in some cases fluorine functionalization appears to actually reduce the mobility. For example, FETs based on $CH_2(CF_2)_6CF_3$-substituted naphthalene carboxylic diimide have shown n-channel mobilities that are three times smaller than the n-channel mobilities of FETs based on the $(CH_2)_7CH_3$-substituted derivatives ($\sim$ 0.05 cm^2/Vs vs. 0.16 cm^2/Vs, both measured in vacuum)[139].
Recently, Jones et al. synthesized two perylene carboxylic diimide derivatives with a cyano-functionalized perylene core and obtained n-channel FETs with excellent performance in air [153]. One of the compounds was end-functionalized with cyclohexane groups and showed a mobility of 0.1 cm^2/Vs, while the other was end-functionalized with fluoroalkyl substituents and exhibited a mobility of 0.6 cm^2/Vs. Apparently, functionalizing only the perylene core with strongly electron-withdrawing groups (e.g., cyano groups[153] or chlorine groups[154, 155]) is sufficient to induce air stability, while the additional functionalization of the diimide groups with electron-withdrawing substituents promotes a further increase of the mobility in air. In the case of fluoroalkyl-substituted naphthalene and perylene carboxylic diimide derivatives, the observation of air-stability has been attributed to the close packing of the fluoroalkyl substituents. These functionalities are believed to act as a kinetic barrier against oxygen penetration into the film [139, 153].

With the intent to elucidate the role of the fluorine functionalities in the air stability of perylene derivatives, a series of core-cyanated perylene carboxylic diimides end-functionalized with more or less fluorine rich and more or less bulky substituents were synthesized and characterized. All five compounds show n-channel FET behavior in air, with mobilities that span several orders of magnitude, but all with a very similar rate of degradation in air.

5.2 Thin film n-channel FETs based on perylene diimides

The five compounds, shown in Figure 5.2, were synthesized according to the general procedure described by Katz et al., Shi et al., and Jones et al. (for details on the synthesis please refer to Appendix C).[139, 153, 156] Compound **2** is the same as the one reported by Jones et al., while compounds **1, 3, 4** and **5** have not been previously reported. For structural and electrical characterization, 30 nm thick films of each compound were deposited by thermal evaporation in vacuum onto heavily doped, thermally oxidized silicon substrates covered with a hydrophobic self-assembled monolayer (SAM) of octadecyltrichlorosilane (OTS)[157]. Structural characterization of the organic films was performed by atomic force microscopy (AFM) and X-ray diffraction (XRD). Thin-film FETs were prepared by evaporating 30 nm thick gold source/drain contacts directly onto the organic films (Figure 5.10). All electrical measurements were performed in air at room temperature.

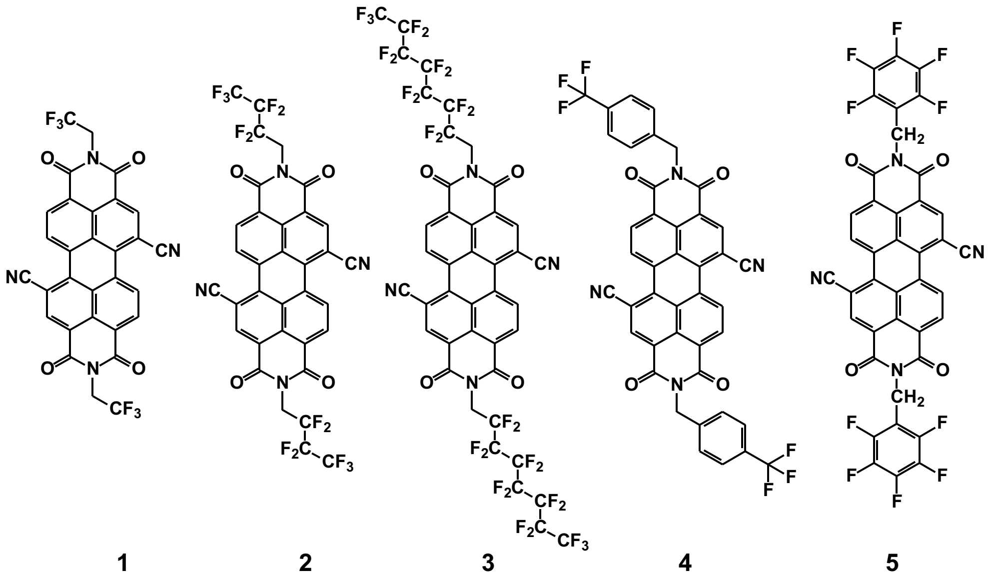

1 **2** **3** **4** **5**

Figure 5.2: Organic semiconductors investigated in this chapter.

5.2.1 Investigation of the structure of the organic films

The AFM and XRD data indicate that the film morphology depends strongly on the substrate temperature, but also on the substituent. First, the morphology of films prepared from compound **2** will be discussed, since this is the compound that has shown the largest carrier mobility.

Investigation of thin films of compound 2 by Atomic Force Microscopy (AFM)

Films of compound **2** deposited onto substrates held at a temperature of 140 °C show the highest degree of molecular order, judging from the AFM data (Figure 5.3b). Large crystallites composed of flat terraces and abrupt steps as well as screw dislocations can be seen. Between the individual crystallites, areas of the substrate not covered with the deposited compound are clearly observed, suggesting that at this temperature the material partially dewets the surface. The film appears to be composed of two polymorphs [158], i.e. two areas in which the molecules are arranged in different orientations (Figure 5.3b): Polymorph A is characterized by terraces with round edges, whereas in polymorph B one edge of each terrace is usually faceted. Under an optical microscope the two polymorphs have different colors: A appears red, whereas B appears green (Figure 5.4). The formation of two polymorphs showing different molecular arrangements as well as colors has been previously reported for perylene [159] and perylene derivatives [160, 161]. The different colors of the two polymorphs were attributed to excitonic effects [160].

When compound **2** is deposited at substrate temperatures below 140 °C the films are characterized by full surface coverage, but appear less ordered; this can be seen in the AFM images of films deposited at 120 °C (Figure 5.3a) and 100 °C, 80 °C and 25 °C (Figure 5.5). In the AFM images of the films grown at 120 °C only polymorph A is visible, i.e. the islands are usually round (Figure 5.3), and under an optical microscope they appear red. (Note that from the AFM data alone we cannot rule out that polymorph B also exists at 120 °C.) At deposition temperatures below 100 °C, the terraces are less pronounced, indicating that these films are even less ordered.

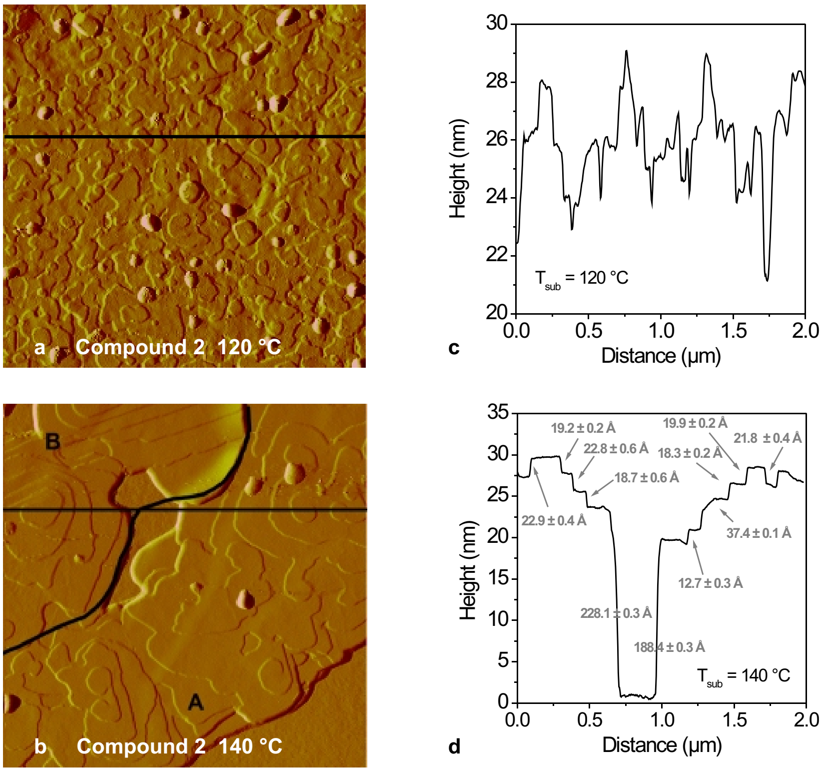

Figure 5.3: **(a)** Atomic force microscopy (AFM) amplitude image (size 2x2 µm^2) of a 30 nm thick film of compound **2** deposited at a substrate temperature of 120 °C. **(b)** AFM amplitude image of compound **2** deposited at a substrate temperature of 140 °C. In both images, islands with discrete steps and screw dislocations can be recognized. The boundary between polymorph A and B is marked by a black line. Panels **(c)** and **(d)** are line scans at the positions indicated by the black lines in **(a)** and **(b)**.

Investigation of thin films of compound 2 by X-Ray Diffraction (XRD)

In order to gain further insight into the film structure at different temperatures and to elucidate the two polymorphs observed by AFM, X-ray diffraction measurements on the films of compound **2** were performed (For details on the XRD procedure please refer to Appendix C). Out-of-plane X-ray diffraction and grazing incidence x-ray diffraction (GIXD) measurements were performed on films deposited at 25 °C, 80 °C, 120 °C and 140 °C (Figure 5.6a). The XRD data show that the films grown at 25 °C are completely

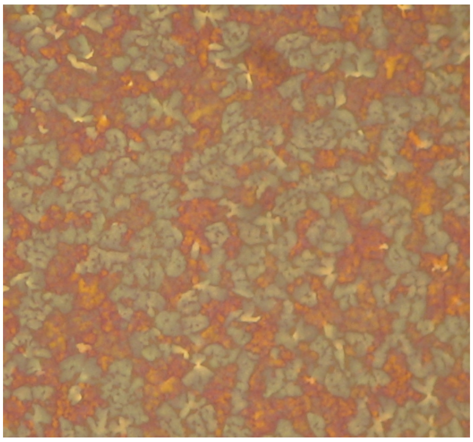

Figure 5.4: Optical micrograph of compound **2** deposited at 140 °C substrate temperature.

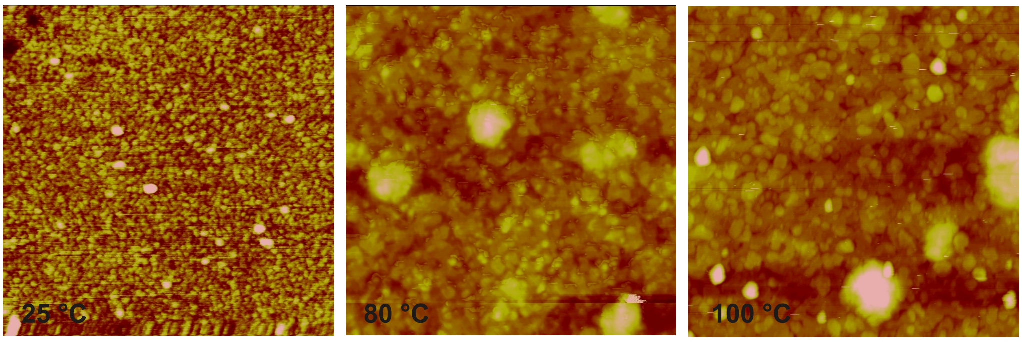

Figure 5.5: AFM images (2 x 2 μm^2) of compound **2** deposited at respective substrate temperatures of 25 °C, 80 °C and 100 °C.

amorphous, as can be discerned from the absence of discrete Bragg peaks in the spectrum. Pronounced Kiessig oscillations arising from interference between the surfaces of the semiconductor film and the substrate show that the films deposited at this temperature are very smooth (with a mean square roughness of only 8.6 Å). Films grown at 80 °C display a small degree of short-range molecular order, and films grown at 120 °C and 140 °C are characterized by a large degree of crystalline molecular ordering.
For the films grown at 120 °C and 140 °C the out-of-plane Bragg reflections display two distinct peaks, one peak is associated with a d-spacing of 19.2 Å ($q_z = 0.3279$ Å^{-1}) and the other one with a d-spacing of 9.2 Å

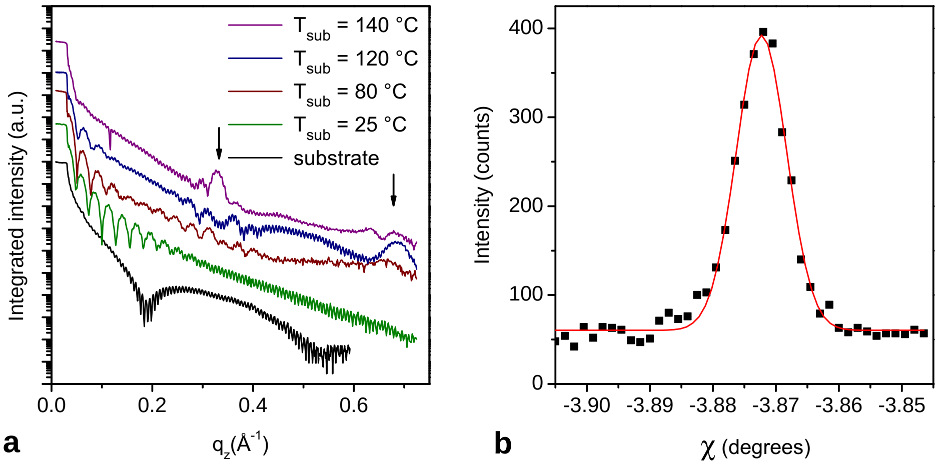

Figure 5.6: **(a)** Specular XRD data of the OTS-covered Si/SiO$_2$ substrate and of thin films of compound **2** deposited at different substrate temperatures. **(b)** Rocking curve obtained for a film of compound **2** deposited at a substrate temperature of 120 °C (q = 0.68342 Å^{-1}). The data are shown in black, the fit to the data calculated using the Parratt32 software based on the Parratt algorithm is shown in red.

(q_z = 0.6834 Å^{-1}). The finding of two periodicities confirms that compound **2** crystallizes in two different polymorphs [158] characterized by different orientations of the molecules. The d-spacing of 19.2 Å is similar to the step heights measured by AFM in both polymorphs (usually between 19 and 21 Å), while the d-spacing of 9.2 Å is much smaller than the step heights measured by AFM. This apparent discrepancy can be explained by assuming that in polymorph A the molecules form layers with a thickness of two molecules. Thus, the observed d spacing of 9.2 Å would correspond to a step height of 18.4 Å (which is indeed similar to what we measured by AFM). In this picture, in polymorph A the molecules would be oriented with their long axis parallel to the substrate, in polymorph B, however, they would be oriented with their long axis approximately upright on the substrate surface. In fact, in polymorph A (but not in polymorph B) occasionally steps with a height significantly smaller than 19 Å were found (Figure 5.3d and Figure 5.8), which supports the existence of the two polymorphs. Judging from the relative intensity of the peaks found for the two periodicities, films deposited at a temperature of 120 °C seem to be predominantly composed of poly-

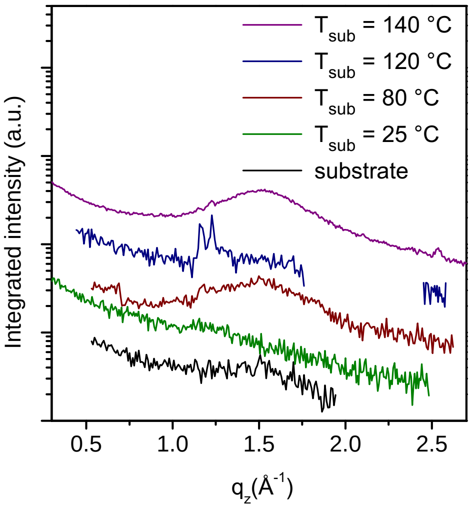

Figure 5.7: Grazing Incidence X-Ray Diffraction (GIXD) data obtained for a film of compound **2** deposited at different temperatures. In-plane reflections observed for the films deposited at 120 °C and 140 °C correspond to an in-plane spacing of 5.39 Å and 5.12 Å, respectively. Note that at a reciprocal wave vector of 2.53 Å^{-1}, an in-plane reflection is seen for the 140 °C film, but not for the 120 °C film. In contrast, the reflections at 1.15 Å^{-1} and 1.22 Å^{-1} are observed in both films. This finding supports the hypothesis of the presence of two polymorphs in films deposited at a substrate temperature of 140 °C.

morph A. The degree of molecular alignment in this polymorph is excellent, with a mosaicity of 0.008 estimated from the Full Width at Half Maximum (FWHM) of the rocking curves (Figure 5.6b).
The large degree of crystallinity and the presence of two different molecular orientations are also apparent from the grazing incidence x-ray diffraction (GIXD) data (Figure 5.7b). A more detailed crystallographic study will be necessary to confirm the proposed molecular ordering of the two polymorphs. In both polymorphs the molecular arrangement provides a favorable overlap in the direction of charge transport parallel to the substrate surface.

Investigation of the thin film structure of compounds 1 and 3-5

Compared with compound **2**, compound **1** has a shorter fluoroalkyl substituent, compound **3** has a longer fluoroalkyl substituent, and compounds **4** and **5** have cyclic substituents. Of all five materials, compound **1** has by far

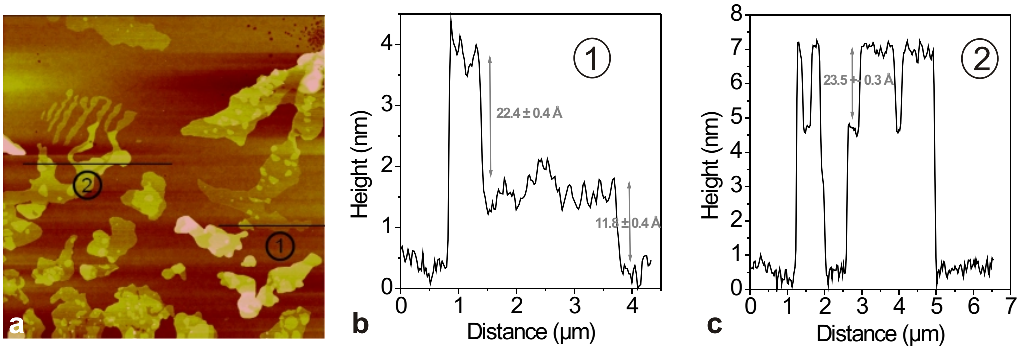

Figure 5.8: **(a)** AFM image (13.1 x 13.1 μm^2) of a region of the substrate that was partially shaded by a clamp during the vacuum deposition, so that individual islands of compound **2** deposited at a substrate temperature of 140 °C can be observed. **(b)** Scan at position **1** as indicated in **(a)**. A step with a step-height of 11.8 Å can be observed suggesting that the molecules are oriented with their long axis parallel to the substrate. **(c)** Scan at position **2** as indicated in **(a)**. The step-height is 23.5 Å.

the strongest tendency to dewet the surface. Disconnected islands are formed at substrate temperatures as low as 60 °C. This is apparently a consequence of the shorter substituents. To obtain full surface coverage with compound **1**, the substrate temperature must be reduced to 25 °C, and at this temperature the films appear entirely disordered (Figure 5.9). Compound **3**, on the other hand, requires higher substrate temperatures to create a high degree of molecular order. When deposited at a substrate temperature of 140 °C, crystallites with a step height of 28.5 ± 0.8 Å are seen in the AFM images (Figure 5.9). Thus, the step height in films of compound **3** is larger by about 9 Å than the step height in polymorph A of compound **2**. From this it can be concluded that the molecules of compound **3** are not oriented in the same way as polymorph A of compound **2**, i.e. not with their long axis parallel to the substrate. Instead, the molecules of compound **3** can be imagined to stand with their long axis approximately upright on the substrate surface. When deposited at a substrate temperature of 140 °C, compound **4** forms closed layers with discrete steps while compound **5** grows in disconnected islands. At a substrate temperature of 120 °C both compound **4** and **5** form closed layers, although the films appear less ordered (5.9).

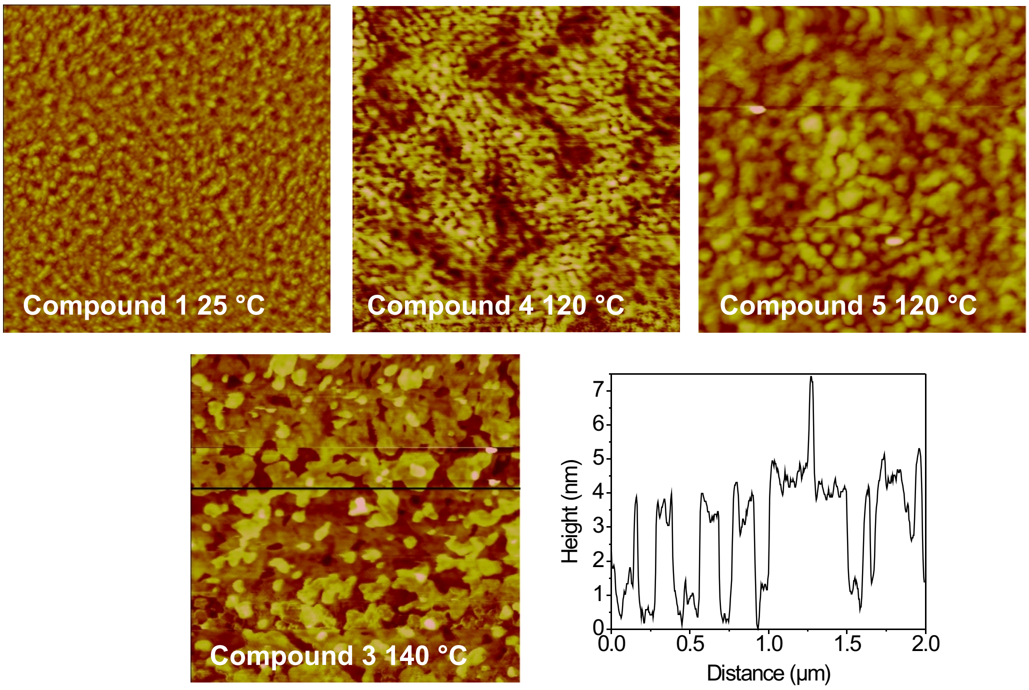

Figure 5.9: AFM images (2 x 2 μm^2) of compounds **1** and **3-5**. The substrate temperature during the deposition, indicated in each image, is the deposition temperature for which the largest FET mobility was obtained. The line scan is extracted from the AFM image of compound **3** at the position indicated by the black line.

5.2.2 Electrical characterization of the FETs

FETs based on all five compounds were manufactured using the device structure shown in Figure 5.10. All transistors show exclusively n-channel characteristics and can be operated in air (Figure 5.11). The key device parameters are summarized in Table 5.1 (For details on the sample preparation as well as the electrical measurements see Appendix C). The best performance was

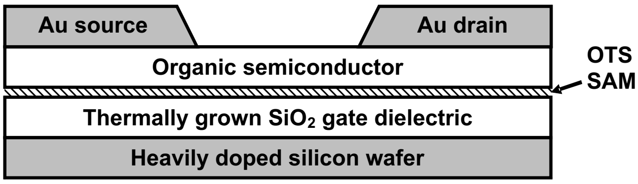

Figure 5.10: Cross section of the organic FETs.

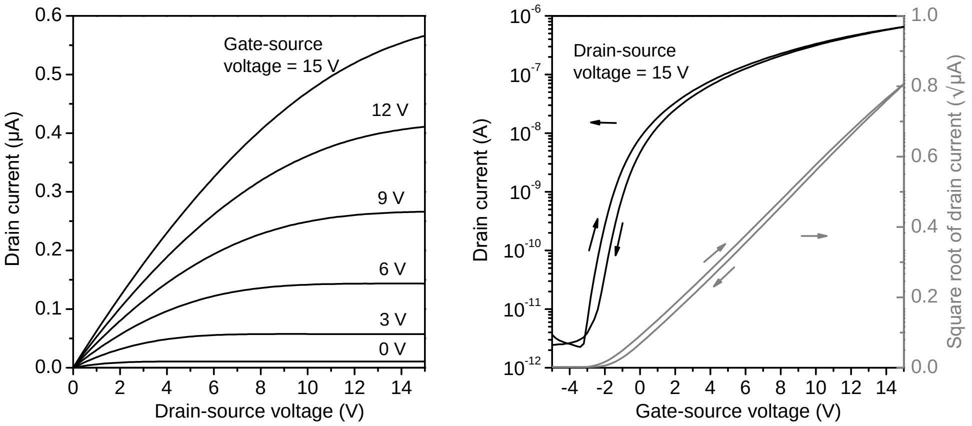

Figure 5.11: Output **(a)** and transfer **(b)** characteristics of a transistor based on compound **2** deposited at a substrate temperature of 120 °C, from which a carrier mobility of 0.1 cm^2/Vs and a subthreshold swing of 0.5 V/decade can be extracted.

obtained with compound **2** deposited at a substrate temperature of 120 °C. This transistor has a carrier mobility of 0.1 cm^2/Vs, a threshold voltage of 1 V, a subthreshold swing of 0.5 V/decade, and an on/off current ratio of 10^5. This mobility is lower than the value reported by Jones et al. for the same compound, but this may be related to the lower operating voltage used in the present experiments (15 V, instead of 100 V) and the different surface functionalization (OTS instead of HMDS). There is very little hysteresis in the transfer characteristics (Figure 5.11), and the subthreshold swing of 0.5 V/decade is quite good for an organic FET. The carrier mobility found in the FETs based on compound **2** increases almost monotonically over four orders of magnitude as the substrate temperature during the deposition is increased from 25 °C to 120 °C (Figure 5.15a). This agrees well with the AFM (Figures 5.3 and 5.5) and XRD (Figure 5.6) data which suggest an increasing degree of molecular order with increasing substrate temperature. FETs prepared at a substrate temperature of 140 °C, however, have a much smaller drain current than FETs prepared at 120 °C, even though the XRD (Figure 5.6) data clearly show a higher degree of molecular order. The reason for the reduced drain current at 140 °C is that the material partially dewets the surface, so that the film is not completely closed at 140 °C. As a result, the FET transconductance has a maximum for a substrate temperature of 120 °C .

compound	**T_{sub}**	**carrier mobility**	**threshold voltage**	**on/off ratio**
1	25 °C	$4 \cdot 10^{-6}$ cm^2/Vs	~ 0 V	$< 10^1$
	> 60 °C	no field effect		
2	100 °C	0.06 cm^2/Vs	-2 V	10^5
	120 °C	**0.1 cm^2/Vs**	**-1 V**	**10^5**
	140 °C	0.009 cm^2/Vs	-1 V	10^5
3	120 °C	$3 \cdot 10^{-4}$ cm^2/Vs	-3 V	10^3
	140 °C	**0.05 cm^2/Vs**	**-1 V**	**10^5**
	160 °C	0.04 cm^2/Vs	1 V	10^5
4	**120 °C**	**0.004 cm^2/Vs**	**-32 V**	**10^4**
	140 °C	0.003 cm^2/Vs	-24 V	10^4
5	100 °C	$7 \cdot 10^{-6}$ cm^2/Vs	~ 0 V	10^1
	120 °C	**0.002 cm^2/Vs**	**-14 V**	**10^4**
	140 °C	no field effect		

Table 5.1: Summary of the electrical characteristics of organic thin-film transistors fabricated using compounds **1** through **5**. T_{sub} denotes the temperature of the substrate during the vacuum deposition of the organic semiconductor. The optimum deposition temperature for each compound is indicated in bold face.

FETs based on compounds 1 and 3-5

For FETs based on compound **1** the performance (Table 5.1) peaks at a much lower substrate temperature (25 °C), apparently because the short substituents lead to distinct island growth at temperatures as low as 60 °C . However, at a substrate temperature of 25 °C the degree of molecular order in the film is very small, which explains the poor mobility (4×10^{-6} cm^2/Vs, similar to the mobility of compound **2** at this substrate temperature). Compound **3** has a longer substituent than compound **2**, and consequently the transistor performance peaks at a higher substrate temperature (140 °C). FETs based on compound **3** prepared at 140 °C have relatively good performance (threshold voltage 1 V, subthreshold swing 1.2 V/decade, on/off ratio 10^5, small hysteresis), although the mobility is only half the maximum mobility of compound **2** (0.05 cm^2/Vs, Figure 5.12 and Table 5.1).

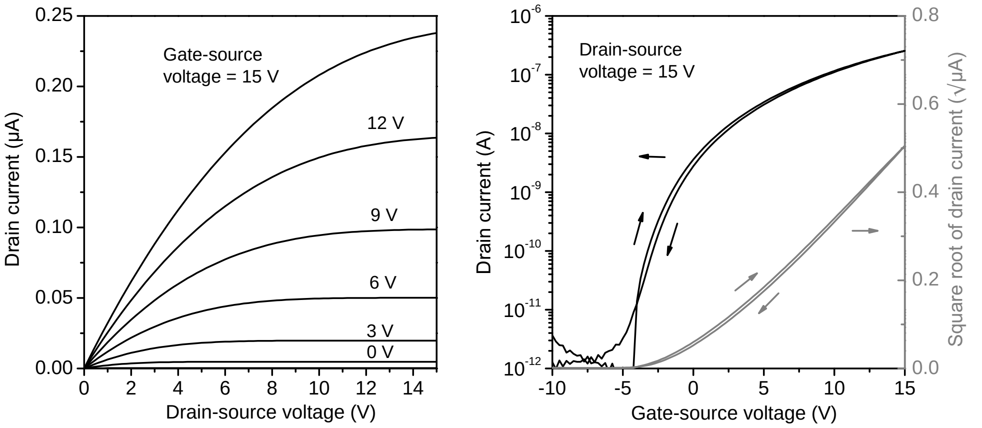

Figure 5.12: **(a)** Output and **(b)** transfer characteristics of an FET based on compound **3** deposited at a substrate temperature of 140 °C, from which a carrier mobility of 0.05 cm^2/Vs can be extracted.

The two compounds with cyclic endgroups display a maximum mobility of 0.004 cm^2/Vs (compound **4**) and 0.002 cm^2/Vs (compound **5**) respectively, both for a substrate temperature of 120 °C (Table 5.1, Figures 5.13 and 5.14). The reason for the much lower mobilities in these two compounds is unclear, but it is interesting that the FETs based on compounds **4** and **5** also show a much more negative threshold voltage than the FETs based on the compounds with linear endgroups. This difference suggests that the bulkier cyclic endgroups lead to a different crystal packing that is characterized both by a smaller degree of orbital overlap in the direction of transport in the channel (leading to a poor mobility) and by a greater density of defects (leading to a larger threshold voltage). However, this interpretation is challenged by the recent results of Chen and coworkers [142] who have observed mobilities as large as 0.06 cm^2/Vs for FETs based on perylene carboxylic diimides end-functionalized with bulky fluorine-rich cyclic endgroups. On the other hand, their compounds were not core-cyanated, so a direct comparison is difficult.

5.2.3 Shelf life of the FETs

The shelf life of the FETs prepared from compounds **2** through **5** when stored under ambient conditions was investigated. Interestingly, all devices

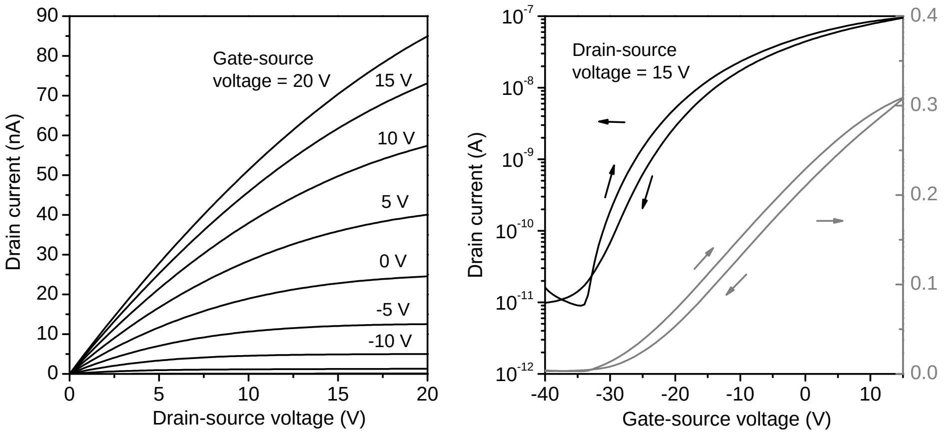

Figure 5.13: **(a)** Output and **(b)** transfer characteristics of an FET based on compound **4** deposited at a substrate temperature of 120 °C, from which a carrier mobility of 0.004 cm^2/Vs can be extracted.

show about the same rate of mobility degradation in air (Figure 5.15b and 5.15c). This observation is somewhat surprising, since the molecules have different functional groups and the degree of order and the molecular orientation of both the functional groups as well as the perylene core in the films is expected to be quite different: For example, films of compound **2** prepared at 120 °C and compound **3** prepared at 140 °C are both characterized by a high degree of molecular order. In contrast, compound **2** prepared at 80 °C and compounds **4** and **5** prepared at 120 °C appear much less ordered. Furthermore, in films of compound **2** prepared at 120 °C the molecules are oriented mainly with their long axis parallel to the substrate surface (polymorph A), so that the conjugated core of the molecule is exposed to the ambient and the film is therefore not protected from the ambient by the fluoroalkyl chains.

In contrast, in films of compound **3** prepared at 140 °C the molecules stand with their long axis approximately upright on the substrate surface. Finally, the fluorinated functional groups vary in length and bulkiness (fluorinated alkyl chain of different length in compounds **1** through **3**, cyclic substitutes in compounds **4** and **5**), and thus the packing of the functional groups is expected to vary. Yet, all FETs show about the same rate of degradation.

In order to rule out that the degradation of the mobility is caused by a macroscopic rearrangement of the organic molecules, we have performed AFM measurements of the films before and during the degradation investigations and

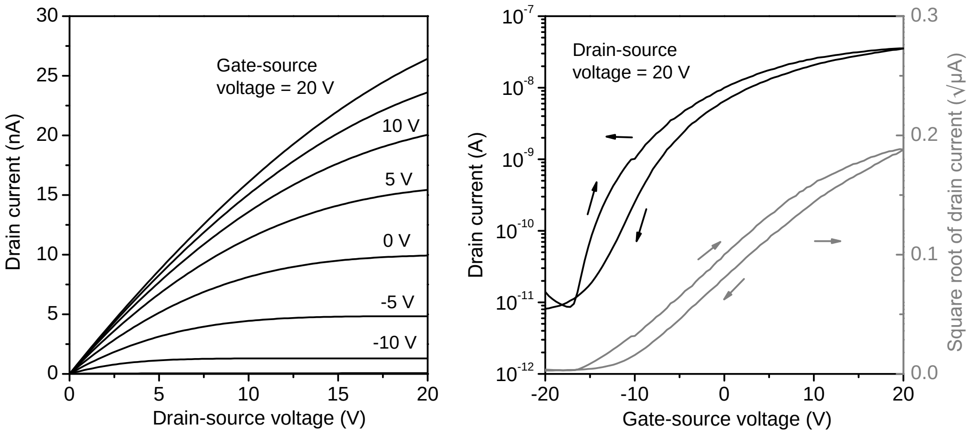

Figure 5.14: **(a)** Output and **(b)** transfer characteristics of an FET based on compound **5** deposited at a substrate temperature of 120 °C, from which a carrier mobility of 0.002 cm^2/Vs can be extracted.

found no apparent change in the film morphology. We also note that the rate of mobility degradation is independent of the number of polymorphs in the film. Specifically, the FET in which the film is composed of two polymorphs (compound **2** deposited at a substrate temperature of 140 °C) shows the same rate of mobility degradation as the FETs in which the films are composed of only one polymorph (all other FETs).

The observation that compounds **2-5** show the same rate of mobility degradation when stored under ambient conditions contradicts the hypothesis that densely packed fluorinated substituents form a kinetic barrier against the undesirable diffusion of environmental species (such as oxygen) into the semiconductor film [153]. If this hypothesis were correct, one would expect the films of compound **3** prepared at 140 °C to be more stable than the others, because in films of compound **3** the molecules stand with their long axis upright on the substrate, so that the long and fluorine-rich $CH_2(CF_2)_6CF_3$ substituents are pointing towards the air. In contrast, FETs composed of compound **2** prepared at 120 °C should be less stable, since in these films (in particular polymorph A) the fluoroalkyl chains do not protect the perylene cores from ambient species.

Furthermore, if the fluoroalkyl chains would form a kinetic barrier against penetration of ambient species, the degradation of the FETs should also depend on the surface area exposed to the ambient: The larger the surface

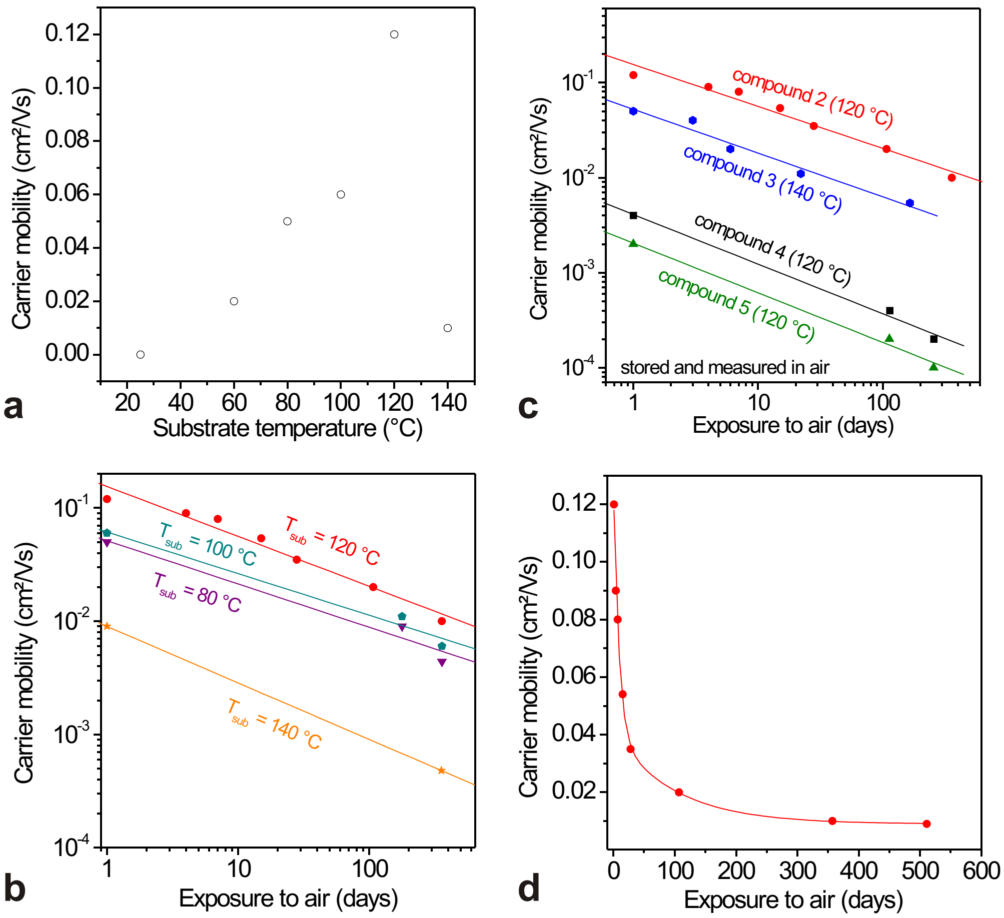

Figure 5.15: **(a)** Carrier mobilities of transistors based on compound **2** fabricated at different substrate temperatures. **(b)** Time-dependent degradation of the carrier mobility of FETs based on compound **2** deposited at different substrate temperatures. **(c)** Time-dependent degradation of the mobility of FETs based on compounds **2** through **5**, each deposited at the respective optimum substrate temperature. The rate of degradation of the carrier mobility is similar for all FETs. The solid lines in **(b)** and **(c)** are a guide to the eye. **(d)** Exponential fit to the degradation data measured for compound **2** deposited at a substrate temperature of 120 °C.

area, the larger the amount of ambient species able to penetrate into the film, and the faster the film would be expected to degrade. In addition to the surface area, the density of grain boundaries would then also be expected to influence the air stability of the FETs, since grain boundaries are likely to enhance the diffusion of environmental traps into the film.

In the FETs presented here, however, neither an influence of the density of grain boundaries nor an effect of the surface area on the rate of mobility degradation could be detected: In films of compounds **2** and **3**, which show a high degree of molecular order, both the surface area and the density of grain boundaries are larger compared to the less ordered films of compounds **4** and **5**. Yet, the rate of mobility degradation in air is similar for all compounds. Finally, if the hypothesis that a kinetic barrier is responsible for the air stability of the mobility were true, [153, 139] different rates of mobility degradation would be expected depending on whether the film is continuous or not. However, in the experiments presented here, the same rate of mobility degradation was found for films with excellent surface coverage (compound **2** deposited at substrate temperatures of 80 °C to 120 °C, and all films of compounds **3-5**) and for films that are not continuous and partially dewet the surface (compound **2** deposited at a substrate temperature of 140 °C).
Another hypothesis is that the stability of charge carriers injected into the semiconductor film with respect to water and oxygen depends on the redox potential of the organic molecules. This hypothesis is based on observations on the stability of electron-conducting doped polymers [162]. Specifically, it has been hypothesized that FETs based on compounds with a redox potential smaller than that of oxygen can be operated in air only if the molecules are protected from oxygen by a kinetic barrier formed by densely packed fluorine-rich substituents. Jones et al. have reported that based on its redox potential compound **2** would not be expected to be stable in air (unless the molecules are protected from oxygen) [153]. However, as was presented above, the FETs measured in this thesis can be operated in air independent of the possible presence of a kinetic barrier, since in this thesis, the same rate of degradation was observed for all compounds, regardless of the degree of molecular order and molecular orientation. Therefore, a mechanism unrelated to both the redox potential and the presence of a kinetic barrier appears to be responsible for the air stability of the n-channel organic semiconductors investigated in this work.

In order to gain further insight into the degradation mechanism of the mobility the time evolution of the mobility was fitted to a decay law (Figure 5.15d). The degradation of the mobility in air over time is expected to follow an exponential law: $\mu(t) = \mu_0 e^{-t/\tau}$. However, when the mobility decay of compound **2** deposited at a substrate temperature of 120 °C (for which the most data points were collected) is fit to the equation $\mu(t) = \mu_0 e^{-t/\tau}$, the quality of the fit is not satisfactory ($\chi^2 = 3 \times 10^5$). Better agreement between data and model ($\chi^2 = 1 \times 10^5$) is achieved by assuming two consecutive degradation processes with different decay rates [163]: $\mu(t) = \mu_1 e^{-t/\tau_1} + \mu_2 e^{-t/\tau_2} + C$. The fit yields $\tau_1 = 9$ days, $\tau_2 = 100$ days, $\mu_1 = 0.09$ cm^2/Vs, $\mu_2 = 0.03$ cm^2/Vs,

$C = 0.009$ cm^2/Vs. A possible explanation for the observation of two consecutive degradation processes is a decay process that proceeds from an initial state via an intermediate state to a final state. The future elucidation of the detailed physical or chemical mechanisms underlying this two-step decay process may provide further insight into the degradation processes of organic semiconductors in general.

5.3 FETs based on perylene diimide nanoribbons

In the previous section, vacuum evaporation was used in order to deposit the organic thin films. One of the advantages of this technique is that large substrates can be reproducibly coated with amorphous or polycrystalline layers of organic semiconductors. However, the inevitable presence of disorder in the film introduced by the grain boundaries limits the mobility of FETs fabricated by this technique [164]. For the fabrication of FETs that possess a larger mobility it is desirable to build transistors based on single organic crystals [165].

One method of fabricating single organic crystals is physical vapor transport. Here, the organic semiconductor is sublimed in a tube furnace by resistive heating. A gas flux carries the molecules to a colder zone in the oven where the material precipitates and forms crystals [166].

The shape of the crystals obtained depends on the ability of the molecules to π-stack: Molecules that are characterized by weak π-interactions in their crystalline form tend to form three-dimensional (3D) crystals [167]. A typical example is pentacene from which high-quality 3D-crystals can be grown from the gas phase [165]. In contrast, in molecules that assemble through strong $\pi - \pi$-interactions crystal growth is highly anisotropic which leads to the growth of one-dimensional (1D) structures. Such strong intermolecular coupling via $\pi - \pi$ interactions is believed to facilitate large charge carrier mobility which is why the use of such materials is desirable for application in FETs. One example of how the large $\pi - \pi$ overlap between the molecules can lead to the formation of highly anisotropic crystal growth is copper phthalocyanine (CuPc), from which single-crystalline submicrometer-sized ribbons could be fabricated by physical vapor transport [168]. Field effect mobilities of 1 cm^2/Vs were reported in p-channel FETs based on these CuPc ribbons. The larger mobility compared to thin CuPc films (here mobilities usually are 0.02 cm^2/Vs) was attributed to the higher degree of crystallinity of the ribbons compared to that of the thin films [168].

Recently, an alternative method for the fabrication of highly crystalline wires with diameters of hundreds of nanometers has attracted significant attention. This method relies on the crystallization of an organic compound from a supersaturated solution of the molecule. A very simple way to attain this supersaturation is to dissolve an organic molecule in a relatively poor solvent by heating the solution [167, 169]. Upon slow cooling, crystallites of the organic molecule begin to form. The formation of crystalline wires has also been shown to proceed at the receding contact line of a drying drop containing the molecule [170, 171], or by the slow diffusion of a poor solvent into a good solvent, whereas the molecule is dissolved in the "good" solvent [172, 173, 174, 175].

5.3.1 Nanoribbons based on compound 2

Here, the latter method has been used for the fabrication of nanoscopic ribbons with a thickness of down to 50 nm from compound **2**, which involves interdiffusion of a poor solvent with a good solvent in which the organic molecule of interest has been dissolved. Following the procedure by Briseno et al.[174] a saturated chloroform solution of compound **2** ($\sim$ 1.5 mg/mL) was injected to the bottom of a beaker filled with methanol, in which compound **2** is not soluble (Figure 5.16). The nanoribbons formed within a few hours by the interdiffusion of the two solvents. The ribbons were then drop-cast onto OTS-functionalized SiO_2-coated degenerately doped silicon wafers (details on the fabrication are given in Appendix C.4). Subsequently, 200 nm thick gold source and drain contacts were evaporated through a shadow mask.

Under an optical microscope two gold electrodes that are connected by an individual ribbon can be easily located (Figure 5.17). Typical ribbons were between 20 μm and more than 300 μm long, and between 1.5 and 20 μm wide. Thicknesses between 50 and 100 nm have been found (Figure 5.18). From Figure 5.18 the existence of two different types of nanoribbons can be discerned. They differ in the ratio between their respective height and width. While the ribbon shown in **(a)** (ribbon 1) has a ratio between its width and its height of 300, this ratio is only 17 in the ribbon shown in **(b)** (ribbon 2). Furthermore, in the surface of ribbon 1 numerous cracks are visible, while ribbon 2 seems to be continuous. These two observations might be an indication that the ribbons are composed of different morphologies. The existence of two polymorphic forms of compound **2** had already been

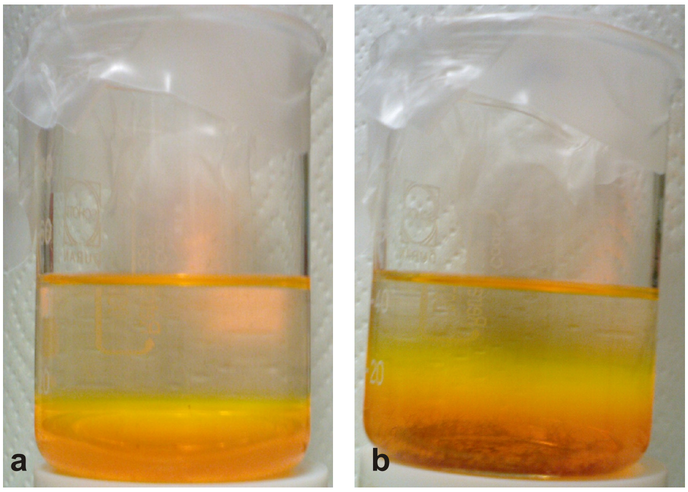

Figure 5.16: Two representative images of the self-assembly process of the organic ribbons based on compound **2**. **(a)** Beaker immediately after a solution containing compound **2** dissolved in chloroform ($CHCl_3$) was injected to the bottom of methanol (CH_3OH). A separation of the methanol and the chloroform can be discerned, since the interdiffusion of compound **2**, fluorescing in orange when dissolved in chloroform, and methanol has not started yet. **(b)** Image of the same beaker 3.25 hours later. The solvents have started interdiffusing, and ribbon started to crystallize and sink to the bottom of the beaker.

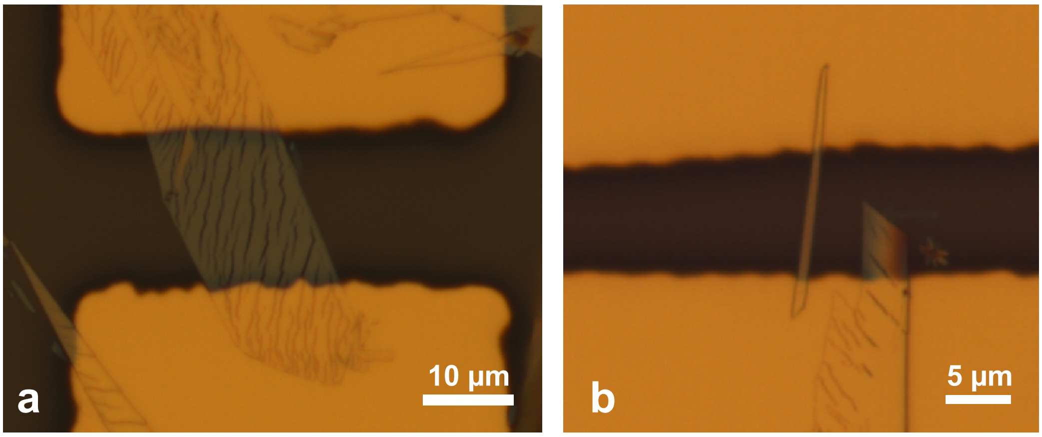

Figure 5.17: Optical micrographs of two nanoribbon FETs fabricated by solution self-assembly from compound **2**. The nanoribbons shown in **(a)** and **(b)** are of different morphology. 200 nm thick gold source and drain contacts were evaporated through a shadow mask.

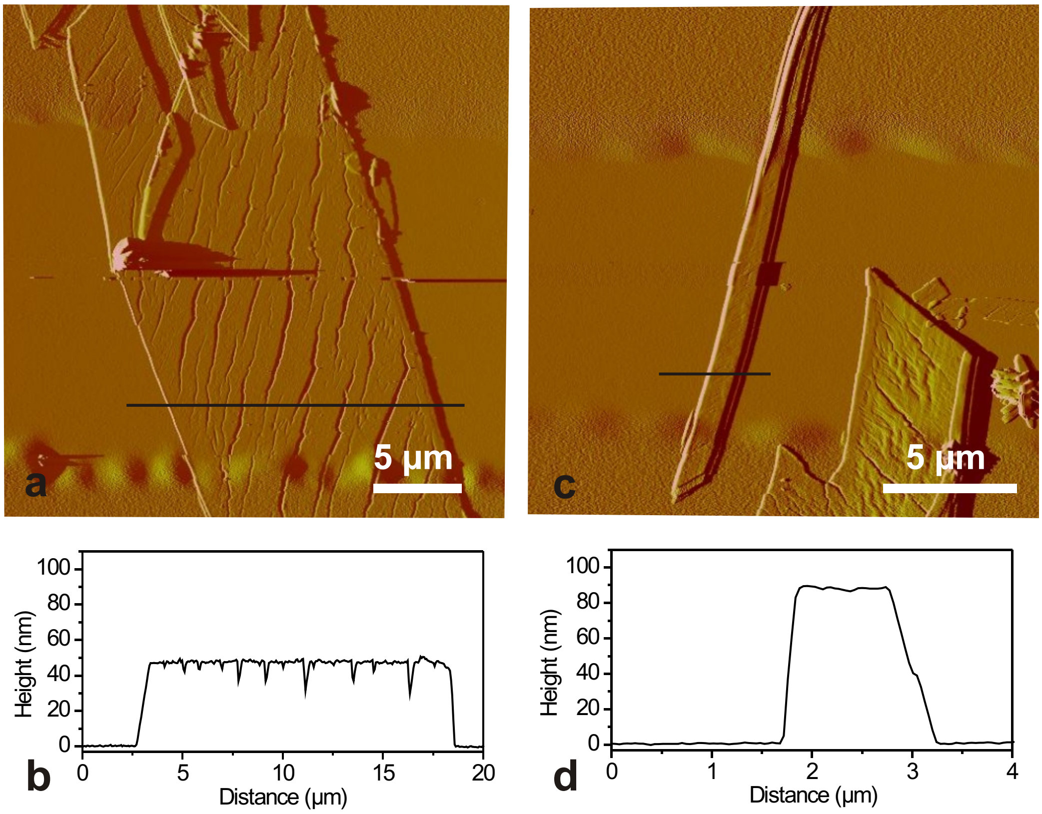

Figure 5.18: Atomic force microscopy (AFM) amplitude image of the two ribbons shown in Figure 5.17. The wires possess different aspect ratios: The wire shown in **(a)** is only 50 nm high, but 15 µm wide, as apparent from the lines can taken at the position marked by the black line and shown in **(b)**. In contrast, the wire shown in **(c)** is about 90 nm high, but less than 1.5 µm wide, as can be discerned from the lines can shown in **(d)**.

revealed for the thin films investigated in section 5.2.1. X-ray diffraction experiments are needed to shed further light on the crystal structure of the wires, and to clarify the hypothesis that ribbon 1 and 2 are composed of different polymorphs of compound **2**.

5.3.2 Electrical characteristics of nanoribbon FETs

The FETs shown in Figure 5.18 show excellent characteristics when measured under ambient conditions. The FET based on ribbon 1 shows a field effect mobility of 0.25 cm^2/Vs and an on-off ratio of the drain current $> 10^6$

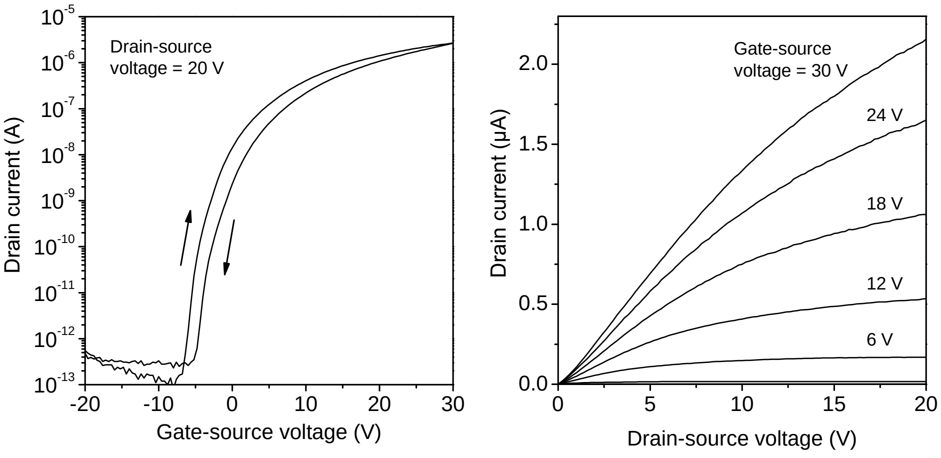

Figure 5.19: **(a)**Transfer and **(b)** output characteristics of the perylene diimide nanoribbon FET (compound **2**) shown in Figure 5.17a (ribbon 1).

(Figure 5.19). The transistor based on ribbon 2 shows a field effect mobility of 0.21 cm^2/Vs, while its smaller width limits the on-current to about 10^{-7} A which leads to an on-off ratio of 10^3 (Figure 5.20). Furthermore, both FETs show good saturation of the drain current in the output characteristics and a small hysteresis in the transfer curve.

It is interesting to note that the field effect mobility of the FETs based on solution-processed nanowires is about twice as large as the mobility of the vacuum-deposited films of compound **2**. This observation can be explained by the larger crystallinity of the nanowire transistors compared to the vacuum-deposited thin films. Thin films fabricated by vacuum deposition usually are either amorphous or polycrystalline, and therefore contain a large number of grain boundaries that act as scattering and/or trapping sites for charge carriers, thereby reducing the mobility of the FET [164]. In contrast, the solution-fabricated nanowires are usually single-crystalline [174] and thus possess significantly less grain boundaries, which in turn results in a larger field effect mobility.

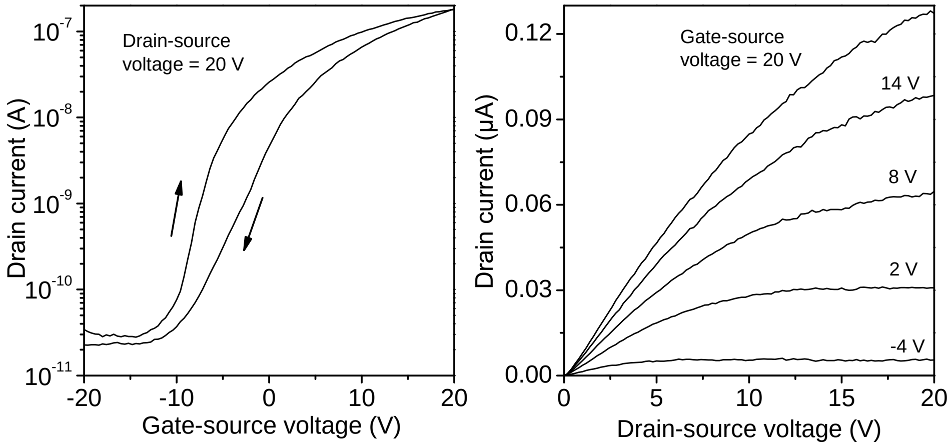

Figure 5.20: **(a)**Transfer and **(b)** output characteristics of the perylene diimide nanoribbon FET (compound **2**) shown in Figure 5.17b (ribbon 2).

5.3.3 Degradation of perylene diimide nanoribbon transistors

The shelf life of the FETs shown in Figure 5.18 was investigated when devices were stored under ambient conditions in the dark. They were measured occasionally and their mobility monitored over time. As apparent from Figure 5.21a, the mobility of ribbon 1 remains essentially constant over 35 days, whereas the mobility of ribbon 2 decreases by a factor of 2. The stability of the mobility does not depend on whether the FETs are stored under dark (first 31 days) or under ambient light (from day 31 on, hatched in Figure 5.21). In order to interpret the slight difference in the degradation of the mobility over time of the two wires, detailed crystallographic studies would be necessary in order to shed light on a possible difference in the respective microscopic arrangement of the molecules in the belts.

5.3.4 Comparison of the shelf life of thin film and nanoribbon FETs

It is interesting to compare the time evolution of the mobility of the organic FETs based on thin films of compound **2** as they were discussed in section 5.2 to that of the nanoribbon FETs. Even though the same semiconductor was used in both FETs, the stability of their carrier mobility is very different

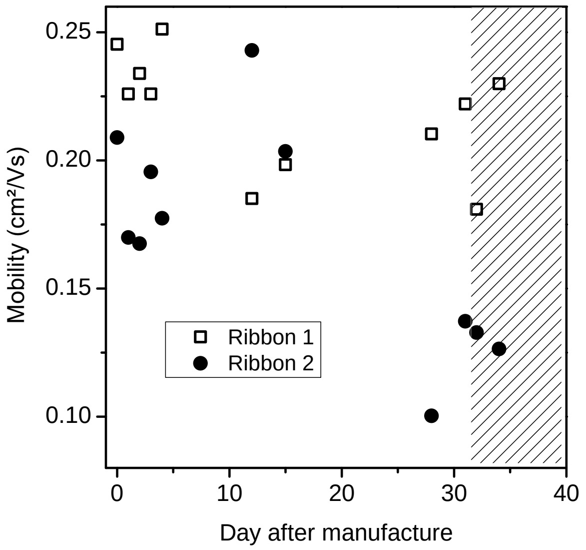

Figure 5.21: Time evolution of the mobility of the FET shown in Figure 5.19 (ribbon 1) compared with the FET shown in Figure 5.20 (ribbon 2). For the first 32 days the devices were protected from light, from then on there were kept under ambient light (hatched).

(Figure 5.22). While the mobility of the nanoribbon FET (ribbon 1) remains essentially constant over 35 days, the mobility of the thin film FETs based on compound **2** degrades by a factor of 10 within the first 10 days, after which it continues decreasing with a slower decay rate.
The excellent stability of the mobility in the nanoribbon FETs contradicts at first sight some of the conclusions reached in chapter 5.2, in which it was argued that in thin polycrystalline or amorphous films the rate of the degradation of the mobility in air does not depend on the amount of grain boundaries. However, in both the polycrystalline as well as in the amorphous films inevitably a significant number of grain boundaries is present. In comparison, in the highly crystalline nanoribbon we assume that no grain boundaries are present. In the thin films both in amorphous and in polycrystalline films a significant number of grain boundaries is present, however with different magnitude (more grain boundaries in the amorphous, less in the polycrystalline films). However, this different magnitude might not be significant enough to reflect upon the degradation of the mobility. In com-

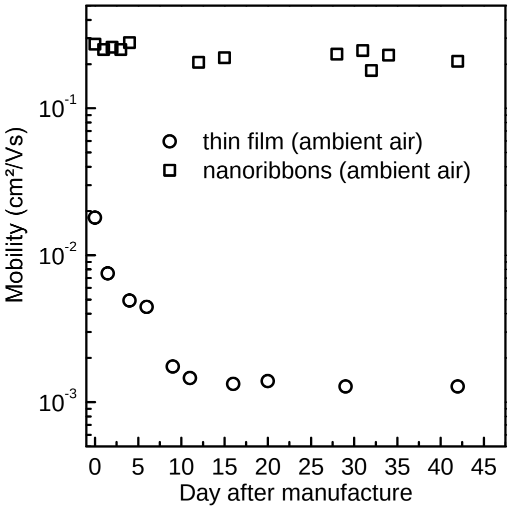

Figure 5.22: Time evolution of **(a)** the mobility of the FET shown in Figure 5.19 compared with a thin film FET fabricated by thermal evaporation of compound **2**. During the evaporation of the thin film the substrate was held at 120 °C.

parison, the absence of grain boundaries in the nanoribbon might be the reason for their better air stability. Alternatively, a different orientation of the molecules in the nanoribbon may be responsible for the enhanced stability. A tighter packing of the molecules might inhibit interdiffusion of environmental traps that could lead to a degradation of the film. However, a thorough crystallographic study would be necessary to clarify this discrepancy.

Chapter 6

Novel route to polymer nanofibers

In addition to the investigation of pre-fabricated nanoscale structures like SWCNTs, also new ways for the fabrication of nanoscale objects were investigated in this thesis. Using the well known spin-coating method, it was found that nanoscale fibers with a diameter down to 25 nm emerge from a polymer solution during this process. This procedure offers an attractive alternative to established methods of fabricating polymer nanowires like electrospinning, for the efficient, simple and nozzle-free fabrication of nanoscale fibers from a variety of polymer solutions. It could be further expanded to semiconducting polymers such as polythiophenes [176, 177] for the fabrication of nanowire transistors.

Up to now, polymer nanofibers have been mainly fabricated by electrospinning. It is one of the most established fiber fabrication methods which has attracted much attention due to the ease by which fibers with diameters ranging from 10 nm to 10 μm can be produced from natural or synthetic materials [178, 179, 180]. However, this method requires a DC voltage in the kV range, and high fiber production rates are difficult to achieve, because only a single fiber emerges from the nozzle of the pipette holding the polymer solution [181].
In this chapter, a simple, but efficient procedure enabling the parallel fabrication of a multitude of polymer fibers with regular morphology and diameters as small as 25 nm will be described [182]. The procedure involves the application of drops of a polymer solution onto a standard spin coater, followed by fast rotation of the chuck, without the need of a mechanical constriction. The fiber formation relies upon the instability of the spin-coated liquid film that arises due to a competition of the centrifugal force and the Laplace force

induced by the surface curvature. This Rayleigh-Taylor instability triggers the formation of thin liquid jets emerging from the outward-driven polymer solution, yielding solid nanofibers after evaporation of the solvent. In addition to being simple, the spinning procedure offers several technologically relevant advantages, including the absence of the need for a mechanical constriction and the ability to yield hollow polymer beads, and is applicable to different types of polymers.

6.1 Introduction of the spin-coating procedure

In order to gain a first insight into the basic processes responsible for the fiber generation during the spin-coating process, the formation of nanofibers made of poly-(methylmethacrylate) (PMMA), which can be regarded as a prototype system for other polymers, was studied in detail.

In the centrifugal spinning experiments, an aliquot of a PMMA polymer solution was placed in the middle of the chuck of a spin coater, which was then rotated at a speed of at least 3000 rotations per minute (rpm) for a

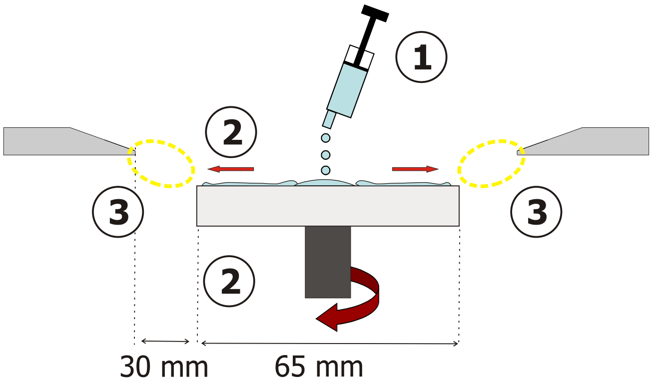

Figure 6.1: Schematic illustration of the spinning procedure used for the fabrication of polymer nanofibers. The steps are in detail: **(1)** The polymer solution is dripped from a syringe onto the center of a chuck. **(2)** Upon rotation, the polymer solution spreads across the chuck. **(3)** The nanofibers generated at the edge of the chuck can be collected during or after the spinning within the encircled area.

few seconds (Figure 6.1). After spinning, PMMA nanofibers were collected at the edge of the spin coater. Their diameter was determined by scanning electron microscopy (SEM) to be in the range of 25 nm to 5 µm, and fiber lengths of up to 0.5 mm were detected.

The liquid film created on the rotating chuck expands outward through the enacting centrifugal force in an asymmetric pattern, resulting in the formation of expanding edges and fingers of liquid. Such fingering instabilities are a common phenomenon occurring at the line of contact of a liquid that is forced to spread on a substrate due to external driving forces such as gravitational forces [183], capillary forces [184], centrifugal forces [185], and Marangoni forces (gradients in surface tension) [186, 187, 188]. The liquid flows preferentially through these fingers, causing them to grow relative to

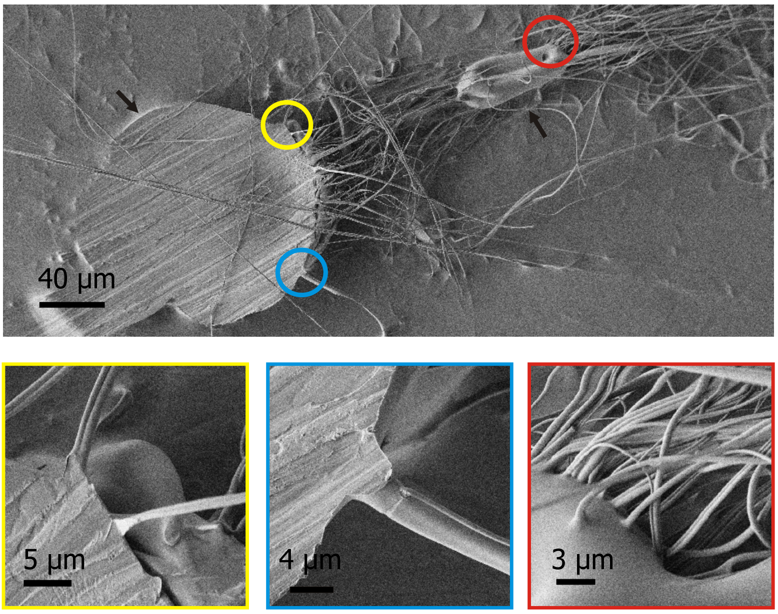

Figure 6.2: SEM images of the fiber formation. SEM image of a solidified polymer finger (lower left part) and a droplet that emerged from this finger (upper right part). The droplet is connected via numerous fibers to the finger. The formation of both the droplets and the nanofibers is caused by the Rayleigh-Taylor instability. Three regions have been inspected in closer detail. The first region (yellow) reveals a distance between two ejected fibers of approximately 7 µm. The second region (blue) shows a nanofiber emerging from a surface instability, while the region marked in red displays multiple fibers emerging from the same droplet. The distance between these fibers ranges between 1 and 5 µm.

other portions of the expanding pattern. A closer microscopic view of such a finger is presented in Figure 6.2; a scheme of the presumable formation of these fingers is shown in Figure 6.3. In this experiment, a 2 ml drop of a 5 wt% solution of 950 kg/mol PMMA was deposited onto the chuck which was then rotated at 8000 rpm for 30 sec. At the end of these fingers nanofibers can be observed (Figure 6.2).

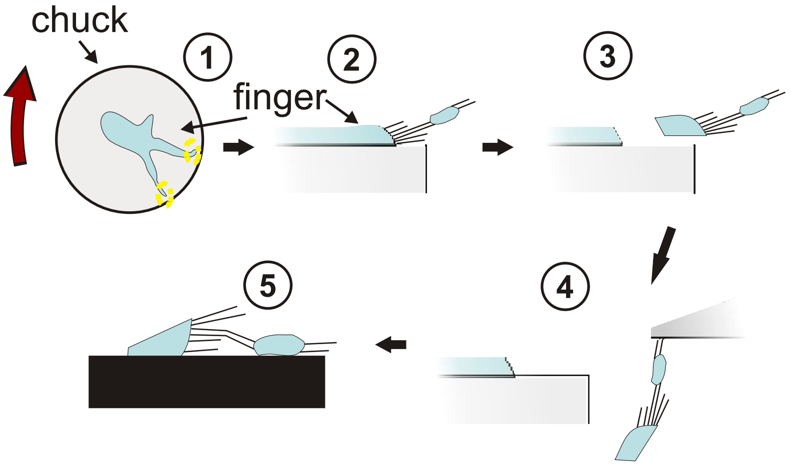

Figure 6.3: Schematic depiction of the presumed formation mechanism of fingers and fibers like those shown in 6.2. It involves the following five steps: *(1)* After deposition in the middle of the chuck, the PMMA solution extends outward upon spinning with concomitant formation of fingers. *(2)* At the finger ends, droplets and jets of polymer solution are ejected (marked in yellow). At a later stage, the tip of the finger breaks off *(3)*, followed by arrival of the fragment at the edge of the spin coater *(4)*, from where it is deposited onto a substrate *(5)* for further characterization.

6.2 Theoretical explanation of the observed fiber formation

The formation of the polymer fibers upon rotation of the chuck can be explained by a Rayleigh-Taylor instability at the air-liquid interface. Surface instabilities are well-known to be responsible for related phenomena, such as for example, droplet formation in the case of dripping of a liquid coating from a ceiling [189, 190, 191]. This dripping occurs since the interface between a liquid film and a gas layer can become unstable to infinitesimal vertical deformations, such that after a while, the liquid film turns into an array of drops. By formulating a rough balance between the destabilizing gravitational force per volume $\rho g \partial h/\partial x$ and the stabilizing surface tension force per volume $\gamma \partial^3 h/x^3$, the wavelength of the instability, i.e., the mean distance between the drops, can be estimated. One finds that the wavelength is controlled by the so-called capillary length $\kappa^{-1} = \sqrt{\gamma/(\rho g)}$ [189], where $\partial/\partial x \sim \kappa$. Here, g is the gravitational acceleration, ρ is the density of the liquid, and γ is the liquid-gas surface tension. The height of the liquid film hanging under the horizontal surface and the direction parallel to the ceiling are denoted as h and x, respectively.

The wavelength of the instability that occurs during the spinning of the polymer solution can be determined by an analogous balancing between the destabilizing centrifugal force $\rho\omega^2 R$ and the stabilizing surface tension force $\gamma\partial^3 h/\partial r^3$, where ω is the angular speed, $R = 0.0325$ m is the radius of the chuck, and r is the distance of the polymer solution from the center of the chuck in cylindrical coordinates. The characteristic length scale of the instability is then given by $L = (h\gamma/(\rho\omega^2 R))^{1/3}$, where $\partial/\partial \mathrm{r} \sim L^{-1}$. Using the parameters $\omega = 500\ \mathrm{s}^{-1}$, $\gamma = 0.01\ \mathrm{kg/s}^2$, $\rho = 10^3\ \mathrm{kg/m}^3$, and $h = 0.1\ \mu$m, one obtains $L = 4\ \mu$m for the characteristic length scale of the instability (i.e. the distance between two positions at which fibers are emitted from the droplet). This value is in good agreement with the mean distance between the points of ejection of the polymer fibers at the end of the fingers (Figure 6.2). The surface instabilities are the regions where liquid jets emerge due to the high radial speed $v = \omega R$.

6.3 Parameters affecting the fiber formation

The reason why the ejected jets of polymer solution do not further break up into individual droplets, but rather give rise to continuous, solid nanofibers (Figure 6.4), is the relatively high viscosity of the utilized PMMA solutions (of the order of several 10 mPa · s). Stretching of the fibers by the centrifugal force exerted onto the polymer and evaporation of the solvent molecules during the movement towards the collecting area is expected to cause thinning of the fibers. The interplay between the centrifugal force and the viscous prop-

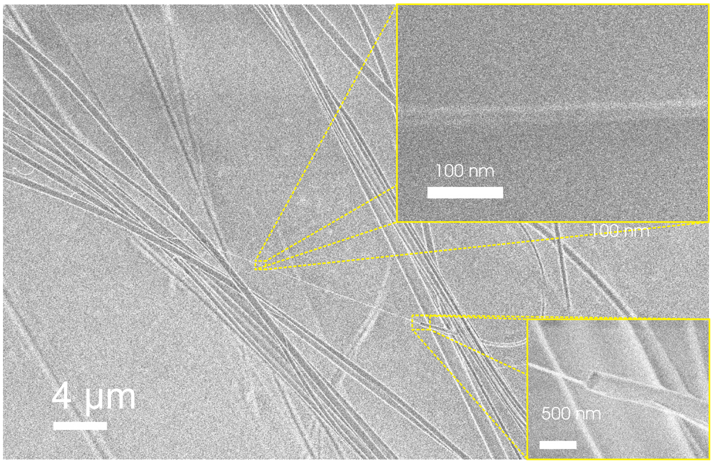

Figure 6.4: SEM image of PMMA nanofibers obtained from a 5 wt% chlorobenzene solution of 950 kg/mol PMMA subjected to a rotation speed of 3000 rpm. The diameter of the fiber shown in the upper inset is 25 nm. As apparent from the lower inset, the fibers are massive.

erties of the polymer solution is the reason that the spin-coating method is able to produce nanofibers, whereas conventional mechanical fiber spinning techniques, in which the diameter of the produced wires is defined by a mechanical constriction, yield fibers with diameters of at least a few tens of micrometers.

It is interesting to note that polymer nanofibers were obtained even when the formation of fingers was suppressed, either by depositing an increased amount of polymer solution on the chuck, or via deposition of the solution close to the edge of the chuck. In order to clarify the fiber formation mechanism in these cases, a silicon wafer substrate was fixed onto the chuck, and a drop of PMMA solution was placed close to the edge of the wafer. Scanning electron micrographs revealed that the resulting fibers originate from surface instabilities that occur when the polymer solution spreads across the wafer edge, as exemplified in the left panel of Figure 6.5. Further surface instabilities of the polymer film at the edge of the wafer are shown in the right panel of Figure 6.5 .

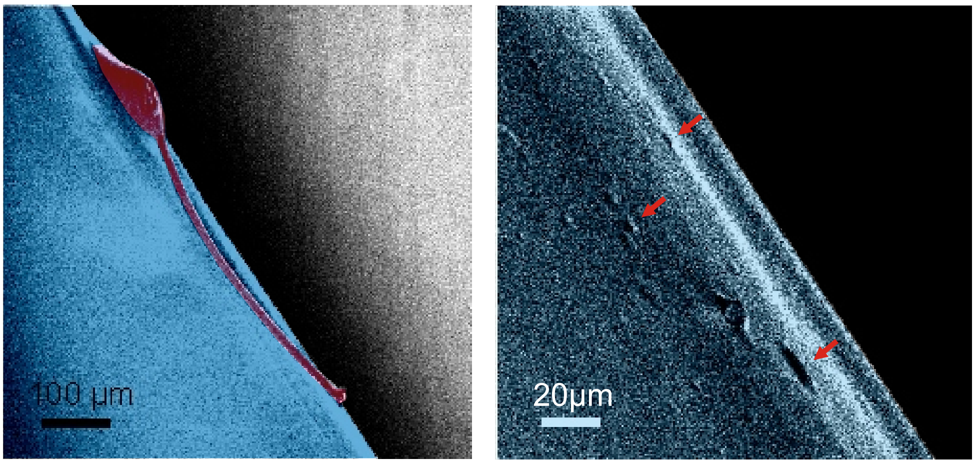

Figure 6.5: **(left panel)** SEM image of the edge of a spin-coated PMMA film prepared from of 5 wt% solution of 950 kg/mol PMMA on a silicon wafer (colored in blue) under conditions that avoid the fingering instability. The surface instability at the edge of the PMMA-coated silicon wafer from which a PMMA nanofiber emerges is highlighted in red. **(right panel)** SEM micrograph of a larger number of surface instabilities (three are marked by red arrows) on the edge of a PMMA film on a silicon wafer, with a separation on the order of several micrometers.

6.3.1 Influence of the concentration of the polymer solution and the molecular weight on the fiber formation

The fiber formation mechanism was further elucidated by investigating the influence of the concentration and molecular weight of the PMMA, as well as the spinning speed of the chuck. The data collected in Table 6.1 indicate under which conditions PMMA nanofibers could be observed. It is apparent that nanofiber formation requires that the polymer concentration exceeds the so-called entanglement concentration, which is about $3c^*$, where c^* is the overlap concentration. This finding corresponds well with a recent study on electrospinning of PMMA solution [192], and can be attributed to the fact that in both the electrospinning and the present spin-coating method, uniform fibers are difficult to obtain, due to the insufficient chain overlap when the polymer solution is too dilute.

molecular weight	concentration [wt%]	c/c*	η [mPa·s]	rpm range when fibers were observed
200kg/mol	3.5	1.6	4	-
	5.0	2.3	6	-
	7.0	3.2	11	8000 rpm (r_{min} = 35 nm)*
950kg/mol	1.5	2.0	6	-
	2.0	2.6	7	-
	2.5	3.3	13	8000 rpm (r_{min} = 45 nm)*
	5.0	6.6	57	3000 rpm (r_{min} = 25 nm)* - 8000 rpm (r_{min} = 50 nm)*

Table 6.1: Collection of the parameters used in the study of nanofiber formation as a function of molecular weight, concentration of the PMMA-chlorobenzene solution, and the rotation speed. The rotation speed was increased from 1000 to 8000 rotations per minute (rpm) in increments of 1000 rpm. The ratio c/c^* denotes the ratio of the actual concentration to the chain overlap concentration c^* of PMMA. The concentration of polymer solutions can be divided into three regimes: dilute ($c/c^* < 1$), semidilute unentangled ($1 < c/c^* < 3$), and semidilute entangled ($c/c^* > 3$). All polymer solutions were purchased from ALLRESIST GmbH, Strausberg, Germany. The last column indicates in which spin speed range nanofibers were observed. (*The minimum fiber diameter observed at the respective rotation speed is given in parenthesis).

6.3.2 Impact of the viscoelasticity of the polymer on the fiber formation

From Table 6.1, it can be seen that the minimum rotation speed needed for fiber formation increases with decreasing viscosity of the polymer solution. This dependency can be understood on the basis of the viscoelasticity of the PMMA solutions. Viscoelasticity is a property common to polymer solutions and accounts for the observation that both the viscosity and the elasticity of the polymer solution depend on the strength and time constant of external forces acting on the polymer chains. Specifically, if the time constant of the external force is small, the response of the polymer solution is elastic, whereas long time constants result in a viscous response of the polymer solution. Hence, for spinning of low-viscosity polymer solutions, fibers can be obtained, provided the rotation speed is large enough to increase the viscosity. In fact, it was found that for the 2.5 wt% solution of 950 kg/mol PMMA with a viscosity $\eta = 13$ mPa · s, fiber generation requires a minimum spinning speed of 8000 rpm, whereas in case of the 5 wt% solution of 950 kg/mol PMMA with viscosity $\eta = 57$ mPa · s, a speed of 3000 rpm is sufficient. Interestingly, no dependence of the minimum fiber diameter on either the concentration of the polymer solution or the molecular weight of the PMMA macromolecules was observed.

6.3.3 Influence of the vapor pressure of the solvent

The morphology of the PMMA fibers was found to sensitively depend on the vapor pressure of the solvent used. In particular, solvents with lower vapor pressure (e.g., ethylactate with a vapor pressure of 2 hPa at 20 °Cinstead of chlorobenzene with a vapor pressure of 21 hPa at 20 °C) results in quite thick (> 500 nm diameter) fibers that frequently coalesce and that are much more prone to breaking (see Figure 6.6). This difference most likely arises from the easier relaxation of the polymer chains to their non-stretched conformation within a solvent of lower vapor pressure, which ensures a slow drying of the fibers.

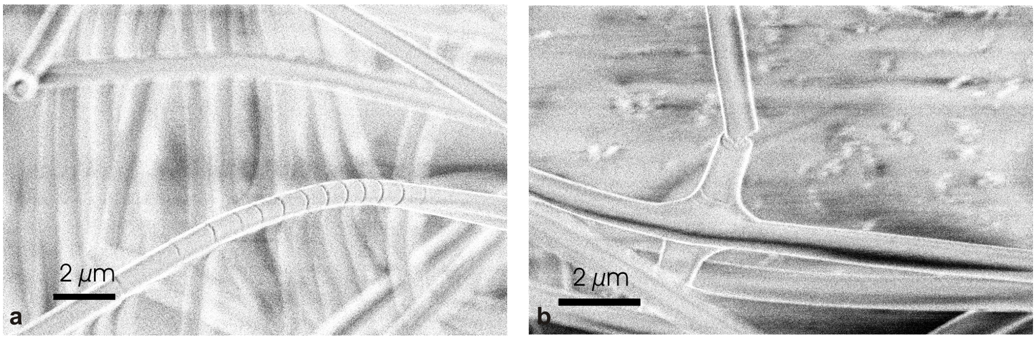

Figure 6.6: Polymer fibers observed by scanning electron microscopy (SEM) after spinning of a 4 wt% solution of 950 kg/mol PMMA in ethylactate at 8000 rpm. The vapor pressure of ethylactate is ten times lower than that of chlorobenzene (which is usually used in the spin-coating experiments). Due to the smaller vapor pressure, the fibers dry slower. The use of ethylactate as solvent leads to fibers that differ from those obtained with chlorobenzene in two aspects: First, they are very prone to breaking, as can be discerned from image **(a)**. Secondly, as shown in panel **(b)**, fibers readily coalesce due to the slower evaporation of the solvent.

6.4 Polymer beads as by-products of the spinning process

Under all investigated conditions, polymer beads were found as by-products of the spinning process. Examples of such toroidal and cup-like beads are shown in Figure 6.7. The formation of beads and beaded fibers is driven by surface tension and is another manifestation of the Rayleigh-Taylor instability. Surface tension acts to decrease the surface area per unit mass, by changing the jets into spheres. A driven jet of a low-molecular-weight liquid will form spherical droplets, while viscoelastic forces in polymer solutions resist rapid changes in shape, leading to beaded fibers (see e.g. Ref [193]). The reason behind this is that the coiled macromolecules of the dissolved polymer are transformed by the elongational flow of the jet into oriented, entangled networks that persist as the fiber solidifies. The contraction of the radius of the jet, which is driven by surface tension, causes the remaining solution to form beads. Contrary to electrospinning, in which only one fiber is connected to each bead, in the spinning process multiple fibers usually emerge from the beads (Figure 6.7). The bead diameter increases as the viscosity increases (Figure 6.8), as expected for the break-up of a liquid jet due to the Rayleigh-Taylor instability [194]. For example, the maximum droplet size observed

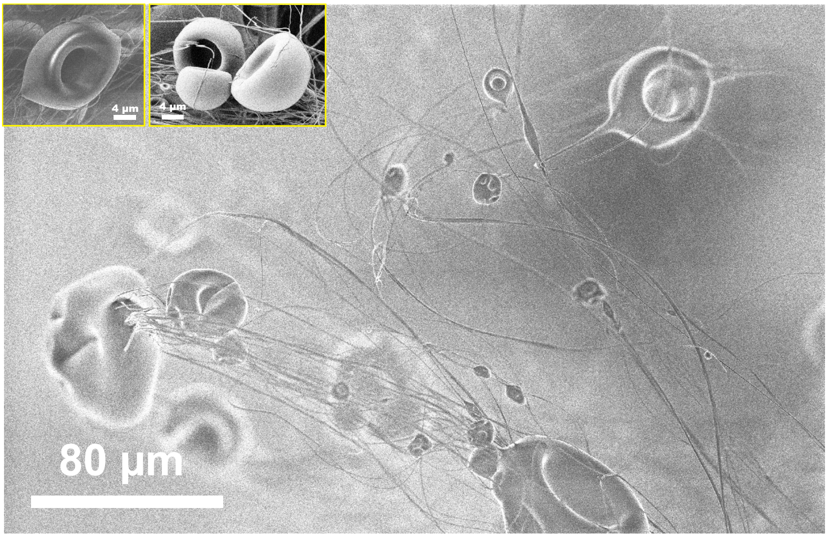

Figure 6.7: SEM image of nanofibers that connect polymer beads of various sizes, obtained by spinning of a 5 wt% chlorobenzene solution of 950 kg/mol PMMA at 3000 rpm. **Insets:** Magnified view of torodial and cup-like structures.

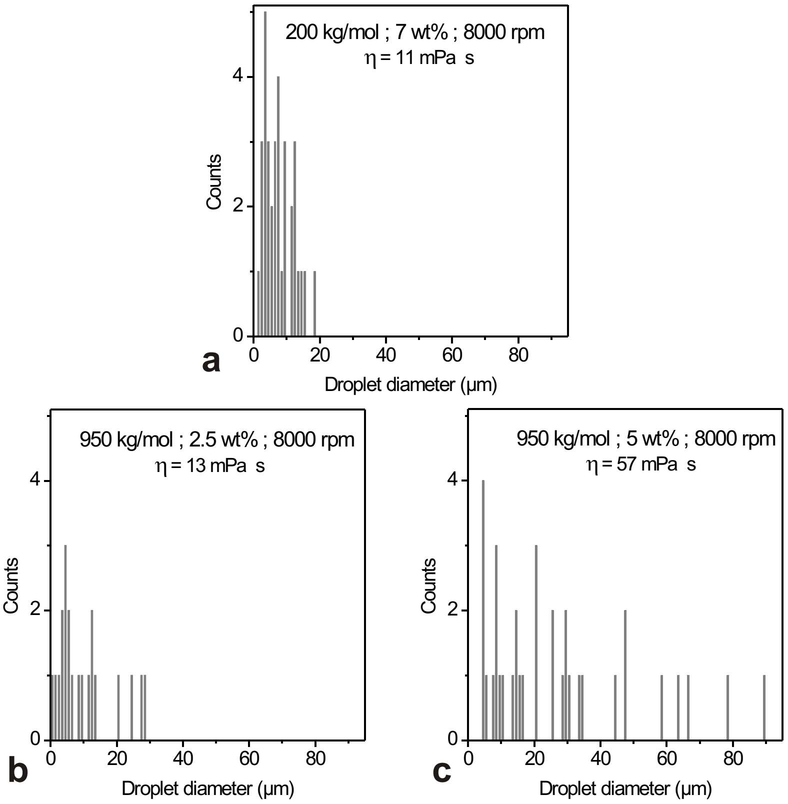

Figure 6.8: Statistics of the measured bead diameters in dependence of the viscosity of the polymer solution used for spin coating. With increasing viscosity from **(a)** to **(c)**, the average diameter of the beads increases, in agreement with the Rayleigh-Taylor instability that is responsible for the formation of the beads.

for a 5 wt% solution of 950 kg/mol PMMA with viscosity $\eta = 57$ mPa · s was determined to be 90 µm, whereas the maximum droplet size is below 30 µm when a 2.5 wt% solution of 950 kg/mol PMMA with viscosity $\eta = 13$ mPa · s is used. The obtained beads are potentially of interest for use in controlled drug release or as protective layers on fabrics [195, 196, 197].

6.5 Expansion of the approach to other polymers

As a first step towards expanding the application range of the spinning method, nanofibers and beads from a (methyl-methacrylate-methacrylic acid)-based copolymer, which is more hydrophilic compared to PMMA, were obtained. Examples of such fibers are depicted in Figure 6.9. By careful optimization of the relevant parameters, such as viscosity of the polymer solution, spinning speed, surface tension, and solvent evaporation rates, the method could be extended to further types of polymers, including materials not amenable to electrospinning.

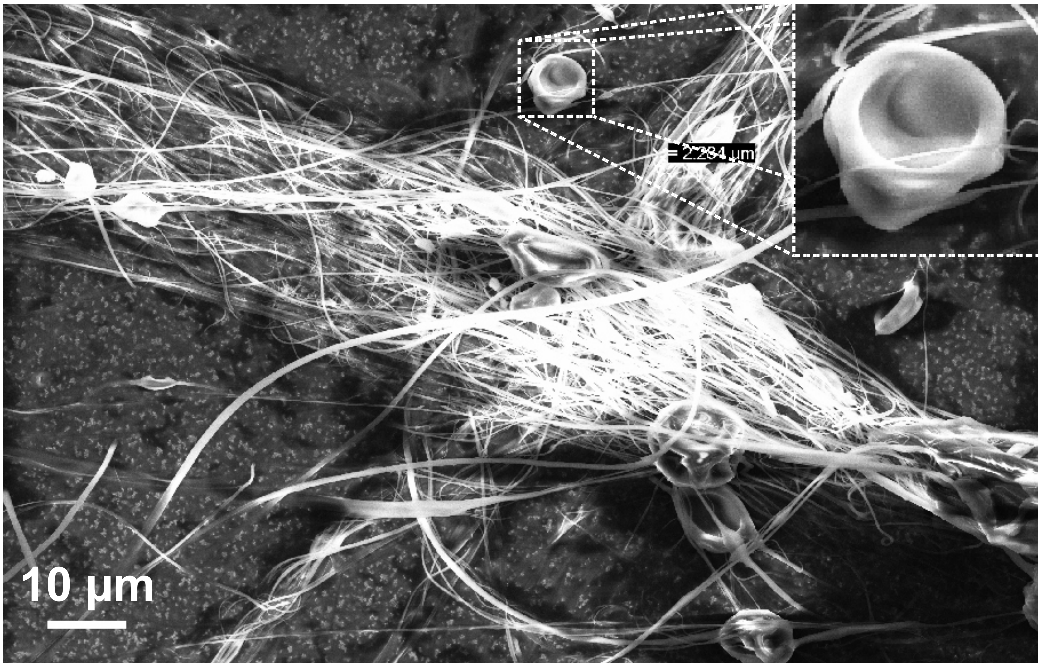

Figure 6.9: SEM image of nanofibers observed when a copolymer based on methyl-methacrylate and methacrylic-acid dissolved in 1-methoxy 2-propanol (8 wt%) is used for spin coating at a spinning speed of 8000 rpm. In the image nanofibers as well as droplets can be discerned. The droplets are not spherical but wrinkled, due to buckling of the thin elastic skin which has dried prior to the drying of the inner part of the droplet.

Chapter 7

Summary and outlook

The potential of organic nanostructured materials for application in field-effect transistors (FETs) was explored in this thesis. To this end, three different types of nanoscopic structures, namely single-walled carbon nanotubes (SWCNTs), core-cyanated perylene tetracarboxylic diimides and polymer nanofibers, have been studied as (potential) transistor channels.

In the first part of this thesis, high-performance FETs based on individual SWCNTs, with a 2 nm thick organic self-assembled monolayer (SAM) gate dielectric were assembled. While a silane-based SAM was used for the fabrication of global gate electrodes, structured aluminum gates were realized with the aid of phosphonic acid SAMs. Due to the high quality of both the SWCNTs and the SAM-based gate dielectric, the obtained FETs exhibit a unique combination of excellent device performance parameters. In particular, they operate with a gate-source voltage of only 1 V and show good saturation, large transconductance, an on/off ratio of 10^7, no hysteresis in the drain current, as well as a very low subthreshold swing (60 mV/dec, the room temperature limit of this parameter) under ambient conditions. It was demonstrated that the electrical performance of the FETs does not degrade when the devices are cycled 10^4 times between the on and off state, or when the devices are stored in air for more than seven months.

In future experiments, based on the outstanding electrical stability and high-performance of the SWCNT FETs investigated in this work, it would be interesting to explore the possibility of directed deposition of SWCNTs on patterned hydrophobic gate electrodes for the fabrication of larger integrated circuits, such as simple ring oscillators and amplifiers. Furthermore, since all of the manufacturing steps are performed at temperatures below 200 °C, the implementation of these devices on plastic substrates would be a major step toward the realization of low-power flexible electronics. For the implementation of such FETs based on an individual SWCNT, each nanotube has to be located by AFM and contacted by e-beam lithography. This serial fabrication process is a disadvantage for possible applications, since it is very time consuming. In industrial-scale processes, parallel manufacturing techniques such as photolithography are employed that allow for faster production. As a first step towards a parallel fabrication of SWCNT FETs on flexible substrates, networks of nanotubes could be used. Large substrates can be homogeneously covered with SWCNT-networks by solution-deposition or spray-techniques [198]. The fabrication of patterned metal gate and source/drain electrodes can then be performed with shadow-mask or photolithographic techniques. Since the deposited networks are composed of semiconducting as well as metallic SWCNTs, the metallic nanotubes would have to be eliminated by high current pulses [199], electrochemical techniques [90] or gas-phase reactions [200] prior to FET-operation. These devices might pave the road to the fabrication of large quantities of low-power high-performance FETs on flexible substrates.

Within this thesis, the modification of individual SWCNTs with an electrodeposited layer of Prussian Blue (PB) was investigated as a means of implementing new functionalities in SWCNT FETs. One intriguing finding was that PB-modified semiconducting SWCNTs exhibit a temperature-dependent doping characteristic, ranging from heavy p-type doping at room temperature to negligible doping at cryogenic temperatures. It was furthermore demonstrated that the coherent charge carrier transport through the SWCNT is not significantly affected by the deposition of PB. These findings represent a first step toward the future realization of spintronic devices that rely upon nanotube-molecular magnet hybrids. In particular, studies of the influence of PB on the electrical transport through the SWCNT at low temperatures and in magnetic fields would be of great interest. Theoretical studies have predicted novel features in the conductance through a very similar system, namely the coupling of a ferromagnet to a quantumwire.[98] These investigations revealed that due to the hybridization of electrons in the nanowire with spin-excitations of a ferromagnet that is coupled to the nanowire (these hybridized states are called magnetic polaron) a new band in the density of states would be formed. Since this band is separated from the band of scattering states, transport through the novel band is expected to be coherent. Another possible interesting application would be to study the so called magneto-Coulomb effect [201], which involves detection of the magnetization reversal of the organic magnet via a change of the Coulomb-blockade peaks of the quantum dot formed by the SWCNT between the contacts.

The second part of the thesis was dedicated to FETs based on small molecules. Here, five core-cyanated perylene tetracarboxylic diimides end-functionalized with fluorine-containing linear and cyclic substituents have been synthesized and employed in the fabrication of air-stable n-channel organic FETs with carrier mobilities up to 0.2 $\mathrm{cm}^2/\mathrm{Vs}$. The relationships between molecular structure, thin-film morphology, substrate temperature during vacuum deposition, transistor performance, and air-stability have been investigated. These experiments revealed that the previous understanding of air stability of n-channel FETs has to be reconsidered. In detail, it could be excluded that the substituents of the perylene carboxylic diimides form a kinetic barrier against the penetration of environmental species into the semiconductor in the case of the thin films. This finding demonstrates that the common model of the role of the redox potential of the organic compounds in determining the air-stability of the electron mobility has to be modified. Finally, the air stability of the electron mobility was compared in two different assemblies of the same compound, namely polycrystalline thin films and self-assembled nanobelts. The air-stability of the electron mobility in the thin films was found to be significantly lower than in the nanoribbons.

This pronounced dependence of the air stability of the mobility on the cystallinity of the semiconducting material might be the reason for the unclear picture of air stability of n-channel FETs in literature. The presented data show that a complete understanding of the air-stability of n-channel FETs can only be gained if the redox potential, the crystalline structure and the grain boundaries of the organic film are considered. This calls for further detailed investigations of the crystalline structure of both the polycrystalline thin films and the nanoribbons. Such investigations could clarify whether it is the crystalline structure or the presence of grain boundaries that renders the polycrystalline thin films more prone to aging than the nanoribbons.

For possible applications of organic FETs, it is very important to gain a detailed understanding of the processes underlying the degradation of mobility over time. A further step towards this would be the identification of the microscopic origin for the degradation. To this end, the stability of the charge carrier mobility in different gas atmospheres such as dry or wet nitrogen and dry or wet oxygen should be investigated. This would identify the possible role of different gaseous species in the degradation process. However, the degradation might also stem from a microscopic redistribution of the molecules (especially those at the grain boundaries) to a more thermodynamically stable configuration. This degradation mechanism seems very plausible, since the organic thin films are not grown in thermodynamic equilibrium. In contrast, the nanoribbons fabricated by solution self-assembly under thermal equilibrium conditions do not show a degradation of the mobility. Were the degradation of the thin films to be governed by a reorientation of the molecules, their $\pi - \pi$ overlap would correspondingly become weaker with time. This change could be detected by UV/VIS spectroscopic investigations [202].

While the nanoribbon FETs have a superior air-stability over the thin-film FETs, they are inferior compared to thin-film FETs in terms of ease of fabrication. This calls for an optimization of the approach used for the fabrication of such nanoribbon FETs. The nanoribbons used in this thesis were fabricated in solution and dispersed onto a substrate. Subsequently source/drain contacts were randomly deposited by thermal metal evaporation through a shadow mask. The yield of functioning FETs was therefore quite low. With the aim of optimizing the device-yield, it would be interesting to extend the solution-fabrication approach in such a way that highly-crystalline areas could be deposited onto the substrate at defined positions. Possible approaches are the directed deposition of nanoribbons by fluidic channels, or the use of such fluidic channels for the crystallization of the molecules from solution at defined positions.

Finally, the formation of nanoscale fibers with a diameter as small as 25 nm and toroidal polymer beads that emerge from a PMMA-based polymer solution during a standard spin-coating process was investigated. It could be attributed to the Raleigh-Taylor instability of the liquid film. It was found that a minimum viscosity of the polymer solution is necessary for the observation of nanoscale fibers. The spinning speed dependence of the occurrence of nanowires was explained by the increase of the viscosity of the polymer solution with the spin-speed (i.e. the viscoelasticity of the polymer solution). Moreover, first steps towards the applicability of this approach to different kinds of polymers were taken.

In the future, it would be interesting to extend the spin-coating process to semiconducting polymers in order to enable the fabrication of fiber-based nanoscale FETs. Since the charge carrier mobility of such FETs would strongly depend on the alignment of the polymer chains in the fibers, X-ray diffraction measurements could be employed to gain insight into the internal structure of the fibers. Furthermore, detailed theoretical and experimental work is needed to provide a better understanding of the role of the viscoelastic properties of the polymer solution on the fiber formation, as well as the dynamics of the fiber development during the spinning process. From an experimental point of view, monitoring of the spin-coating process with a high-speed camera would give a first insight into the involved dynamics. Furthermore, the nanowires might be interesting as scaffolds in soft-tissue engineering, since they mimic the nanoscale properties of native extracellular matrix [203]. To this end, materials that cannot be employed in electrospinning could be utilized.

Appendix A

Fabrication of SWCNT FETs

Deposition of HIPCO SWCNTs from solution

Carbon nanotubes (CNI, Houston, Texas) were dispersed by ultrasonic agitation in an aqueous surfactant solution (1 wt% sodium dodecyl sulfate) and then purified by centrifugation (11500 rpm for 30 min). The SAM-based substrates were immersed into this solution for about 10 min.

E-beam lithography

Source and drain contacts are fabricated on top of the SWCNTs (after locating them by AFM relative to alignment markers) by e-beam lithography using a standard double-layer (1*st* layer 3.5 % 200k; 2nd layer 1.5 %950k dissolved in chlorobenzene) polymethylmethacrylate (PMMA) resist with a total thickness of 200 nm, an electron energy of 20 keV (25 keV in case of the silane based SAM dielectric SWCNT FETs), and an electron beam dose of 270 μC/cm^2. Electrodes were formed through thermal evaporation of typically 0.3 nm Ti / 15 nm AuPd (60/40) and subsequent lift-off in acetone for 2h at 55 °C.

Appendix B

Electrochemical deposition of PB on SWCNTs

Electrodeposition of PB was performed with a Solartron 1285 potentiostat (working electrode: contacted tube, counter electrode: Pt wire, reference electrode: Ag/AgCl) using a freshly prepared aqueous solution of 5 mM HCl and 0.2 mM of each $FeCl_3$ and $K_3Fe(CN)_6$. After application of a constant current density of $\sim 3\,\mathrm{nA/cm^2}$ for 20 seconds, the samples were removed from the cell, thoroughly rinsed with 10 mM HCl and water, and finally dried under nitrogen flow.

Electroless PB deposition was accomplished through dipping the substrates for 15 min into a freshly prepared bath containing 5 mM HCl and 20 mM of each $FeCl_3$ and $K_3Fe(CN)_6$. For the control experiments, the substrates were dipped for 15 min into 5 or 10 mM HCl.

Appendix C

Synthesis and characterization of the perylene derivatives

C.1 Characterization and synthesis of the perylene derivatives, FET fabrication

LDI-TOF mass spectra were obtained in reflection mode on a Reflex IV (337 nm nitrogen laser) from Bruker Daltonik GmbH, Bremen, Germany. 1H NMR spectra were recorded on a Bruker Avance 300 MHz spectrometer. Chemical shifts are expressed in ppm relative to the internal standard Me_4Si ($\delta 0.00$). All reagents were purchased from Aldrich and ABCR and used as received. 1,7-dibromoperylene-3,4,9,10-tetracarboxydianhydride was obtained by bromination of perylene-3,4,9,10-tetracarboxydianhydride in concentrated sulphuric acid as described elsewhere [153]. Pentafluorobenzylamine was obtained by reduction of the corresponding benzonitrile according to the known procedure [204]. Compounds **1** through **5** were synthesized from 1,7 dibromoperylene-3,4,9,10-tetracarboxydianhydride in accordance to the same synthetic route as described for compound **2** [153] (Figure C.1). All compounds were purified via column flash chromatography on silica and characterized by ^{1}H NMR and LDI-TOF mass spectrometry. The NMR spectra showed the presence of small amounts of 1,6-isomers (1,6 dicyanoperylene) for all dicyano derivatives.

N,N‘-bis(2,2,2-trifluoroethyl)-1,7-dibromo-perylene-3,4:9,10-bis(dicarboximide) (1a). Red solid (62% yield), $R_f = 0.50$ (DCM:Acetone 100:1); ^{1}H NMR ($CDCl_3$) δ 9.523 (d, J = 8.14 Hz, 2H),

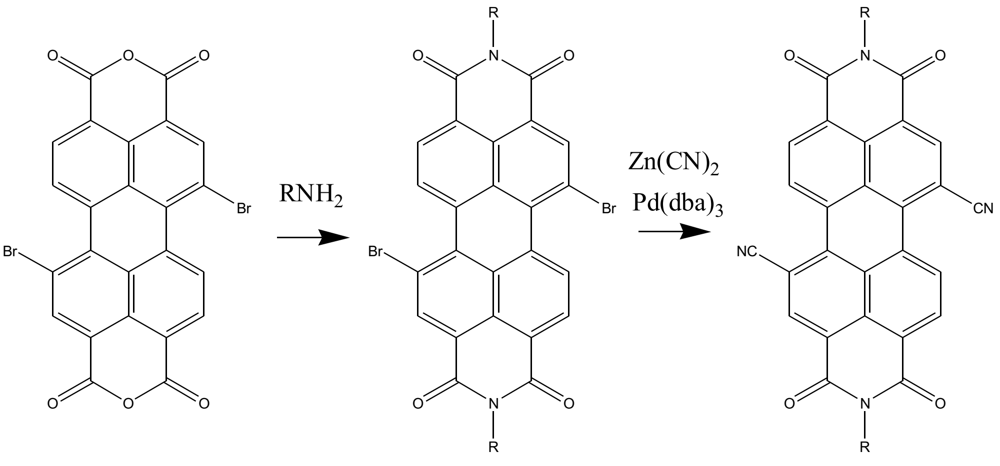

a

b

Figure C.1: Synthesis route for compounds **1-5**

8.984 (s, 2H), 8.75-8.80 (m, 2H), 4.95-5.10 (m, 4H); LDI-TOF MS calcd for $C_{28}H_{10}Br_2F_6N_2O_4$ (M^-) 709.89, found 709.72.

N,N‘-bis(2,2,2-trifluoroethyl)-1,7-dicyano-perylene -3,4:9,10-bis(dicarboximide) (1b). Red solid (71% yield), R_f = 0.28 (DCM:Acetone 100:2); ^{1}H NMR ($C_2D_2CL_4$) δ 9.02-9.05 (m, 2H), 8.26 (d, J=8.17 Hz, 2H), 8.20-8.29 (m, 2H), 4.25-4.31 (m, 4H); LDI-TOF MS calcd for $C_{30}H_{10}F_6N_4O_4$ (M^-) 604.06, found 603.87.

N,N‘-bis(1H,1H-perfluorobutyl)-1,7-dibromo-perylene -3,4:9,10-bis(dicarboximide) (2a). Red solid (82% yield), R_f = 0.67 (DCM:Acetone 100:2); ^{1}H NMR ($CDCl_3$) δ 9.506 (d, J = 8.16 Hz, 2H), 8.967 (s, 1H), 8.743 (d, J = 8.16 Hz, 2H), 5.017 (t, J = 15.36 Hz, 4H); LDI-TOF MS calcd for $C_{32}H_{10}Br_2F_{14}N_2O_4$ (M^-) 909.88, found 909.76.

N,N‘-bis(1H,1H-perfluorobutyl)-1,7-dicyano-perylene -3,4:9,10-bis(dicarboximide) (2b). Red solid (76% yield), R_f = 0.32 (DCM:Acetone 100:2); ^{1}H NMR ($CDCl_3$) δ 9.728 (d, J = 8.23 Hz, 2H), 8.87-9.07 (m, 3H), 5.028 (t, J = 15.21 Hz, 4H); LDI-TOF MS calcd for ($C_{34}H_{10}F_{14}N_4O_4$ (M^-) 804.05, found 804.22.

N,N‘-bis(1H,1H-perfluorooctyl)-1,7-dibromo-perylene

-3,4:9,10-bis(dicarboximide) (3a). Red solid (80% yield), $R_f = 0.56$ (DCM:Acetone 100:2); ^1H NMR ($CDCl_3$) δ 9.819 (d, J = 8.16 Hz, 2H), 8.948 (s, 1H), 8.750 (d, J = 8.16 Hz, 2H), 5.027 (t, J = 15.35 Hz, 4H); LDI-TOF MS calcd for $C_{40}H_{10}Br_2F_{30}N_2O_4$ (M^-) 1309.85, found 1309.73.

N,N'-bis(1H,1H-perfluorooctyl)-1,7-dicyano-perylene -3,4:9,10-bis(dicarboximide) (3b). Red solid (68% yield), $R_f = 0.25$ (DCM:Acetone 100:2); ^1H NMR ($CDCl_3$) δ 9.729 (d, J = 8.16 Hz, 2H), 9.032 (s, 1H), 8.986 (d, J = 8.16 Hz, 2H), 5.038 (t, J = 15.38 Hz, 4H); LDI-TOF MS calcd for $C_{42}H_{10}F_{30}N_4O_4$ (M^-) 1204.02, found 1203.91.

N,N'-bis(4-(trifluoromethyl)benzyl)-1,7-dibromo-perylene -3,4:9,10-bis(dicarboximide) (4a). Red solid (76% yield), $R_f = 0.41$ (DCM:Acetone 100:2); ^1H NMR ($CDCl_3$) δ 9.476 (d, J = 8.16 Hz, 2H), 8.936 (s, 2H), 8.714 (d, J = 8.16 Hz, 2H), 7.549-7.663 (m, 8H), 5.432 (s, 4H); LDI-TOF MS calcd for $C_{40}H_{18}Br_2F_6N_2O_4$ (M^-) 861.95, found 861.62.

N,N'-bis(4-(trifluoromethyl)benzyl)-1,7-dicyano-perylene -3,4:9,10-bis(dicarboximide) (4b). Red solid (43% yield), $R_f = 0.24$ (DCM:Acetone 100:2); ^1H NMR ($C_2D_2C_{14}$) δ 8.98 (d, J = 8.16 Hz, 2H), 8.25-8.36 (m, 4H), 6.95-7.01 (m, 8H), 4.78 (s, 4H); LDI-TOF MS calcd for $C_{42}H_{18}F_6N_4O_4$ (M^-) 756.12, found 755.98.

N,N'-bis(2,3,4,5,6-pentafluorobenzyl)-1,7-dibromo-perylene -3,4:9,10-bis(dicarboximide) (5a). Red solid (85% yield), $R_f = 0.83$ (DCM:Acetone 100:2); ^1H NMR ($CDCl_3$) δ 9.46-9.51 (m, 2H), 8.933 (dd, J = 4.78 Hz, 1.16 Hz, 2H), 8.68-8.73 (m, 2H), 5.468 (d, J = 26.37 Hz, 4H); LDI-TOF MS calcd for $C_{38}H_{10}Br_2F_{10}N_2O_4$ (M^-) 905.88, found 905.53.

N,N'-bis(2,3,4,5,6-pentafluorobenzyl)-1,7-dicyano-perylene -3,4:9,10-bis(dicarboximide) (5b). Red solid (88% yield), $R_f = 0.48$ (DCM:Acetone 100:2); ^1H NMR ($C_2D_2C_{14}$) δ 8.81-8.96 (m,2H), 8.21-8.33 (m,4H), 4.61-4.73 (m, 4H) LDI-TOF MS calcd for $C_{40}H_{10}F_{10}N_4O_4$ (M^-) 800.05, found 799.95.

C.2 Characterization of the thin films by XRD

Diffraction experiments The x ray diffraction measurements were carried out at the Max Planck Institute for Metals Research's beamline at the Synchrotron Radiation Source ANKA in Karlsruhe, Germany, at a beam energy of 10 keV ($\lambda = 1.23984$ Å). The GIXD experiment was performed with the angles of the incident and exit x ray beam close to the critical angle of the substrate $\alpha_{\text{crit}} = 0.1725°$. The fit of the x-ray specular data was performed with the Parratt32 software based on the Parratt algorithm.

C.3 FET preparation

Heavily boron-doped and thermally oxidized Si wafers were used as the substrate and gate electrode. The 100 nm thick SiO_2 gate oxide was functionalized with octadecyltrichlorosilane (OTS). The OTS self assembles from the vapor phase in a low pressure nitrogen atmosphere at a temperature of 150 °C, giving static contact angles between 100 and 105°. Organic semiconductors were evaporated at a rate of about 1 nm/min at a base pressure of about 10^{-6} mbar. During the deposition, the substrate was held at a constant temperature of 25, 60, 80, 100, 120, 140 or 160 °C. 30 nm thick gold source and drain contacts were evaporated through a shadow mask.

C.4 Electrical Measurements

All measurements were performed at room temperature in air on a Micromanipulator probe station with an Agilent 4156C Semiconductor Parameter Analyzer without specifically protecting the devices from the yellow laboratory light. Between electrical measurements devices were stored in ambient air under (weak) yellow laboratory light. The carrier mobility (μ) was calculated from the I_D vs. V_{GS} data in the saturation regime using the standard formula for field effect-transistors (Equation 2.21), where L is the channel length (130 μm), Z is the channel width (170 μm), C_{ox} is the gate dielectric capacitance (35 nF/cm^2), I_D is the drain current, and V_{GS} is the gate source voltage.

Bibliography

[1] R. P. Feynman. There is plenty of room at the bottom. *Engineering and Science*, 23:22–36, 1960.

[2] M. Knoll and E. Ruska. Das Elektronenmikroskop. *Z. Physik*, 78:318–339, 1932.

[3] G. Binning, H. Rohrer, C. Gerber, and E. Weibel. Tunneling through a controllable vacuum gap. *Applied Physics Letters*, 40:178–180, 1982.

[4] G. Binning, H. Rohrer, C. Gerber, and E. Weibel. Surface studies by scanning tunneling microscopy. *Physical Review Letters*, 49(1):57–61, 1982.

[5] R. Waser, editor. *Nanoelectronics and Information Technology.* Wiley-VCH, Weinheim, first edition, 2003.

[6] J.V. Barth, J. Weckesser, C.Z. Cai, P. Gunter, L. Burgi, O. Jeandupeux, and K. Kern. Building supramolecular nanostructures at surfaces by hydrogen bonding. *Angewandte Chemie - International Edition*, 39:1230–1234, 2000.

[7] H. Röder, E. Hahn, H. Brune, J.-P. Bucher, and K. Kern. Building one- and two-dimensional nanostructures by diffusion-controlled aggregation at surfaces. *Nature*, 366:141–143, 1993.

[8] J.V. Barth, G. Costantini, and K. Kern. Engineering atomic and molecular nanostructures at surfaces. *Nature*, 437:671–679, 2005.

[9] M. Pope and C.E. Swenberg. *Electronic Processes in Organic Crystals and Polymers.* Oxford Science Publications, Oxford, New York, second edition, 1999.

[10] A. Tsumura, H. Koezuka, and T. Ando. Macromolecular electronic device: Field-effect transistor with a polythiophene thin film. *Applied Physics Letters*, 49(18):1210–1212, 1986.

[11] G. Horowitz, D. Fichou, X. Peng, Z. Xu, and F. Garnier. A field-effect transistor based on conjugated alpha-sexithienyl. *Solid State Communications*, 72(4):381–384, 1989.

[12] H. Klauk. Personal communication.

[13] M. Kawasaki, S. Imazeki, S. Hirota, T. Arai, T. Shiba, M. Ando, Y. Natsume, T. Minakata, S. Uemura, and T. Kamata. High-mobility solution-processed organic thin-film transistor array for active-matrix color liquid-crystal displays. *Journal of the Society for Information Display*, 16:161–167, 2008.

[14] Z. Bao, A. Dodabalapur, and Lovinger A.J. Soluble and processable regioregular poly(3-hexylthiophene) for thin film field-effect transistor applications with high mobility. *Applied Physics Letters*, 69(26):4108–4110, 1996.

[15] H. Klauk, U. Zschieschang, J. Pflaum, and M. Halik. Ultralow-power organic complementary circuits. *Nature*, 445(7129):745–748, 2007.

[16] Francis Garnier, Ryad Hajlaoui, Abderrahim Yassar, and Pratima Srivastava. All-Polymer Field-Effect Transistor Realized by Printing Techniques. *Science*, 265(5179):1684–1686, 1994.

[17] S. Iijima. Helical microtubules of graphitic carbon. *Nature*, 354:56–58, 1991.

[18] T. Aßmus. *Carbon nanotubes functionalized with dye molecules and metal nanoparticles.* PhD thesis, École Polytechnique Fédérale De Lausanne, 2007.

[19] S. Reich, C. Thomsen, and J. Maultzsch. *Carbon Nanotubes - Basic Concepts and Physical Properties.* WILEY-VCH, Weinheim, first edition, 2004.

[20] R. Saito and G. Dresselhaus. *Physical Properties of Carbon Nanotubes.* Imperial College Press, London, first edition, 1998.

[21] R. Saito, M. Fujita, G. Dresselhaus, and M. S. Dresselhaus. Electronic structure of graphene tubules based on C60. *Phys. Rev. B*, 46(3):1804–1811, 1992.

[22] S. Datta. *Quantum Transport, Atom to Transistor.* Camebridge University Press, Cambridge, first edition, 2005.

[23] S. Frank, P. Poncharal, Z. L. Wang, and W. A. de Heer. Carbon Nanotube Quantum Resistors. *Science*, 280(5370):1744–1746, 1998.

[24] C. T. White and T. N. Todrov. Nanotubes go ballistic. *Nature*, 411:649–650, 2001.

[25] R. Farchioni and G. Grosso, editors. *Organic Electronic Materials.* Springer-Verlag, Berlin Heidelberg New York, first edition, 2001.

[26] N. Karl. Charge carrier transport in organic semiconductors. *Synthetic Metals*, 133-134:649–657, 2003.

[27] A. Maliakal, K. Raghavachari, H. Katz, E. Chandross, and T. Siegrist. Photochemical stability of pentacene and a substituted pentacene in solution and in thin films. *Chemistry of Materials*, 16(24):4980–4986, 2004.

[28] S.M. Sze and K.K. Ng. *Physics of semiconductor devices.* Wiley-Interscience, Hoboken, third edition, 2007.

[29] J. Bardeen and W.H. Brattain. The transistor, a semiconductor triode. *Phys. Rev.*, 74:230, 1948.

[30] W. Schockley. The theory of p-n junctions in semiconductors and p-n junction transistors. *Bell Syst. Tech. J.*, 28:435, 1949.

[31] D. Kahng and M.M. Atalla. IER-AIEE Solid-State Devices Res. Conf. In *Carnegie Inst. of Tech., Pittsburgh, PA*, 1960.

[32] S. Hunklinger. *Festkörperphysik.* Oldenburg, Oldenburg, first edition, 2007.

[33] A. Rolland, J. Richard, J. P. Kleider, and D. Mencaraglia. Electrical-properties of amorphous-silicon transistors and mis-devices - comparative-study of top nitride and bottom nitride configurations. *Journal of the Electrochemical Society*, 140(12):3679–3683, 1993.

[34] J.R. Brews. A Charge-Sheet Model of the MOSFET. *Solid-State Electron.*, 21:345–355, 1978.

[35] A. Javey, J. Guo, M. Paulsson, Q. Wang, D. Mann, M. Lundstrom, and H. J. Dai. High-field quasiballistic transport in short carbon nanotubes. *Physical Review Letters*, 92(10):106804, 2004.

[36] S. Heinze, J. Tersoff, R. Martel, V. Derycke, J. Appenzeller, and P. Avouris. Carbon nanotubes as schottky barrier transistors. *Phys. Rev. Lett.*, 89(10):106801, 2002.

[37] A. Rahman, J. Guo, S. Datta, and M.S. Lundstrom. Theory of ballistic nanotransistors. *IEEE Transactions on Electron Devices*, 50(9):1853–1864, 2003.

[38] P. Avouris, J. Appenzeller, R. Martel, and S. J. Wind. Carbon nanotube electronics. *Proceedings of the IEEE*, 91(11):1772–1784, 2003.

[39] A. Bachtold, P. Hadley, T. Nakanishi, and C. Dekker. Logic circuits with carbon nanotube transistors. *Science*, 294(5545):1317–1320, 2001.

[40] Y. R. Lu, S. Bangsaruntip, X. R. Wang, L. Zhang, Y. Nishi, and H. J. Dai. DNA functionalization of carbon nanotubes for ultrathin atomic layer deposition of high kappa dielectrics for nanotube transistors with 60 mV/decade switching. *Journal of the American Chemical Society*, 128(11):3518–3519, 2006.

[41] A. Javey, H. Kim, M. Brink, Q. Wang, A. Ural, J. Guo, P. McIntyre, P. McEuen, M. Lundstrom, and H. J. Dai. High-kappa dielectrics for advanced carbon-nanotube transistors and logic gates. *Nature Materials*, 1(4):241–246, 2002.

[42] W. Kim, A. Javey, O. Vermesh, O. Wang, Y. M. Li, and H. J. Dai. Hysteresis caused by water molecules in carbon nanotube field-effect transistors. *Nano Letters*, 3(2):193–198, 2003.

[43] S. H. Hur, M. H. Yoon, A. Gaur, M. Shim, A. Facchetti, T. J. Marks, and J. A. Rogers. Organic nanodielectrics for low voltage carbon nanotube thin film transistors and complementary logic gates. *Journal of the American Chemical Society*, 127(40):13808–13809, 2005.

[44] S. H. Lo, D. A. Buchanan, Y. Taur, and W. Wang. Quantum-mechanical modeling of electron tunneling current from the inversion layer of ultra-thin-oxide nMOSFET's. *IEEE Electron Device Letters*, 18(5):209–211, 1997.

[45] M. Halik, H. Klauk, U. Zschieschang, G. Schmid, C. Dehm, M. Schutz, S. Maisch, F. Effenberger, M. Brunnbauer, and F. Stellacci. Low-voltage organic transistors with an amorphous molecular gate dielectric. *Nature*, 431(7011):963–966, 2004.

[46] R. T. Weitz, U. Zschieschang, F. Effenberger, H. Klauk, M. Burghard, and K. Kern. High-performance carbon nanotube field effect transistors with a thin gate dielectric based on a self-assembled monolayer. *Nano Letters*, 7(1):22–27, 2007.

[47] R. T. Weitz, U. Zschieschang, H. Klauk, M. Burghard, and K. Kern. Single-walled carbon nanotube transistors on an ultra-thin gate dielectric. *Physica Status Solidi B-Basic Solid State Physics*, 243(13):3394–3398, 2006.

[48] M. Mardou. *Fundamentals of Microfabrication.* CRC Press, New York, first edition, 1997.

[49] C. Boulas, J. V. Davidovits, F. Rondelez, and D. Vuillaume. Suppression of charge carrier tunneling through organic self-assembled monolayers. *Physical Review Letters*, 76(25):4797–4800, 1996.

[50] M. Rittner, M. S. Martin-Gonzalez, A. Flores, H. Schweizer, F. Effenberger, and M. H. Pilkuhn. Nanostructural and electrical properties of functionally terminated self-assembled monolayers on silicon surfaces. *Journal of Applied Physics*, 98(5):054312, 2005.

[51] B De Boer, M. M. Frank, Y. J. Chabel, W. R. Jiang, E. Garfunkel, and Z. Bao. Metallic Contact Formation for Molecular Electronics: Interactions between Vapor-Deposited Metals (Au, Al and Ti) and Self-Assembled Monolayers of Conjugated Mono-and Dithiols. *Langmuir*, 20(5):1539–1542, 2004.

[52] M. Zharnikov and M. Grunze. Modification of thiol-derived self-assembling monolayers by electron and x-ray irradiation: Scientific and lithographic aspects. *Journal of Vacuum Science & Technology B*, 20(5):1793–1807, 2002.

[53] Z. Y. Tan, Y. Y. Xia, X. D. Liu, and M. W. Zhao. Monte-carlo simulation of low-energy electron scattering in pmma - using stopping powers from dielectric formalism. *Microelectronic Engineering*, 77(3-4):285–291, 2005.

[54] J. Appenzeller, J. Knoch, V. Derycke, R. Martel, S. Wind, and P. Avouris. Field-modulated carrier transport in carbon nanotube transistors. *Physical Review Letters*, 89(12):126801, 2002.

[55] A. Javey, J. Guo, D. B. Farmer, Q. Q. Wang, E. Yenilmez, R. G. Gordon, M. Lundstrom, and H. Dai. Self-aligned ballistic molecular

transistors and electrically parallel nanotube arrays. *Nano Letters*, 4(7):1319–1322, 2004.

[56] A. Javey, J. Guo, Q. Wang, M. Lundstrom, and H. J. Dai. Ballistic carbon nanotube field-effect transistors. *Nature*, 424(6949):654–657, 2003.

[57] M. H. Yang, K. B. K. Teo, L. Gangloff, W. I. Milne, D. G. Hasko, Y. Robert, and P. Legagneux. Advantages of top-gate, high-k dielectric carbon nanotube field-effect transistors. *Applied Physics Letters*, 88(11):113507, 2006.

[58] M. Radosavljevic, S. Heinze, J. Tersoff, and P. Avouris. Drain voltage scaling in carbon nanotube transistors. *Applied Physics Letters*, 83(12):2435–2437, 2003.

[59] A. Javey, R. Tu, D. B. Farmer, J. Guo, R. G. Gordon, and H. J. Dai. High performance n-type carbon nanotube field-effect transistors with chemically doped contacts. *Nano Letters*, 5(2):345–348, 2005.

[60] C. G. Lu, Q. Fu, S. M. Huang, and J. Liu. Polymer electrolyte-gated nanotube field-effect carbon transistor. *Nano Letters*, 4(4):623–627, 2004.

[61] G. P. Siddons, D. Merchin, J. H. Back, J. K. Jeong, and M. Shim. Highly efficient gating and doping of carbon nanotubes with polymer electrolytes. *Nano Letters*, 4(5):927–931, 2004.

[62] Y. M. Lin, J. Appenzeller, J. Knoch, and P. Avouris. High-performance carbon nanotube field-effect transistor with tunable polarities. *IEEE Transactions On Nanotechnology*, 4(5):481–489, 2005.

[63] J. Chen, C. Klinke, A. Afzali, and P. Avouris. Self-aligned carbon nanotube transistors with charge transfer doping. *Applied Physics Letters*, 86(12):123108, 2005.

[64] S. J. Wind, J. Appenzeller, and P. Avouris. Lateral scaling in carbon-nanotube field-effect transistors. *Physical Review Letters*, 91(5):058301, 2003.

[65] S. J. Wind, J. Appenzeller, R. Martel, V. Derycke, and P. Avouris. Vertical scaling of carbon nanotube field-effect transistors using top gate electrodes. *Applied Physics Letters*, 80(20):3817–3819, 2002.

[66] F. Nihey, H. Hongo, M. Yudasaka, and S. Iijima. A top-gate carbon-nanotube field-effect transistor with a titanium-dioxide insulator. *Japanese Journal of Applied Physics Part 2-Letters*, 41(10A):L1049–L1051, 2002.

[67] A. Javey, J. Guo, D. B. Farmer, Q. Wang, D. W. Wang, R. G. Gordon, M. Lundstrom, and H. J. Dai. Carbon nanotube field-effect transistors with integrated ohmic contacts and high-k gate dielectrics. *Nano Letters*, 4(3):447–450, 2004.

[68] A. Javey, P. F. Qi, Q. Wang, and H. J. Dai. Ten- to 50-nm-long quasi-ballistic carbon nanotube devices obtained without complex lithography. *Proceedings of the National Academy of Sciences of the United States of America*, 101(37):13408–13410, 2004.

[69] T. Dürkop, S. A. Getty, E. Cobas, and M. S. Fuhrer. Extraordinary mobility in semiconducting carbon nanotubes. *Nano Letters*, 4:35–39, 2004.

[70] W. Kim, A. Javey, R. Tu, J. Cao, Q. Wang, and H. J. Dai. Electrical contacts to carbon nanotubes down to 1 nm in diameter. *Applied Physics Letters*, 87(17):173101, 2005.

[71] X. L. Liu, S. Han, and C. W. Zhou. Novel nanotube-on-insulator (NOI) approach toward single-walled carbon nanotube devices. *Nano Letters*, 6(1):34–39, 2006.

[72] M. S. Fuhrer, B. M. Kim, T. Durkop, and T. Brintlinger. High-mobility nanotube transistor memory. *Nano Letters*, 2(7):755–759, 2002.

[73] J. B. Cui, R. Sordan, M. Burghard, and K. Kern. Carbon nanotube memory devices of high charge storage stability. *Applied Physics Letters*, 81(17):3260–3262, 2002.

[74] M. Radosavljevic, M. Freitag, K. V. Thadani, and A. T. Johnson. Nonvolatile molecular memory elements based on ambipolar nanotube field effect transistors. *Nano Letters*, 2(7):761–764, 2002.

[75] M. Burghard, G. Duesberg, G. Philipp, J. Muster, and S. Roth. Controlled adsorption of carbon nanotubes on chemically modified electrode arrays. *Advanced Materials*, 10(8):584–588, 1998.

[76] Z. H. Chen, J. Appenzeller, Y. M. Lin, J. Sippel-Oakley, A. G. Rinzler, J. Y. Tang, S. J. Wind, P. M. Solomon, and P. Avouris. An integrated logic circuit assembled on a single carbon nanotube. *Science*, 311(5768):1735–1735, 2006.

[77] Y. F. Hu, K. Yao, S. Wang, Z. Y. Zhang, X. L. Liang, Q. Chen, L. M. Peng, Y. G. Yao, J. Zhang, W. W. Zhou, and Y. Li. Fabrication of high performance top-gate complementary inverter using a single carbon nanotube and via a simple process. *Applied Physics Letters*, 90(22):223116, 2007.

[78] D. J. Gundlach, L. L. Jia, and T. N. Jackson. Pentacene TFT with improved linear region characteristics using chemically modified source and drain electrodes. *IEEE Electron Device Letters*, 22(12):571–573, 2001.

[79] J. E. Northrup and M. L. Chabinyc. Gap states in organic semiconductors: Hydrogen- and oxygen-induced states in pentacene. *Physical Review B*, 68(4):41202–1–4, 2003.

[80] A. Vollmer, O. D. Jurchescu, I. Arfaoui, I. Salzmann, T. T. M. Palstra, P. Rudolf, J. Niemax, J. Pflaum, J. P. Rabe, and N. Koch. The effect of oxygen exposure on pentacene electronic structure. *European Physical Journal E*, 17(3):339–343, 2005.

[81] F. De Angelis, S. Cipolloni, L. Mariucci, and G. Fortunato. Aging effects in pentacene thin-film transistors: Analysis of the density of states modification. *Applied Physics Letters*, 88(19):193508, 2006.

[82] O. D. Jurchescu, J. Baas, and T. T. M. Palstra. Effect of impurities on the mobility of single crystal pentacene. *Applied Physics Letters*, 84(16):3061–3063, 2004.

[83] J. H. Lee, G. H. Kim, S. H. Kim, S. C. Lim, Y. S. Yang, J. H. Youk, J. Jang, and T. Y. Zyung. Longevity enhancement of organic thin-film transistors by using a facile laminating passivation method. *Synthetic Metals*, 143(1):21–23, 2004.

[84] W. J. Kim, W. H. Koo, S. J. Jo, C. S. Kim, H. K. Baik, J. Lee, and S. Im. Passivation effects on the stability of pentacene thin-film transistors with sno2 prepared by ion-beam-assisted deposition. *Journal of Vacuum Science & Technology B*, 23(6):2357–2362, 2005.

[85] H. Klauk, U. Zschieschang, R. T. Weitz, H. Meng, T. Sun, G. Nunes, D. E. Keys, C. R. Fincher, and Z. Xiang. Organic transistors based on di(phenylvinyl)anthracene: Performance and stability. *Advanced Materials*, 19(22):3882–3887, 2007.

[86] K. Balasubramanian and M. Burghard. Chemically functionalized carbon nanotubes. *Small*, 1(2):180–192, 2005.

[87] Z. Yao, C. L. Kane, and C. Dekker. High-field electrical transport in single-wall carbon nanotubes. *Physical Review Letters*, 84(13):2941–2944, 2000.

[88] K.S. Kim, D.J. Bae, J.R. Kim, K.A. Park, S.C. Lim, J.J. Kim, W.B. Choi, C.Y. Park, and Y.H Lee. Modification of electronic structures of a carbon nanotube by hydrogen functionalization. *Advanced Materials*, 14:1818–1821, 2002.

[89] J.B. Cui, M. Burghard, and K. Kern. Room temperature single electron transistor by local chemical modification of carbon nanotubes. *Nano Letters*, 2(2):117–120, 2002.

[90] K. Balasubramanian, R. Sordan, M. Burghard, and K. Kern. A selective electrochemical approach to carbon nanotube field-effect transistors. *Nano Letters*, 4(5):827–830, 2004.

[91] J. Kong, N. R. Franklin, C. Zhou, M. G. Chapline, S. Peng, K. Cho, and H. Dai. Nanotube molecular wires as chemical sensors. *Science*, 287(5453):622–625, 2000.

[92] M. Bockrath, J. Hone, A. Zettl, Paul L. McEuen, Andrew G. Rinzler, and Richard E. Smalley. Chemical doping of individual semiconducting carbon-nanotube ropes. *Phys. Rev. B*, 61(16):R10606 – R10608, 2000.

[93] V. Derycke, R. Martel, J. Appenzeller, and P. Avouris. Controlling doping and carrier injection in carbon nanotube transistors. *Applied Physics Letters*, 80(15):2773–2775, 2002.

[94] C. Klinke, J. Chen, A. Afzali, and P. Avouris. Charge transfer induced polarity switching in carbon nanotube transistors. *Nano Letters*, 5(3):555–558, 2005.

[95] J. Kong, J. Cao, H. Dai, and E. Anderson. Chemical profiling of single nanotubes: Intramolecular p–n–p junctions and on-tube single-electron transistors. *Applied Physics Letters*, 80(1):73–75, 2002.

[96] J. Kong and H. Dai. Full and modulated chemical gating of individual carbon nanotubes by organic amine compounds. *Journal of Physical Chemistry B*, 105(15):2890–2893, 2001.

[97] C. Zhou, J. Kong, E. Yenilmez, and H. Dai. Modulated Chemical Doping of Individual Carbon Nanotubes. *Science*, 290(5496):1552–1555, 2000.

[98] F. Reininghaus, T. Korb, and H. Schoeller. Fingerprints of the magnetic polaron in nonequilibrium electron transport through a quantum wire coupled to a ferromagnetic spin chain. *Phys. Rev. Lett.*, 97(2):026803, 2006.

[99] F. Herren, P. Fischer, A. Ludi, and W. Halg. Neutron-diffraction study of prussian blue, $Fe_4[Fe(CN)_6]_3 \times H_2O$ - location of water-molecules and long-range magnetic order. *Inorganic Chemistry*, 19(4):956–959, 1980.

[100] S.F. Han, Y.M. Chen, R. Pang, P.Y. Wan, and M.H. Fan. Fabrication of prussian blue/multiwalled carbon nanotubes/glass carbon electrode through sequential deposition. *INDUSTRIAL & ENGINEERING CHEMISTRY RESEARCH*, 46(21):6847–6851, 2007.

[101] J. Li, H.D. Qiu, J.J. Xu, H.Y. Chen, and X.H. Xia. The synergistic effect of prussian-blue-grafted carbon nanotube/poly(4-vinylpyridine) composites for amperometric sensing. *Advanced Functional Materials*, 17(9):1574–1580, 2007.

[102] Z.F. Li, J.H. Chen, W. Li, K. Chen, L.H. Nie, and S.Z. Yao. Improved electrochemical properties of prussian blue by multi-walled carbon nanotubes. *Journal Of Electroanalytical Chemistry*, 603(1):59–66, 2007.

[103] L. Qian and X.R. Yang. Assembly of prussian blue onto SiO_2 nanoparticles and carbon nanotubes by electrostatic interaction. *Colloids and Surfaces A-Physiochemical and Engineering Aspects*, 278(1-3):123–128, 2006.

[104] X.R. Zhai, W.Z. Wei, J.X. Zeng, X.Y. Liu, and S.G. Gong. New nanocomposite based on prussian blue nanoparticles/carbon nanotubes/chitosan and its application for assembling of amperometric glucose biosensor. *Analytical Letters*, 39(5):913–926, 2006.

[105] Y.J. Zhang, Y. Wen, Y. Liu, D. Li, and J.H. Li. Functionalization of single-walled carbon nanotubes with prussian blue. *Electrochemistry Communications*, 6:1180–1884, 2004.

[106] L.D. Zhu, J.L. Zhai, Y.N. Guo, C.Y. Tian, and R.L. Yang. Amperometric glucose biosensors based on integration of glucose oxidase onto prussian blue/carbon nanotubes nanocomposite electrodes. *Electroanalysis*, 18:1842–1746, 2006.

[107] Y.J. Zou, L.X. Sun, and F. Xu. Prussian Blue electrodeposited on MWNTs-PANI hybrid composites for H_2O_2 detection. *Talanta*, 72:437–442, 2007.

[108] V.D. Neff. Electrochemical oxidation and reduction of thin-films of prussian blue. *Journal of the Electrochemical Society*, 125(6):886–887, 1978.

[109] K. Itaya, H. Akahoshi, and S. Toshima. Electrochemistry of prussian blue modified electrodes - an electrochemical preparation method. *Journal of the Electrochemical Society*, 129(7):1498–1500, 1982.

[110] K. Itaya, T. Ataka, and S. Toshima. Spectroelectrochemistry and electrochemical preparation method of prussian blue modified electrodes. *Journal of the American Chemical Society*, 104(18):4767–4772, 1982.

[111] A. A. Karyakin. Prussian blue and its analogues: Electrochemistry and analytical applications. *Electroanalysis*, 13(10):813–819, 2001.

[112] S.E. Kooi, U. Schlecht, M. Burghard, and K. Kern. Electrochemical modification of single carbon nanotubes. *Angewandte Chemie - International Edition*, 41(8):1353–1355, 2002.

[113] M. Pyrasch, A. Toutianoush, W. Jin, J. Schnepf, and B. Tieke. Self-assembled films of prussian blue and analogues: Optical and electrochemical properties and application as ion-sieving membranes. *Chemistry of Materials*, 15(1):245–254, 2003.

[114] J. Marwan, T. Addou, and D. Belanger. Functionalization of glassy carbon electrodes with metal-based species. *Chemistry of Materials*, 17(9):2395–2403, 2005.

[115] P. Somani, A. B. Mandale, and S. Radhakrishnan. Study and development of conducting polymer-based electrochromic display devices. *Acta Materialia*, 48(11):2859–2871, 2000.

[116] M. Datta and A. Datta. In-situ ftir and xps studies of the hexacyanoferrate redox system. *Journal of Physical Chemistry*, 94(21):8203–8207, 1990.

[117] E. Fluck, H. Inoue, and S. Yanagisawa. Mössbauer and x-ray photoelectron spectroscopic studies of prussian blue and its related compounds. *Zeitschrift für Anorganische und Allgemeine Chemie*, 430(3):241–249, 1977.

[118] J.F. Moulder, W. F. Stickle, P.E. Sobol, and K.D. Bomben. *Handbook of X-ray Photoelectron Spectroscopy.* Physical Electronics Inc., Minnesota, first edition, 1995.

[119] A.P. Grosvenor, B.A. Kobe, M.C. Biesinger, and N.S. McIntyre. Investigation of multiplet splitting of fe 2p xps spectra and bonding in iron compounds. *Surface and Interface Analysis*, 36(12):1564–1574, 2004.

[120] B. R. Goldsmith, J. G. Coroneus, V. R. Khalap, A. A. Kane, G. A. Weiss, and P. G. Collins. Conductance-Controlled Point Functionalization of Single-Walled Carbon Nanotubes. *Science*, 315(5808):77–81, 2007.

[121] S. J. Tans, A. R. M. Verschueren, and C. Dekker. Room-temperature transistor based on a single carbon nanotube. *Nature*, 393(6680):49–52, 1998.

[122] R. Graupner, J. Abraham, A. Vencelova, T. Seyller, F. Hennrich, M.M. Kappes, A. Hirsch, and L. Ley. Doping of single-walled carbon nanotube bundles by bronsted acids. *Physical Chemistry Chemical Physics*, 5(24):5472–5476, 2003.

[123] K. Kinoshita. *Carbon - Electrochemical and Physiochemical Properties.* Weiley Interscience, New York, first edition, 1988.

[124] W. Liang, M. Bockrath, D. Bozovic, J. H. Hafner, M. Tinkham, and H. Park. Fabry - perot interference in a nanotube electron waveguide. *Nature*, 441:665 – 669, 2001.

[125] J. Kong, E. Yenilmez, T. W. Tombler, W. Kim, H. Dai, R. B. Laughlin, L. Liu, C. S. Jayanthi, and S. Y. Wu. Quantum interference and ballistic transmission in nanotube electron waveguides. *Phys. Rev. Lett.*, 87(10):106801, 2001.

[126] L. L. Chua, J. Zaumseil, J. F. Chang, E. C. W. Ou, P. K. H. Ho, H. Sirringhaus, and R. H. Friend. General observation of n-type field-effect behaviour in organic semiconductors. *Nature*, 434(7030):194–199, 2005.

[127] A. Facchetti. Semiconductors for organic transistors. *Materials Today*, 10(3):28–37, 2007.

[128] R. C. Haddon, A. S. Perel, R. C. Morris, T. T. M. Palstra, A. F. Hebard, and R. M. Fleming. C60 thin-film transistors. *Applied Physics Letters*, 67(1):121–123, 1995.

[129] S. Kobayashi, T. Takenobu, S. Mori, A. Fujiwara, and Y. Iwasa. Fabrication and characterization of C60 thin-film transistors with high field-effect mobility. *Applied Physics Letters*, 82(25):4581–4583, 2003.

[130] G. Horowitz, F. Kouki, P. Spearman, D. Fichou, C. Nogues, X. Pan, and F. Garnier. Evidence for n-type conduction in a perylene tetracarboxylic diimide derivative. *Advanced Materials*, 8(3):242–245, 1996.

[131] J. G. Laquindanum, H. E. Katz, A. Dodabalapur, and A. J. Lovinger. n-channel organic transistor materials based on naphthalene frameworks. *Journal of the American Chemical Society*, 118(45):11331–11332, 1996.

[132] T. Suga, M. Iizuka, S. Kuniyoshi, K. Kudo, and K. Tanaka. Determination of effects of purity and atmospheric gases on electrical properties of perylene thin films by field effect measurement. *Synthetic Metals*, 102(1-3):1050–1051, 1999.

[133] P. R. L. Malenfant, C. D. Dimitrakopoulos, J. D. Gelorme, L. L. Kosbar, T. O. Graham, A. Curioni, and W. Andreoni. N-type organic thin-film transistor with high field-effect mobility based on a n,n-'-dialkyl-3,4,9,10-perylene tetracarboxylic diimide derivative. *Applied Physics Letters*, 80(14):2517–2519, 2002.

[134] D. J. Gundlach, K. P. Pernstich, G. Wilckens, M. Gruter, S. Haas, and B. Batlogg. High mobility n-channel organic thin-film transistors and complementary inverters. *Journal of Applied Physics*, 98(6):064502.

[135] S. Tatemichi, M. Ichikawa, T. Koyama, and Y. Taniguchi. High mobility n-type thin-film transistors based on n,n '-ditridecyl perylene diimide with thermal treatments. *Applied Physics Letters*, 89(11):112108, 2006.

[136] M. Ahles, R. Schmechel, and H. von Seggern. n-type organic field-effect transistor based on interface-doped pentacene. *Applied Physics Letters*, 85(19):4499–4501, 2004.

[137] Z. A. Bao, A. J. Lovinger, and J. Brown. New air-stable n-channel organic thin film transistors. *Journal of the American Chemical Society*, 120(1):207–208, 1998.

[138] M. M. Ling, Z. N. Bao, and P. Erk. Air-stable n-channel copper hexachlorophthalocyanine for field-effect transistors. *Applied Physics Letters*, 89(16):163516, 2006.

[139] H. E. Katz, J. Johnson, A. J. Lovinger, and W. J. Li. Naphthalenetetracarboxylic diimide-based n-channel transistor semiconductors: Structural variation and thiol-enhanced gold contacts. *Journal of the American Chemical Society*, 122(32):7787–7792, 2000.

[140] H. E. Katz, A. J. Lovinger, J. Johnson, C. Kloc, T. Siegrist, W. Li, Y. Y. Lin, and A. Dodabalapur. A soluble and air-stable organic semiconductor with high electron mobility. *Nature*, 404(6777):478–481, 2000.

[141] C. C. Kao, P. Lin, C. C. Lee, Y. K. Wang, J. C. Ho, and Y. Y. Shen. High-performance bottom-contact devices based on an air-stable n-type organic semiconductor n,n-bis (4-trifluoromethoxybenzyl)-1,4,5,8-naphthalene-tetracarboxylic di-imide. *Applied Physics Letters*, 90(21), 2007.

[142] H. Z. Chen, M. M. Ling, X. Mo, M. M. Shi, M. Wang, and Z. Bao. Air stable n-channel organic semiconductors for thin film transistors based on fluorinated derivatives of perylene diimides. *Chemistry of Materials*, 19(4):816–824, 2007.

[143] Y. Hosoi, D. Tsunami, I. Hisao, and Y. Furukawa. Air-stable n-channel organic field-effect transistors based on n,n '-bis(4-trifluoromethylbenzyl)perylene-3,4,9, 10-tetracarboxylic diimide. *Chemical Physics Letters*, 436(1-3):139–143, 2007.

[144] A. Facchetti, Y. Deng, A. C. Wang, Y. Koide, H. Sirringhaus, T. J. Marks, and R. H. Friend. Tuning the semiconducting properties of sexithiophene by alpha,omega-substitution - alpha,omega-diperfluorohexylsexithiophene: The first n-type sexithiophene for thin-film transistors. *Angewandte Chemie-International Edition*, 39(24):4547–4551, 2000.

[145] A. Facchetti, M. Mushrush, H. E. Katz, and T. J. Marks. n-type building blocks for organic electronics: A homologous family of fluorocarbon-substituted thiophene oligomers with high carrier mobility. *Advanced Materials*, 15(1):33–38, 2003.

[146] A. Facchetti, M. H. Yoon, C. L. Stern, H. E. Katz, and T. J. Marks. Building blocks for n-type organic electronics: Regiochemically modulated inversion of majority carrier sign in perfluoroarene-modified polythiophene semiconductors. *Angewandte Chemie-International Edition*, 42(33):3900–3903, 2003.

[147] A. Facchetti, J. Letizia, M. H. Yoon, M. Mushrush, H. E. Katz, and T. J. Marks. Synthesis and characterization of diperfluorooctyl-substituted phenylene-thiophene oligomers as n-type semiconductors. molecular structure-film microstructure-mobility relationships, organic field-effect transistors, and transistor nonvolatile memory elements. *Chemistry of Materials*, 16(23):4715–4727, 2004.

[148] A. Facchetti, M. Mushrush, M. H. Yoon, G. R. Hutchison, M. A. Ratner, and T. J. Marks. Building blocks for n-type molecular and polymeric electronics. perfluoroalkyl-versus alkyl-functionalized oligothiophenes (nt; n=2-6). systematics of thin film microstructure, semiconductor performance, and modeling of majority charge injection in field-effect transistors. *Journal of the American Chemical Society*, 126(42):13859–13874, 2004.

[149] H. M. Yoon, A. Facchetti, C. E. Stern, and T. J. Marks. Fluorocarbon-modified organic semiconductors: Molecular architecture, electronic, and crystal structure tuning of arene- versus fluoroarene-thiophene oligomer thin-film properties. *Journal of the American Chemical Society*, 128(17):5792 –5801, 2006.

[150] M. H. Yoon, C. Kim, A. Facchetti, and T. J. Marks. Gate dielectric chemical structure-organic field-effect transistor performance correlations for electron, hole, and ambipolar organic semiconductors. *Journal of the American Chemical Society*, 128(39):12851–12869, 2006.

[151] Y. Sakamoto, T. Suzuki, M. Kobayashi, Y. Gao, Y. Fukai, Y. Inoue, F. Sato, and S. Tokito. Perfluoropentacene: High-performance p-n junctions and complementary circuits with pentacene. *Journal of the American Chemical Society*, 126(26):8138–8140, 2004.

[152] Y. Inoue, Y. Sakamoto, T. Suzuki, M. Kobayashi, Y. Gao, and S. Tokito. Organic thin-film transistors with high electron mobility based on perfluoropentacene. *Japanese Journal of Applied Physics Part 1-Regular Papers Short Notes & Review Papers*, 44(6A):3663–3668, 2005.

[153] B. A. Jones, M. J. Ahrens, M. H. Yoon, A. Facchetti, T. J. Marks, and M. R. Wasielewski. High-mobility air-stable n-type semiconductors with processing versatility: Dicyanoperylene-3,4 : 9,10-bis(dicarboximides). *Angewandte Chemie-International Edition*, 43(46):6363–6366, 2004.

[154] M. M. Ling, P. Erk, M. Gomez, M. Koenemann, J. Locklin, and Z. N. Bao. Air-stable n-channel organic semiconductors based on perylene diimide derivatives without strong electron withdrawing groups. *Advanced Materials*, 19(8):1123–1127, 2007.

[155] M. M. Ling, Z. N. Bao, P. Erk, M. Koenemann, and M. Gomez. Complementary inverter using high mobility air-stable perylene di-imide derivatives. *Applied Physics Letters*, 90(9):093508, 2007.

[156] M. M. Shi, H. Z. Chen, J. Z. Sun, J. Ye, and M. Wang. Fluoroperylene diimide: a soluble and air-stable electron acceptor. *Chemical Communications*, (14):1710–1711, 2003.

[157] R. T. Weitz, K. Amsharov, U. Zschieschang, E. Barrena Villas, D.K. Goswami, M. Burghard, H. Dosch, M. Jansen, K. Kern, and H. Klauk. Film morphology, performance, and stability of n channel organic transistors based on core-cyanated perylene carboxylic diimide derivatives. *Journal of the American Chemical Society*, 130:34637, 2008.

[158] T. L. Threlfall. Analysis of organic polymorphs - a review. *Analyst*, 120(10):2435–2460, 1995.

[159] J. Tanaka. The electronic spectra of aromatic molecular crystals .2. the crystal structure and spectra of perylene. *Bulletin of the Chemical Society of Japan*, 36(10):1237–1249, 1963.

[160] J. Mizuguchi, K. Hino, and K. Tojo. Strikingly different electronic spectra of structurally similar perylene imide compounds. *Dyes and Pigments*, 70(2):126–135, 2006.

[161] M. Mobus, N. Karl, and T. Kobayashi. Structure of perylene-tetracarboxylic-dianhydride thin-films on alkali-halide crystal substrates. *Journal of Crystal Growth*, 116(3-4):495–504, 1992.

[162] D. M. deLeeuw, M. M. J. Simenon, A. R. Brown, and R. E. F. Einerhand. Stability of n-type doped conducting polymers and consequences for polymeric microelectronic devices. *Synthetic Metals*, 87(1):53–59, 1997.

[163] P. Atkins and J. de Paula. *Atkins' Physical Chemistry.* Oxford University Pres Inc., New York, seventh edition, 2002.

[164] S.F. Nelson, Y. Y. Lin, D.J. Gundlach, and T. N. Jackson. Temperature-independent transport in high-mobility pentacene transistors. *Appl. Phys. Lett*, 72(15):1854–1856, 1998.

[165] A. L. Briseno, S. C. B. Mannsfeld, M. M. Ling, S. H. Liu, R. J. Tseng, C. Reese, M. E. Roberts, Y. Yang, F. Wudl, and Z. N. Bao. Patterning organic single-crystal transistor arrays. *Nature*, 444(7121):913–917, 2006.

[166] C. Reese and Z. Bao. Organic single-crystal field-effect transistors. *Mat. Today*, 10(3):20–27, 2007.

[167] A. L. Briseno, S. C. B. Mannsfeld, X. M. Lu, Y. J. Xiong, S. A. Jenekhe, Z. N. Bao, and Y. N. Xia. Fabrication of field-effect transistors from hexathiapentacene single-crystal nanowires. *Nano Letters*, 7(3):668–675, 2007.

[168] Q. Tang, H. Li, M. He, W. Hu, C. Liu, K. Chen, C. Wang, Y. Liu, and D. Zhu. Low threshold voltage transistors based on individual single-crystalline submicrometer-sized ribbons of copper phthalocyanine. *Adv. Mater.*, 18:65–58, 2006.

[169] J. P. Hill, W. Jin, A. Koska, T. fukushima, H. Ichihara, T. Shimomura, K. Ito, T. Hashizume, N. Ishii, and T. Aida. Self-assembled hexa-peri-hexabenzocoronene graphitic nanotube. *Science*, 304:1481–1483, 2004.

[170] W. H. Lee, D. H. Kim, Y. Jang, J. H. Cho, M. Hwang, Y. D. Park, Y. H. Kim, J. I. Han, and K. Cho. Solution-processable pentacene microcrystal arrays for high performance organic field-effect transistors. *Appl. Phys. Lett.*, 90:132106, 2007.

[171] Y. Zhou, W. J. Liu, Y. Ma, L. Wang, H. Qi, Y. Cao, J. Wang, and J. Pei. Single microwire transistors of oligoarenes by direct solution process. *J. Am. Chem. Soc*, 129:12386–12387, 2006.

[172] D. H. Kim, D. Y. Lee, H. S. Lee, W. H. Lee, Y. H. Kim, J. I. Han, and K. Cho. High-mobility organic transistors based on single-crystalline microribbons of triisopropylisilylethynl pentacene via solution-phase self-assembly. *Advanced Materials*, 19(5):678–682, 2007.

[173] K. Balakrishnan, A. Datar, R. Oitker, H. Chen, J. M. Zuo, and L. Zang. Nanobelt self-assembly from an organic n-type semiconductor: Propoxyethyl-ptcdi. *Journal of the American Chemical Society*, 127(30):10496–10497, 2005.

[174] A. L. Briseno, S. C. B. Mannsfeld, C. Reese, J. M. Hancock, Y. Xiong, S. A. Jenekhe, Z. Bao, and Y. Xia. Perylenediimide nanowires and their use in fabricating field-effect transistors and complementary inverters. *Nano Letters*, 7(9):2847–2853, 2007.

[175] Y. K. Che, A. Datar, K. Balakrishnan, and L. Zang. Ultralong nanobelts self-assembled from an asymmetric perylene tetracarboxylic diimide. *Journal of the American Chemical Society*, 129(23):7234–7235, 2007.

[176] B.S. Ong, Y. Wu, P. Liu, and S. Gardner. High-performance semiconducting polythiophenes for organic thin-film transistors. *Journal of the American Chemical Society*, 126(11):3378–3379, 2004.

[177] G. Hadziioannou and G. G. Malliaras, editors. *Semiconducting Polymers - Chemistry, Physics and Engineering*. WILEY-VCH Verlag GmbH & Co. KGaA, Weinheim, second edition, 2007.

[178] Y. Dzenis. Spinning continuous fibers for nanotechnology. *Science*, 304(5679):1917–1919, 2004.

[179] D. H. Reneker and I. Chun. Nanometre diameter fibres of polymer, produced by electrospinning. *Nanotechnology*, 7(3):216–223, 1996.

[180] M. Bognitzki, W. Czado, T. Frese, A. Schaper, M. Hellwig, M. Steinhart, A. Greiner, and J. H. Wendorff. Nanostructured fibers via electrospinning. *Advanced Materials*, 13(1):70–72, 2001.

[181] A. Greiner and J. H. Wendorff. Electrospinning: A fascinating method for the preparation of ultrathin fibres. *Angewandte Chemie-International Edition*, 46(30):5670–5703, 2007.

[182] R. T. Weitz, L. Harnau, S. Rauschenbach, M. Burghard, and K. Kern. Polymer nanofibres via nozzle-free centrifugal spinning. *Nano Letters*, 8:1187, 2008.

[183] H. E. Huppert. Flow and instability of a viscous current down a slope. *Nature*, 300(5891):427–429, 1982.

[184] S. M. Troian, X. L. Wu, and S. A. Safran. Fingering instability in thin wetting films. *Physical Review Letters*, 62(13):1496–1499, 1989.

[185] F. Melo, J. F. Joanny, and S. Fauve. Fingering instability of spinning drops. *Physical Review Letters*, 63(18):1958–1961, 1989.

[186] L. E. Scriven and C. V. Sternling. Marangoni effects. *Nature*, 187(4733):186–188, 1960.

[187] A. M. Cazabat, F. Heslot, S. M. Troian, and P. Carles. Fingering instability of thin spreading films driven by temperature-gradients. *Nature*, 346(6287):824–826, 1990.

[188] J. Sur, T. P. Witelski, and R. P. Behringer. Steady-profile fingering flows in marangoni driven thin films. *Physical Review Letters*, 93(24):247803, 2004.

[189] P. G. de Gennes, F. Brochard-Wyart, and D. Quere. *Capillary and wetting phenoena.* Springer, New York, first edition, 2004.

[190] J. M. Burgess, A. Juel, W. D. McCormick, J. B. Swift, and H. L. Swinney. Suppression of dripping from a ceiling. *Physical Review Letters*, 86(7):1203–1206, 2001.

[191] R. Suryo and O. A. Basaran. Dripping of a liquid from a tube in the absence of gravity. *Physical Review Letters*, 96(3):034504, 2006.

[192] P. Gupta, C. Elkins, T. E. Long, and G. L. Wilkes. Electrospinning of linear homopolymers of poly(methyl methacrylate): exploring relationships between fiber formation, viscosity, molecular weight and concentration in a good solvent. *Polymer*, 46(13):4799–4810, 2005.

[193] H. Fong, I. Chun, and D. H. Reneker. Beaded nanofibers formed during electrospinning. *Polymer*, 40(16):4585–4592, 1999.

[194] C. Weber. The break-up of liquid jets. *Zeitschrift Fur Angewandte Mathematik Und Mechanik*, 11:136–154, 1931.

[195] J. Liu and S. Kumar. Microscopic polymer cups by electrospinning. *Polymer*, 46(10):3211–3214, 2005.

[196] P. B. Deotare and J. Kameoka. Fabrication of silica nanocomposite-cups using electrospraying. *Nanotechnology*, 17(5):1380–1383, 2006.

[197] G. Eda and S. Shivkumar. Bead structure variations during electrospinning of polystyrene. *Journal of Materials Science*, 41(17):5704–5708, 2006.

[198] M. Kaempgen, G.S. Duesberg, and S. Roth. Transparent carbon nanotube coatings. *Applied Surface Science*, 252(2):425–429, 2005.

[199] P. G. Collins, M. S. Arnold, and P. Avouris. Engineering Carbon Nanotubes and Nanotube Circuits Using Electrical Breakdown. *Science*, 292(5517):706–709, 2001.

[200] G. Zhang, P. Qi, X. Wang, Y. Lu, X. Li, R. Tu, S. Bangsaruntip, D. Mann, L. Zhang, and H. Dai. Selective Etching of Metallic Carbon Nanotubes by Gas-Phase Reaction. *Science*, 314(5801):974–977, 2006.

[201] L Bogani and W. Wernsdorfer. Molecular spintronics using single-molecule magnets. *Nature Materials*, 7:179–186, 2008.

[202] F. Wurthner. Perylene bisimide dyes as versatile building blocks for functional supramolecular architectures. *Chemical Communications*, (14):1564–1579, 2004.

[203] Q. P. Pham, U. Sharma, and A. G. Mikos. Electrospinning of polymeric nanofibers for tissue engineering applications: A review. *Tissue Engineering*, 12(5):1197–1211, 2006.

[204] B. K. Das, N. Shibata, and Y. Takeuchi. Design and synthesis of n-nonpolar nucleobase dipeptides: application of the ugi reaction for the preparation of dipeptides having uoroarylalkyl groups appended to the nitrogen atom. *Journal of the Chemical Society-Perkin Transactions 1*, (2):197–206, 2002.

Publications

- R. T. Weitz, A. Walter, R. Engl, R. Sezi, and C. Dehm, "New Charge-Transfer Salts for Reversible Resistive Memory Switching" *Nano Letters* **6**, 2810 (2006)
- R. T. Weitz, U. Zschieschang, H. Klauk, M. Burghard and K. Kern, "Single-walled carbon nanotube transistors on an ultra-thin gate dielectric" *phys. stat. sol. (b)* **243**, 3394 (2006)
- R. T. Weitz, U. Zschieschang, F. Effenberger, H. Klauk, M. Burghard and K. Kern, "High-performance carbon nanotube field effect transistors with a self-assembled monolayer gate dielectric" *Nano Letters* **7**, 22 (2007)
- R. T. Weitz, H. Klauk, U. Zschieschang, M. Burghard and K. Kern, "Organic monolayer gate dielectric for high-performance carbon nanotube transistors", *SPIE Newsroom* doi: 10.1117/2.1200705.0720, (2007)
- R. T. Weitz, H. Klauk, U. Zschieschang, M. Burghard and K. Kern, "High-performance single-walled carbon nanotube transistors on self-assembled organic monolayer gate dielectric", *Yearly report of the Max-Planck-Institute for Solid State Research* 2006, Stuttgart
- R.T. Weitz, S. Rauschenbach, A Forment-Aliaga, M. Burghard and K. Kern, "Investigation of the composition of layers of the charge-transfer salt CuDDQ", *phys. stat. sol. (b)* **244**, 4346 (2007)
- M. Burghard, K. Balasubramanian, T. Assmus, A. Forment-Aliaga, E. Lee, R.T. Weitz, M. Scolari, F. Nan, A. Mews, and K, Kern "Electrochemically modified single-walled carbon nanotubes", *phys. stat. sol. (b)* **244**, 4021 (2007)
- H. Klauk, U. Zschieschang, R. T. Weitz, H. Meng, F. Sun, G. Nunes, D. E. Keys, C. R. Fincher, and Z. Xiang "Organic Transistors Based

on Di(phenylvinyl)anthracene: Performance and Stability”, *Advanced Materials* **19**, 3882 (2007)

- C. Gómez-Navarro, R.T. Weitz, A.M. Bittner, M. Scolari, A. Mews, M. Burghard, and K. Kern, Electronic transport properties of individual chemically reduced graphene oxide sheets, *Nano Letters* **7**, 3499 (2007)
- K. Balasubramanian, E.J.H. Lee, R.T. Weitz, M. Burghard, and K. Kern ”Carbon Nanotube Transistors - Chemical Functionalization and Device Characterization”, *phys. stat. sol. (a)*, **205**, 633 (2008)
- R. T. Weitz, K. Amsharov, U. Zschieschang, E. Barrena Villas, D. K. Goswami, M. Burghard, H. Dosch, M. Jansen, K. Kern, and H. Klauk ”Film Morphology, Performance, and Stability of n Channel Organic Transistors Based on Core-Cyanated Perylene Carboxylic Diimide Derivatives”, *J. Am. Chem. Soc.*, **130**, 4637 (2008)
- M. Häffner, A. Haug, R.T. Weitz, M. Fleischer, M. Burghard, H. Peisert, T. Chass, and D.P. Kern ”E-beam lithography of catalyst patterns for carbon nanotube growth on insulating substrates”, *Microelectronics Engineering*, **85**, 768 (2008)
- R.T. Weitz, L. Harnau, S. Rauschenbach, M. Burghard, and K. Kern, ”Polymer Nanofibres via Nozzle-Free Centrifugal Spinning”, *Nano Letters*, **8**, 1187 (2008)
- E.J.H. Lee, K. Balasubramanian, R.T. Weitz, M. Burghard and K. Kern, ”Contact and Edge Effects in Graphene Devices”, *submitted*
- A. Forment-Aliaga, R. Thomas Weitz, A.S. Sagar, M. Konuma, M. Burghard and K. Kern ”Electrical properties of individual carbon nanotubes functionalized by a molecular magnet”, *submitted*
- R. Vogelgesang, J. Dorfmller, R. Esteban, R.T. Weitz, A. Dmitriev, and K. Kern ”Plasmonic nanostructures in aperture-less scanning near field optical microscopy (aSNOM)”, *submitted*
- R.T. Weitz, U. Zschieschang, A. Forment-Aliaga, D. Kälblein, M. Burghard, K. Kern and H. Klauk ”Reliability of carbon nanotube transistors with patterned gates and molecular gate dielectric”, *in preparation*

Acknowledgement

It is my great pleasure to acknowledge all those that contributed to the success of this thesis.

I am thankful to Prof. Dr. Klaus Kern for giving me the opportunity to perform my PhD research at the Max Planck Institute for Solid State Research in Stuttgart and for guiding me through the course of this thesis.

My special gratitude goes to Prof. Dr. R. Schaller, Prof. Dr. J. Brugger, Dr. P. Gröning and Dr. H. Klauk for being part of the PhD jury.

PD Dr. Marko Burhard, my direct advisor, I would like to thank for fruitful discussions, continuous support and for giving me great freedom in the details of my work.

I am indebted to Dr. Hagen Klauk for in-depth discussions, advice, continuous support and the joint work in the lab.

My fellow PhD Students and post-Docs that contributed to this work, I also would like to thank very much. I especially enjoyed the close collaboration with Dr. A. Forment-Aliaga, Dr. U. Zschieschang, Dr. K. Balasubramanian, Dr. R. Sordan, Dr. Christina Gómez-Navarro, E. Lee, J. Böttcher, D. Kälblein and F. Ante. Also the whole Kern department I would like to thank for the friendly working atmosphere.

Dr. Stephan Rauschenbach I would like to thank for in-depth discussions of scientific and non-scientific topics.

I also would like to acknowledge the friendly atmosphere and discussions in our office with Dr. Thomas Classen, Dr. Georgios Katsaros, Dr. Stephan Rauschenbach, Jens Dorfmüller and Dr. Christina Gómez-Navarro.

S. Neubeck and A. Küster I would like to acknowledge for their support with setting a vacuum chamber.

I would like to thank Dr. K. Amsharov and Prof. Dr. M. Jansen for the synthesis of the perylene diimide compounds and helpful discussions.

S. Birtel I would like to thank for uncomplicated support with paperwork.

The members of the technical workshop W. Stiepany, P. Andler and A. Koch as well as M. Siemers and R. Chaikevitch I would like for their through support in all technical questions.

The "clean-room-team", U. Waizmann, T. Reindel and M. Riek I would like to thank for their very competent support.
Dr. E. Barrena Villas I am indebted for the X-ray analysis of the perylene diimide films.
PD Dr. L. Harnau I would like to thank for preparing the theory part on the work concerning the polymer nanofibres.
The members of the service groups of the Max-Planck-Institute deserve special thanks for their always helpful and very competent support.
My special thanks goes to my family and Sarah for support in all respects.